Measurement of the Charm Production in $\gamma\gamma$ Interactions at LEP

DISSERTATION
zur Erlangung des Grades
eines Doktors der Naturwissenschaften

vorgelegt von
Dipl.-Phys. An Bang Ngac
aus Hanoi, Vietnam

eingereicht beim Fachbereich 7
der Universität Siegen

Siegen 2003

Contents

Chapter 1

Introduction

Built to perform precision measurements of the carriers of the electroweak interactions, the Z and W bosons, the ALEPH detector at LEP gave also an ideal opportunity to study two-photon interactions $\mathrm{e^+e^-} \rightarrow \mathrm{e^+e^-}\gamma^\star\gamma^\star \rightarrow \mathrm{e^+e^-}X$. Especially at LEP 2 energies, $\sqrt{s_{\mathrm{e^+e^-}}} = 183\,\mathrm{GeV} - 209\,\mathrm{GeV}$, the two-photon interaction is by far the dominant process with relatively low background. Due to the rather complex partonic structure of the photon, the field turns out to be a rich and clean environment to undertake precision phenomenology and obtain quantitative tests of perturbative QCD. The main processes of interest are deep-inelastic scattering, large p_T phenomena, heavy flavour production and the formation of resonances.

Heavy flavour production in two-photon events at LEP 2 centre-of-mass energies is dominated by charm production processes in which both of the photons couple directly (*direct processes*) or in which one photon couples directly and the other appears resolved (*single-resolved processes*). Because the single-resolved process is dominated by γg fusion, the measurement of the cross section can give access to the gluon content of the photon. Moreover, the large masses of the c and b quarks provide a cutoff for perturbative QCD calculations, allowing a good test of QCD predictions for the corresponding reactions. Contributions from processes in which both photons appear resolved (*double-resolved processes*) are suppressed by more than two orders of magnitude compared to the total cross section. The production of b quarks is expected to be suppressed by a large factor compared to charm quark because of the heavier mass and smaller absolute charge.

This present analysis aims at the measurement of charm production in $\gamma\gamma$ collisions at LEP 2 energies using the $\mathrm{D^{*\pm}}$–tagging method. The tagging of charmed quarks is performed using exclusively reconstructed $\mathrm{D^{*\pm}}$ mesons in their dominant decay to $\mathrm{D^0}\pi^\pm$ with the $\mathrm{D^0}$ mesons being subsequently identified in three different decay modes, (1) $\mathrm{K^\mp}\pi^\pm$, (2) $\mathrm{K^\mp}\pi^\pm\pi^0$, and (3) $\mathrm{K^\mp}\pi^\pm\pi^\mp\pi^\pm$. The relative size of the main contributions, direct and single-resolved processes, is of special interest. Differential cross sections of $\mathrm{D^{*\pm}}$ production as functions of $p_\mathrm{t}^{\mathrm{D^{*\pm}}}$ and the pseudorapidity $|\eta^{\mathrm{D^{*\pm}}}|$ are measured within the experimentally accessible kinematic region. They are compared to next-to-leading order (NLO) perturbative QCD calculations.

1. Introduction

The total cross section of charm production $\sigma(\mathrm{e^+e^-} \to \mathrm{e^+e^-} c\bar{c})_{<\sqrt{s}>=197\,\mathrm{GeV}}$ is determined by extrapolating the visible inclusive $\mathrm{D}^{*\pm}$ cross section $\sigma_{\mathrm{visible}}^{\mathrm{D}^{*\pm}}$ from the accessible kinematic range to the total phase space available, taking into account the probability for a charm quark to fragment into a $\mathrm{D}^{*\pm}$ meson. The result is then compared to NLO perturbative QCD prediction.

This thesis is organized as follows. An overview of the basics of two-photon physics and heavy flavour production is given in Chapter 2. Chapter 3 gives a short description of the ALEPH detector. The whole analysis is presented in Chapter 4. Finally, in Chapter 5 a summary is given.

Throughout this thesis charge-conjugated particles and their decays are implicitly included.

Chapter 2

Two-Photon Interactions and Heavy Flavour Production

2.1 Two-Photon Interactions

2.1.1 The Photon

The photon is a fundamental, massless and structureless particle in the framework of the standard model [1–3]. As the gauge boson of the theory of Quantum Electrodynamics (QED), the photon mediates the electromagnetic interactions between charged objects and couples only to charged particles. However, due to the Heisenberg uncertainty principle, the photon can fluctuate briefly into any charged fermion-antifermion pair with the same quantum number as the photon (Fig. 2.1). While the photon is in one of these virtual states, it can be considered as a complex structure particle so called a resolved photon.

The fluctuations of the photon into a lepton-antilepton pair $(l^+l^-, l = \mathrm{e}, \mu, \tau)$ are purely QED processes. These leptonic fluctuations are therefore fully calculable. The fluctuations into pairs of quarks and antiquarks are much more complicated as they involve the strong interactions between the induced quarks. It is customary to separate the spectrum of these q$\bar{\mathrm{q}}$ fluctuations into a low-virtuality and a high-virtuality part using some cut-off parameter Q_0 [4]. Highly virtual photons fluctuate into q$\bar{\mathrm{q}}$ pairs with transverse momenta p_t greater than the cut-off scale Q_0. These fluctuations, labelled as anomalous, are perturbatively calculable in the framework of the Quark Parton Model (QPM) [5]. The QPM essentially ignores the strong interactions between the quarks and considers them as fractionally charged and massive QED particles.

Fluctuations of low-virtuality photons into q$\bar{\mathrm{q}}$ pairs with p_t below Q_0 are described by non-perturbative QCD models such as the Vector Meson Dominance (VMD) model [6,7]. This model takes into account the strong interactions between the produced quarks and treats the photon as a superposition of the lowest-lying vector mesons such as $\rho, \omega, \phi, J/\psi...$ which have the same quantum numbers as the
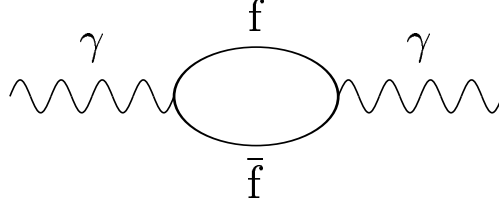
Figure 2.1: Photon fluctuation into a pair of fermion-antifermion.

Figure 2.2: The different appearances of the photon.

photon. In real interactions, the transition between VMD and anomalous should be smooth.

The photon wave function $|\gamma\rangle$ can be written as a superposition of all possible contributions (Fig. 2.2) as

$$|\gamma\rangle = \underbrace{c_{\text{dir}}|\gamma_{\text{dir}}\rangle}_{\text{direct}} + \underbrace{\sum_{V=\rho^0,\omega,\phi,J/\psi} c_V|V\rangle}_{\text{VMD}} + \underbrace{\sum_{q=u,d,s,c,b} c_q|q\bar{q}\rangle}_{\text{anomalous}} + \underbrace{\sum_{\ell=e,\mu,\tau} c_\ell|\ell^+\ell^-\rangle}_{\text{leptonic}} \qquad (2.1)$$

The coefficients c_i depend on the scale μ to probe the photon. It is usually taken to be the transverse momentum of a $2 \to 2$ parton-level process. Explicit forms of c_i can be found in [4]. The leptonic fluctuation $\gamma \to l^+l^- \to \gamma$ will not be considered hereafter.

The separation of the $q\bar{q}$ fluctuation into VMD and anomalous parts is the basis of all parton density function (PDF) parametrizations for the photon and therefore is the central part of Monte Carlo event generators for two-photon physics. Neglecting the leptonic component, the PDF of the photon can be written as

$$f_i^\gamma(x_\gamma, Q^2) = f_i^{\gamma,\text{direct}}(x_\gamma, Q^2) + f_i^{\gamma,\text{VMD}}(x_\gamma, Q^2, Q_0^2) + f_i^{\gamma,\text{anomalous}}(x_\gamma, Q^2; Q_0^2) \quad (2.2)$$

where

- Q^2 is the virtuality of the photon,
- Q_0 is the cut-off scale,

- x_γ is the so-called "Bjorken-scale variable", which can be interpreted as the fraction of the four-momentum of the photon which takes part in the hard interactions.

There are several sets of PDF's for real and virtual photons in leading and next-to-leading orders. These PDF parametrizations differ in the value of the cut-off scale Q_0, below which the perturbative part should vanish, as well as how to model the nonperturbative distribution (VMD part). Some of them used in this analysis will be discussed briefly below , a more detailed review on this topic can be found in [8].

GRV [9,10] **G**lück, **R**eya and **V**ogt constructed this set of PDF's using the known PDF of the pion from [11]. These PDF's are available in leading (LO) and next-to-leading order (NLO). The scale Q_0 was chosen to be $Q_0^2 = 0.25\text{GeV}^2$ and 0.3GeV^2 for the LO and NLO sets, respectively. At $Q = Q_0$, the perturbative part vanishes and the PDF of the pion is assumed to describe the VMD part. The Q^2 evolution is carried out using the DGLAP equations [12–16]. Since the parton density function of the pion cannot be calculated in an absolute normalization, a free parameter κ is introduced and has to be determined from experimental data.

GRS [17] This set of PDFs was introduced by **G**lück, **R**eya and **S**chienbein. It is basically the same as the GRV parametrization. Beside using the updated pion data from [18], this set of PDFs does not need any free parameter since it uses a coherent sum of low-mass vector mesons.

AFG [19] **A**urenche, **F**ontannaz and **G**uillet contructed the AFG parametrizations in a similar way as in the case of the GRS. At the scale $Q_0^2 = 0.5\text{GeV}^2$, a purely nonperturbative distribution based on the VMD arguments is assumed using a coherent sum of low-mass vector mesons. The Q^2 evolution is performed using the DGLAP equations in the massless scheme for three light flavours for $Q^2 < m_\text{c}^2 = 2\text{GeV}^2$ and for four flavours for $Q^2 > m_\text{c}^2 = 2\text{GeV}^2$.

SaS [20] Two sets of LO PDFs are given by **S**chuler **a**nd **S**jöstrand, SaS1 with $Q_0^2 = 0.36\text{GeV}^2$ and SaS2 with $Q_0^2 = 4\text{GeV}^2$. Contributions from charm and bottom quarks were taken into account. For the SaS1 set, both the scale Q_0^2 and the normalization of the VMD contribution are determined from the analysis of γp scattering data, while the shape of this VMD contribution is fitted to the data of the photon structure function. The subdivision into anomalous (point-like) and VMD (hadron-like) parton distribution functions is made explicitly in the SaS parametrizations, thus, allowing for an independent treatment of the two.

2.1.2 Two-Photon Interactions

Photon-photon interactions are complicated since each of the incoming photons is described by the wave function (2.1) with several different components. Each of

2. Two-Photon Interactions and Heavy Flavour Production

those has its own interactions. In total there are $3 \times 3 = 9$ combinations. However, trivial symmetry reduces this into six distinct classes shown in Fig. 2.3. They are [4]

a. VMD × VMD, where both photons convert into vector mesons prior to interactions (Fig. 2.3 a). All the processes known from ordinary hadron-hadron interactions may thus occur in this class.

b. VMD × direct, in which a direct (bare) photon interacts with a parton of the VMD photon (Fig. 2.3 b).

c. VMD × anomalous, wherein the anomalous photon perturbatively fluctuates into a q$\bar{\text{q}}$ pair, and one of these quarks interacts with a parton from the VMD photon (Fig. 2.3 c).

d. direct × direct, which corresponds to the subprocess $\gamma\gamma \to$ q$\bar{\text{q}}$ (Fig. 2.3 d). The leptonic final state l^+l^- is also possible, but will not be considered here.

e. direct × anomalous, in which a direct (bare) photon interacts with a parton of the anomalous photon (Fig. 2.3 e).

f. anomalous × anomalous, where both photons perturbatively branch into pairs of q$\bar{\text{q}}$, and subsequently one parton from each photon undergoes a hard interaction (Fig. 2.3 f).

This classification based on the parametrization (2.1) is not unique. More commonly used in two-photon physics is to put together the VMD and anomalous photons into a common class called resolved photon (Section 2.1.1 and Fig. 2.2). The classification of the two-photon events at the parton level is now simpler:

1. Direct process $\gamma\gamma \to$ q$\bar{\text{q}}$ in which both photons interact as a bare particle and directly produce a q$\bar{\text{q}}$ pair as in the class d above.

2. Single-resolved process where one of the photons couples directly to the parton of the other resolved photon. Possible subprocesses are γq $\to$ qg and γg $\to$ q$\bar{\text{q}}$ which occur in class b and e in the previous classification.

3. Double-resolved process wherein two resolved photons interact with each other. Several subprocesses are possible: qq$'$ $\to$ qq$'$, q$\bar{\text{q}}$ $\to$ q$'\bar{\text{q}}'$, q$\bar{\text{q}}$ $\to$ gg, qg $\to$ qg, gg $\to$ q$\bar{\text{q}}$, gg $\to$ gg. They could occur in the classes a, c and f above.

The discussed classifications are defined only in an operative manner, there should be no sharp border between those classes of events but rather smooth transitions between them. Moreover, these are in the LO scenario at the parton level. In reality, parton showers and hadronisations would smear out any parton level border. Higher-order considerations would make these processes no longer well defined and become scheme-dependent.
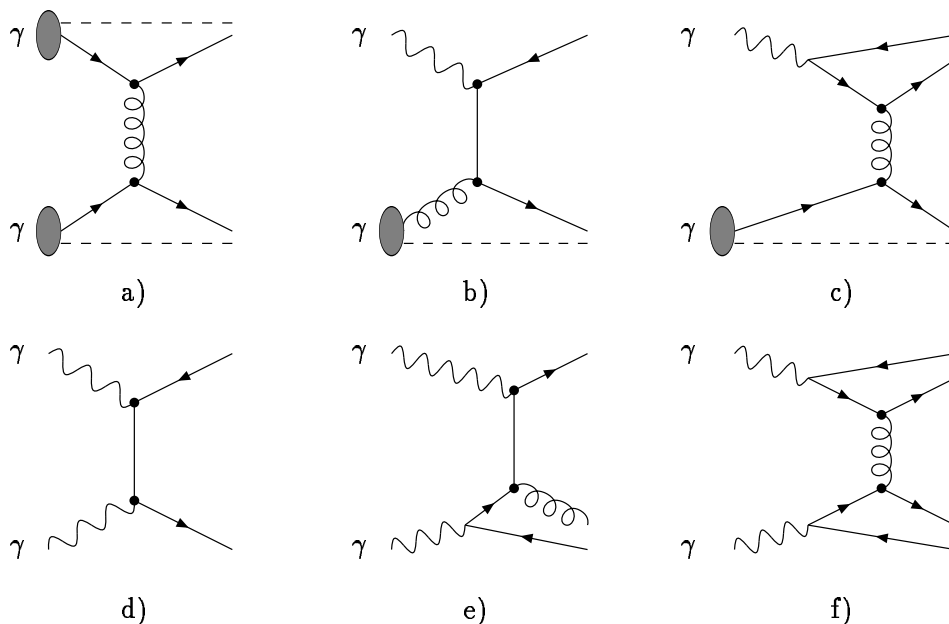
Figure 2.3: Contributions to hard $\gamma\gamma$ interaction: a) VMD $\times$ VMD, b) VMD $\times$ direct, c) VMD $\times$ anomalous, d) direct $\times$ direct, e) direct $\times$ anomalous, f) anomalous $\times$ anomalous. Only the basic graphs are shown; additional partonic activity is allowed. This figure is taken from [4].

2.1.3 Two-photon Physics at LEP

In order to study two-photon interactions $\gamma\gamma \rightarrow X$, sources which can produce high intense fluxes of very high energy photons are required. One of these sources is provided by the clouds of high energy virtual photons surrounding beam particles in high energy $\mathrm{e^+e^-}$ storage rings like LEP.

Kinematics

Two-photon interaction at LEP is of the form

$$\mathrm{e^+e^-} \rightarrow \mathrm{e^+e^-} \gamma^\star \gamma^\star \rightarrow \mathrm{e^+e^-} X, \tag{2.3}$$

where

- the virtual photons $\gamma^\star$ are emitted by the beam electrons via bremsstrahlung,
- $\gamma\gamma$ interaction produces the final state X, which could be either leptonic or hadronic.

The leptonic channels $\mathrm{e^+e^-} \rightarrow \mathrm{e^+e^-} \gamma^\star \gamma^\star \rightarrow \mathrm{e^+e^-} l^+ l^- (l = \mathrm{e}, \mu, \tau)$, are purely QED processes and can be calculated to an accuracy of the order of α_{em}^4. This

type of event will not be considered hereafter. The kinematics of the reaction (2.3) is shown in Fig. 2.4. Two incoming beam electrons with four-momenta $p_i = (E_i, \vec{p_i}), (i = 1, 2)$ radiate photons $\gamma_i^{\star}$ with four-momenta $q_i, (i = 1, 2)$. These beam electrons are then scattered at angles θ_i with respect to the beam directions carrying away four-momenta $p_i' = (E_i', \vec{p_i}')$. For unpolarized electron beams of given beam energy E_i, the $\gamma\gamma$ system can be described by five variables

- the energy of the scattered electrons E_i',
- the scattering angles θ_i,
- and the angle between the two electron scattering planes ϕ.

The invariant mass squared $W_{\gamma\gamma}$ of the $\gamma\gamma$ system is

$$
\begin{aligned}
W_{\gamma\gamma}^2 &= (q_1 + q_2)^2 \\
&= 4E_{\gamma 1}E_{\gamma 2} - 2E_1'E_2' \left(1 - \cos\theta_1 \cos\theta_2 - \sin\theta_1 \sin\theta_2 \cos\phi\right) \quad , \quad (2.4)
\end{aligned}
$$

neglecting the electron mass m_{e}. The kinematic properties of the radiated photons are defined by their negative squared four-momentum transfers Q_i^2, which measure the virtualities of these photons. These quantities can be calculated by

$$
Q_i^2 = -q_i^2 \approx 2E_iE_i' \left(1 - \cos\theta_i\right) > 0 \quad , \tag{2.5}
$$

again neglecting the electron mass m_{e}. The scattering angles θ_i are usually small. The scattered electrons therefore may or may not be detected depending on the acceptance of the detector in the very forward direction. If the scattered electron is detected, then its four-momentum p_i' is usually well measured and so is the virtuality Q_i^2 of the corresponding photon. In this case, this electron is called a tagged electron. Two-photon events can thus be classified according to the number of tagged electrons.

- No-tag events: Neither scattered electrons is detected. They both escape through the beam pipe leaving very little information about the photons. Nevertheless, since the θ_i are very small, the virtuality $Q_i^2 \approx 0$ and both photons can be regarded as quasi-real photons. This type of event has the highest rate. It is therefore useful for studying the final state X such as total cross section of $\gamma\gamma$ production, single inclusive particle as well as di-jet productions, exclusive resonances, and heavy quark (charm and bottom) production. At LEP, there is a remakable progress in studying this field [21]. The charm production in $\gamma\gamma$ collisions is the subject of this thesis.
- Single-tag events: Only one scattered electron is detected and the other is lost in the beam pipe. Thus, one of the photons is highly virtual and the other is quasi-real $Q_1^2 \gg Q_2^2 \approx 0$. This class of event can be considered as deep inelastic scattering (DIS) of an electron off a quasi-real photon via exchange of a virtual photon. In this kinematic regime, ALEPH has carried out number of
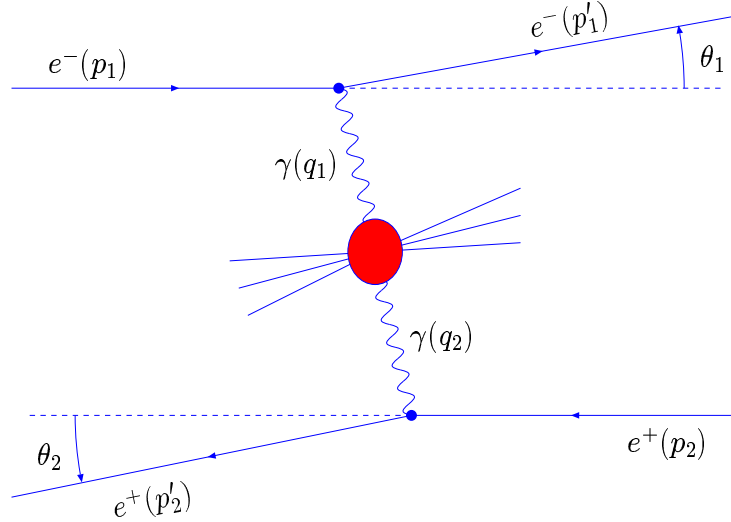
Figure 2.4: The kinematics of the two-photon interaction at LEP.

analyses on the structure functions $F_2^\gamma(x, Q^2)$ of the photon [22–26]. There is one problem, though, concerning $W_{\gamma\gamma}$ (2.4). This quantity is usually not well measured in single-tag events, and no-tag events for that matter. Therefore unfolding is neccesary.

- Double-tag events: Both scattered electrons are detected giving, in principle, the full kinematics of the event. Both Q_i^2 as well as $W_{\gamma\gamma}$ can be directly measured and thus unfolding is not needed. Using this type of event, the cross section for virtual $\gamma^\star \gamma^\star$ interactions can be measured and then used to test the QCD models [27,28]. Unfortunately, the rate of double-tag events is very low, making this measurement difficult.

Total Cross Section

The total cross section for the reaction (2.3) can be separated into two parts, one part dealing with the production of the photons at the eγ vertices and the other with the production of the final state X from two-photon interactions. Detailed calculations can be found in [29]. The cross section $\sigma(e^+e^- \to e^+e^-X)$ can be written in the form

$$
\begin{aligned}
\mathrm{d}^6\sigma \;=\;& \mathrm{d}^6\sigma(e^+e^- \to e^+e^-X) = \\
& \frac{\mathrm{d}^3 p_1' \mathrm{d}^3 p_2'}{E_1' E_2'} \frac{\alpha_{\mathrm{em}}^2}{16\pi^4 Q_1^2 Q_2^2} \left[\frac{(q_1 \cdot q_2)^2 - Q_1^2 Q_2^2}{(p_1 \cdot p_2)^2 - 2m_e^2} \right]^{1/2} \\
& \times (4\rho_1^{++}\rho_2^{++}\sigma_{\mathrm{TT}} + 2|\rho_1^{+-}\rho_2^{+-}|\tau_{\mathrm{TT}}\cos 2\bar\phi + 2\rho_1^{++}\rho_2^{00}\sigma_{\mathrm{TL}} \\
& + 2\rho_1^{00}\rho_2^{++}\sigma_{\mathrm{TL}} + \rho_1^{00}\rho_2^{00}\sigma_{\mathrm{LL}} - 8|\rho_1^{+0}\rho_2^{+0}|\tau_{\mathrm{TL}}\cos\bar\phi),
\end{aligned} \tag{2.6}
$$

where

- $\bar{\phi}$ is the angle between the scattering planes of the two electrons in the $\gamma\gamma$ centre-of-mass frame,
- the density matrices ρ_1^{ij} and ρ_2^{ij} with $i, j \in [+, -, 0]$ contain the helicity information of the photons 1 and 2,
- the σ's and τ's are cross section and interference terms respectively. The subscript T's and L's denote an interaction between transverse (T, helicity ± 1) or longitudinal (L, helicity 0) photons.

The cross section formula (2.6) simplifies substantially, if the reaction (2.3) involves quasi-real photons. Since a quasi-real photon has no longitudinal polarisation, all terms containing the longitudinal polarisation component of that photon like σ_{LL}, σ_{TL} and τ_{TL} disappear.

Figure 2.5 show the predicted total cross sections for various processes as functions of the e^+e^- centre-of-mass energy $\sqrt{s}$ at LEP. The two-photon production (2.3) is by far the dominant process at LEP 2 energies. Background processes like e^+e^- annihilation and W-pair production have much lower cross sections. The high luminosity (almost $700\mathrm{pb}^{-1}$) and high energy (up to $\sqrt{s} = 209\mathrm{GeV}$) available make it possible to undertake precision phenomenology and obtain quantitative tests of perturbative QCD. The main processes of interest in two-photon physics at LEP 2 are deep-inelastic scattering, large p_{T} phenomena and heavy flavour production.
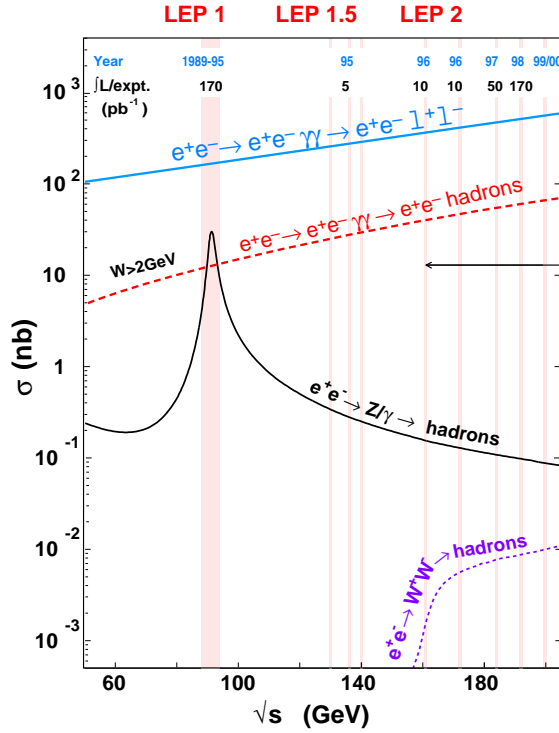
Figure 2.5: Cross sections for various processes as functions of the e^+e^- centre-of-mass energy $\sqrt{s}$ at LEP [30].

2.2 Heavy Flavour Production in $\gamma\gamma$ Collisions

Heavy flavour production has been studied both as tests of QCD and as probes for other physics aspects within and beyond the standard model. A quark Q is defined as heavy when its mass m_Q is much lager than $\Lambda_{QCD} \approx 200 - 300\,\mathrm{MeV/c^2}$. This parameter Λ_{QCD} represents the scale at which the coupling gets too large to apply perturbative QCD calculation. More qualitatively, it indicates the order of magnitude of the scale at which the strong coupling constant $\alpha_s(Q^2)$ becomes too large and the perturbative theory breaks down. Charm (c), bottom (b), and top (t) quarks are heavy. However, the top quark is too heavy to be produced at LEP. Moreover, it decays weakly before hadronizing. Throughout this discussion heavy quark will therefore have to be understood as a charm or a bottom quark.

The mass of a heavy quark m_Q acts as a cut-off for collinear singularities and sets a hard scale at which the α_s can be evaluated and found small enough for the perturbative QCD calculation. The cross section for heavy flavour production is perturbatively calculable with corrections being suppressed by powers of the heavy quark mass m_Q. Heavy flavour production in $\gamma\gamma$ collisions at LEP is of the form

$$e^+e^- \rightarrow e^+e^-\gamma^\star\gamma^\star \rightarrow e^+e^-Q\bar{Q} \quad . \tag{2.7}$$

The production of heavy quarkonia below the open heavy quark thresholds, $D\bar{D}$ and/or $B\bar{B}$, is also a very attractive and challenging domain of $\gamma\gamma$ physics. Resonances with $J^{PC} = 0^{-+}, 0^{++}, 2^{-+}, 2^{++}$ can be exclusively and cleanly produced. Although suffering from poor statistics, LEP experiments have carried out several analyses related to the formation and production of the $c\bar{c}$ ground state η_c [31,32]. The first search for the undetected bottomonium ground state η_b was performed in ALEPH [33].

The cross section for open heavy quark production is dominated by the scattering of two on-shell photons (no-tag events) which produces a pair of heavy quarks $Q\bar{Q}$. The field has been actively investigated by all four experiments at LEP. The total cross section as well as single inclusive distributions were calculated in perturbative QCD to NLO accuracy. There are two NLO QCD models available for comparisons with measurements, the fixed-order (FO) NLO QCD [34] and the resummed (RES) NLO QCD [35].

2.2.1 QCD Models for Heavy Quark Production

The transverse momentum $p_T(Q)$ of a heavy quark Q enters into the QCD calculations as another hard scale beside the quark mass m_Q. Depending on the ratio of these two scales $p_T(Q)/m_Q$, two different models for NLO calculation in perturbative QCD, the fixed-order (FO) and the resummed (RES), are available for heavy quark production.

- The fixed-order (FO) NLO QCD: This model is also known as massive approach. In this model, only light quarks q ($q = u, d$, and s) are present as the

active flavours in the photons. There are no contributing subprocesses initiated by an intrinsic heavy flavour coming directly from the PDF of the photon. The heavy quark is assumed to be massive and produced dynamically in the hard subprocess. The FO NLO QCD has some advantages. In this model not only various distributions like $p_T(Q)$ and the pseudo-rapidity of the heavy quark Q can be predicted but also the total cross section. The separation of the production mechanism into direct, single-resolved, and double-resolved is well defined and meaningful. There is a disadvantage, though, it is reasonable only in the region where the two scales $p_T(Q)$ and m_Q are approximately of the same order. For very high $p_T(Q)$, terms containing $\alpha_s \ln(p_T(Q)^2/m_Q^2)$ may become too large and spoil the convergence of the perturbative series. In this case, the RES NLO QCD model exists as an alternative.

- The resummed (RES) NLO QCD: The potentially large logarithmic terms $\alpha_s \ln(p_T(Q)^2/m_Q^2)$ are properly treated in the RES NLO QCD calculation. In this model, the heavy quark Q is also assumed to be present as an active flavour inside the photon. All the mass singularity terms, occurring as powers of $\alpha_s \ln(p_T(Q)^2/m_Q^2)$, are absorbed into the PDF of the photon and the fragmentation function (FF) of the heavy quark Q, where they can be resummed to all orders using the Altarelli-Parisi equations. This approach is also known as massless approach, in the sense that it does not include the contributions that are suppressed by powers of $m_Q/p_t(Q)$ into the cross section. The RES NLO QCD calculation is expected to produce reasonable predictions only in the high $p_T(Q)$ region, $p_T(Q) \gg m_Q$. The total cross section is not calculable using this model, since it diverges in the limit of $p_T(Q) \to 0$. Moreover, the separation into direct, single-resolved, and double-resolved is not meaningful and only the sum of their contributions corresponds to a physical observable.

The single inclusive distributions predicted by these two models have been used for comparisons with experimental measurements at LEP and elsewhere. Even though the experimental accessible kinematic range is somewhat between the ranges of these two calculations. More details about these two NLO QCD models can be found in [34–37].

2.2.2 Total Cross Section

The cross section for open heavy flavour production (2.7) can be calculated by convoluting the cross section $d\sigma_{\gamma\gamma \to Q\bar{Q}}$ of the $\gamma\gamma \to Q\bar{Q}$ with the Weizsäcker-Williams function f_γ^e

$$d\sigma_{e^+e^- \to e^+e^- Q\bar{Q}} = f_\gamma^e \oplus d\sigma_{\gamma\gamma \to Q\bar{Q}} \oplus f_\gamma^e \quad . \tag{2.8}$$

As mentioned in Sect. 2.1.2, three mechanism (direct, single-resolved, and double-resolved) contribute to the cross section $\sigma_{\gamma\gamma \to Q\bar{Q}}$

$$d\sigma_{\gamma\gamma \to Q\bar{Q}} = d\sigma_{\text{direct}} + d\sigma_{\text{single-resolved}} + d\sigma_{\text{double-resolved}} \quad . \tag{2.9}$$

The resolved contributions require the use of the PDF of the photon, whereas the direct production is free of such non-perturbative input. Detailed NLO QCD calculation for the cross section can be found in [38]. Figures 2.6 and 2.7 show the results of this calculation for charm and bottom productions as functions of the e^+e^- centre-of-mass energy $\sqrt{s}$, separately. Contributions from the three processes involved are also shown in these figures. In the low energy $\sqrt{s}$ range of PETRA/PEP/TRISTAN experiments, the direct production by far dominates the total cross section. However, at LEP 2 energy ($183 - 209\,\text{GeV}$) the direct and single-resolved contributions are comparable, whereas the double-resolved production remains negligible. The bottom production is suppressed by two orders of magnitude because of the heavier mass and smaller absolute charge.

2.2.3 Charm Quark Identification via D^{*+}-tagging

Due to the colour confinement property, parton flavour cannot be directly observed. Perturbative QCD can predict the total cross section as well as the single inclusive distributions for heavy flavour production. However, only the decay products of heavy hadrons containing the heavy quark are directly observed. Experimental measurements require some forms of tag to identify the presence of the heavy quark. There are several techniques available for the tagging of charm quark. Among them, the D^{*+}-tagging method has been frequently employed thanks to its clean and unambiguous signal. This technique exploits the small kinetic energy available in the decay $D^{*+} \to D^0\pi^+$, which yields a very good resolution for the mass difference $\Delta m = m_{D^{*+}} - m_{D^0}$. Taking the invariant masses of the charmed mesons D^{*+} and D^0 given in [40], the mass difference $\Delta m \approx 145.5\,\text{MeV/c}^2$ is just about $6\,\text{MeV/c}^2$ larger than the invariant mass of the π^+, $m_{\pi^+} = 139.6\,\text{MeV/c}^2$. The signal is typically displayed by plotting the Δm distribution for all reconstructed decay product candidates.

The fragmentation of a charm quark of momentum P into a charmed meson D^{*+} of momentum zP involves the process of binding the charm quark c to a $\bar{\text{d}}$ quark, which cannot be perturbatively calculated at the first place. Nevertheless, this process can be described with the help of a non-perturbative fragmentation function (FF) which can be extracted by fitting to experimental data. This analysis uses the so-called Peterson fragmentation function [39] $D_c^{D^{*+}}$

$$D_c^{D^{*+}} = \frac{N_{D^{*+}}}{z}[1 - \frac{1}{z} - \frac{\epsilon_c}{1-z}] \quad , \tag{2.10}$$

where

- the non-perturbative parameter ϵ_c is of the order of $O(m_{\bar{\text{d}}}^2/m_c^2)$ and can be determined from experimental data,
- the normalization factor $N_{D^{*+}}$ are constrained by $\sum_{D^{*+}} \int \text{d}z D_c^{D^{*+}} = 1$.
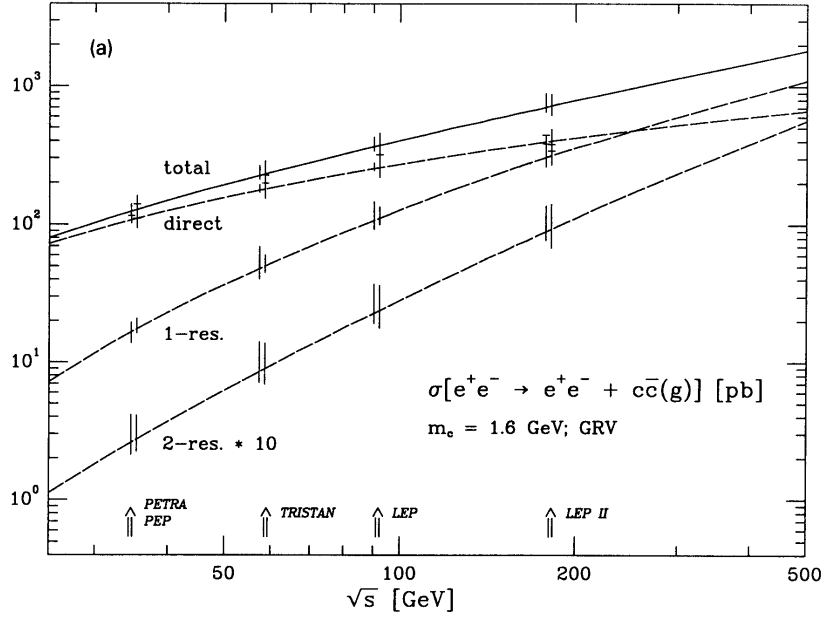
Figure 2.6: Total cross sections for charm production as a function of the e^+e^- centre-of-mass energy $\sqrt{s}$. The total cross section is broken down to the direct, single-resolved (1-res in the figure), and double-resolved (2-res) contributions. This figure is taken from [38].
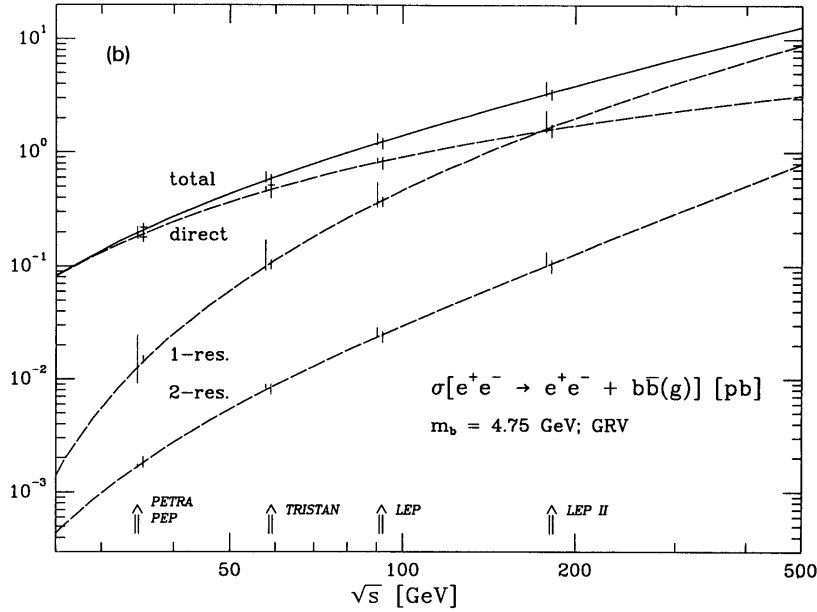

Figure 2.7: Total cross sections for bottom production as a function of the e^+e^- centre-of-mass energy $\sqrt{s}$ [38].

The D^{*+}-tagging method was employed by the ALEPH collaboration in the measurements of the charm production in $\gamma\gamma$ collisions using data collected at LEP 1 energies [41] and a part of LEP 2 data [42, 43]. This present analysis uses the same technique to measure the charm production in $\gamma\gamma$ collisions using the full LEP 2 data available.

2.3 Monte Carlo Generation

In order to simulate the process $e^+e^- \to e^+e^-\gamma\gamma \to e^+e^-c\bar{c} \to e^+e^-D^{*\pm}X$, the leading-order (LO) PYTHIA 6.121 Monte Carlo [44] is used. Events are generated at e^+e^- centre-of-mass energies ranging from $183\,\text{GeV}$ to $209\,\text{GeV}$ using the corresponding integrated luminosities for weighting. Two different samples, direct and single-resolved processes, were generated for each of the considered D^{*+} decay modes using matrix elements for the massive charm quark. The charm quark mass m_c is chosen to be $1.5\,\text{GeV}/\text{c}^2$ and the parameter Λ_{QCD} is set to $0.291\,\text{GeV}/\text{c}^2$. The $\gamma\gamma$ invariant mass $W_{\gamma\gamma}$ is required to be at least $3.875\,\text{GeV}/\text{c}^2$, which is the D$\bar{\text{D}}$ threshold. In order to ensure that both photons are quasi-real, the maximum squared four-momentum transfer Q^2_{max} is limited to $4.5\,\text{GeV}/\text{c}^2$. In the single-resolved process, the SaS-1D [20] parametrization is used for the partonic distribution of the resolved photon. The Peterson et al. parametrization [39] is adopted as the fragmentation function of the charm quark with the nonperturbative parameter $\epsilon_c = 0.031$. The background process $e^+e^- \to e^+e^-\gamma\gamma \to e^+e^-b\bar{b}$ is simulated using PYTHIA 6.121 with $W_{\gamma\gamma}$ being required to be at least $10.5\,\text{GeV}/\text{c}^2$, which is the B$\bar{\text{B}}$ threshold. The b quark mass is set to $4.5\,\text{GeV}/\text{c}^2$. Again the Peterson et al. parametrization is adopted with $\epsilon_b = 0.0035$. Other possible background processes have been simulated using appropriate Monte Carlo generators as listed in Table 4.1. All Monte Carlo samples are generated with full simulation of the ALEPH detector (Sect. 3.2.7). The resulting data are then reconstructed and analysed using the same algorithms as applied to the real data.

Chapter 3

The ALEPH Detector at LEP

3.1 The LEP Collider

The Large Electron Positron (LEP) Collider is located at the Swiss-French border near the city of Geneva. It is part of the CERN laboratory (European Organisation for Nuclear Research). The collider is constructed in an almost circular tunnel with a circumference of 26.7 km, 50 to 150 m below the surface.

Before the electrons and positrons are injected into LEP, they have been accelerated in steps to 20 GeV by four other accelerators. Once they are injected into LEP, the RF (Radio-Frequency) cavities accelerate them to the final beam energy in 8 bunches in opposite directions. At four of the eight short straight sections in the LEP ring, the electrons and positrons are brought into collision. Here, four large experiments are built: ALEPH, DELPHI, L3, and OPAL (Fig. 3.1). LEP was designed to perform precision measurements on the carriers of the electroweak interaction, the Z and W bosons. From 1989 to 1995, LEP ran at centre-of-mass energies around 91 GeV, the mass of the Z boson (LEP1). Since the fall of 1995 onwards, superconducting RF cavities were installed to raise the centre-of-mass energy in steps to 209 GeV (LEP2).

The data analyzed in this analysis were collected by the ALEPH detector at e^+e^- centre-of-mass energies ranging from 183 GeV to 209 GeV in the data taking period from 1997 to 2000.

3.2 The ALEPH Detector at LEP

The ALEPH detector has been described in detail in [45–48]. Here, only the parts essential to the present analysis are described briefly. A cut-away view showing the detector is shown in Fig. 3.2. It is a collection of independent and modular subdetectors. In being so, the ALEPH detector as a whole can be sensitive to almost every known elementary particle.
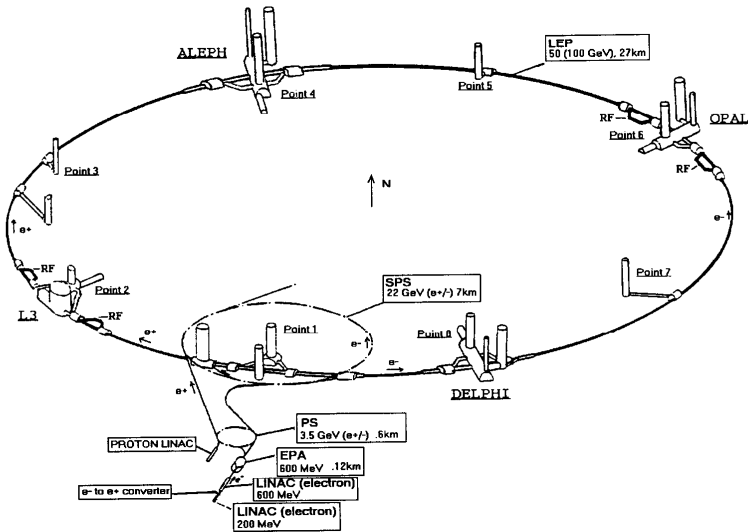
Figure 3.1: The LEP ring and the location of the four LEP experiments.
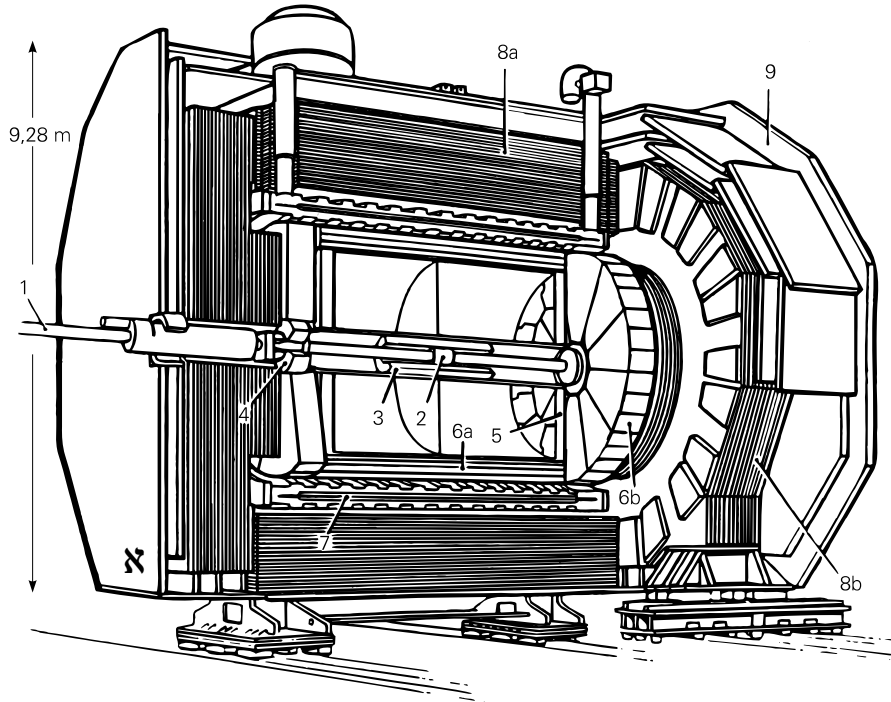
Figure 3.2: The ALEPH detector: (1) beam pipe, (2) silicon vertex detector (VDET), (3) inner tracking chamber (ITC), (4) luminosity monitor, (5) time projection chamber (TPC), (6a and 6b) electromagnetic calorimeter (ECAL), (7) superconducting solenoid, (8a and 8b) hadron calorimeter (HCAL), and (9) the muon chambers.

3.2.1 Tracking Subdetectors

The central part of the ALEPH detector is dedicated to the reconstruction of the trajectories of charged particles. The trajectory of a charged particle emerging from the interaction point is measured by a two-layer silicon strip vertex detector (VDET), a cylindrical drift chamber (ITC) and a large time projection chamber (TPC). The three tracking detectors are immersed in a $1.5\,\mathrm{T}$ axial magnetic field provided by a superconducting solenoidal coil. Together they measure charged particle transverse momenta with a resolution of $\delta p_\mathrm{t}/p_\mathrm{t} = 6 \times 10^{-4} p_\mathrm{t} \oplus 0.005$ (p_t in GeV/c). The TPC also provides a measurement of the specific ionization $\mathrm{d}E/\mathrm{d}x_\mathrm{meas}$. An estimator may be formed to test a particle hypothesis, $\chi_\mathrm{h} = (\mathrm{d}E/\mathrm{d}x_\mathrm{meas} - \mathrm{d}E/\mathrm{d}x_\mathrm{exp,h})/\sigma_\mathrm{exp,h}$, where $\mathrm{d}E/\mathrm{d}x_\mathrm{exp,h}$ and $\sigma_\mathrm{exp,h}$ denote the expected specific ionization and the estimated uncertainty for the particle hypothesis h, respectively.

3.2.2 Calorimeters

The electromagnetic calorimeter (ECAL) is situated between the TPC and the coil. It is a lead/proportional-tube sampling calorimeter segmented in $0.9° \times 0.9°$ projective towers read out in three sections in depth. It has a total thickness of 22 radiation lengths and yields a relative energy resolution of $0.18/\sqrt{E} + 0.009$, with E in GeV, for isolated photons. Electrons and photons are identified by their transverse and longitudinal shower profiles in ECAL.

The iron return yoke is instrumented with 23 layers of streamer tubes and forms the hadron calorimeter (HCAL). The latter provides a relative energy resolution of charged and neutral hadrons of $0.85/\sqrt{E}$, with E in GeV. The HCAL is used to identify hadrons by distinguishing the characteristic hadronic shower from the cleaner penetration of muon.

3.2.3 Muon Chambers

The muon chambers are composed of two double-layers of streamer tubes outside HCAL. Together with the HCAL, the muon chambers are used to identify muons with high efficiency.

3.2.4 Luminosity and Beam Monitoring

Two small angle luminosity calorimeters, the silicon luminosity calorimeter (SICAL) and the luminosity calorimeter (LCAL), are particularly important for this analysis to veto events with detected scattered electrons. The LCAL is a lead/wire calorimeter, similar to ECAL, placed around the beam pipe at each end of the detector. It monitors angles from 45 to 160 mrad with an energy resolution of $0.15 \cdot \sqrt{E(\mathrm{GeV})}$. The SICAL uses 12 silicon/tungsten layers to sample showers. It is mounted around the beam pipe in front of the LCAL, covering angles from 34 to 58 mrad. An energy resolution of $0.225 \cdot \sqrt{E(\mathrm{GeV})}$ is achieved.

The instantaneous luminosity is provided by the very small angle luminosity monitor, known as the BCAL. This consists of two opposite pairs of detectors placed 7.7 m from the interaction point and detects 20 times more Bhabha events than SICAL does due to its larger acceptance at smaller polar angle.

A small angle monitor of the background (SAMBA) is positioned in front of the LCAL at either end of the detector. It consists of two multi-wire proportional chambers. Information provided by the SAMBA is used to optimize the beam conditions.

3.2.5 Triggering

The ALEPH triggering system is organised into 3 levels. Signals from various subdetectors are used as input to the trigger decision.

- LVL1 Level 1 trigger (LVL1) decides whether or not to read out all detector elements. There are several types of LVL 1 trigger conditions. One type involves a coincidence between tracks in the ITC and energy deposited in the ECAL. Triggers based only on energy deposited into the ECAL barrel and/or endcaps also exist. Analogously, several trigger conditions use information from the ITC and HCAL. Signals from the LCAL and muon chambers are employed to set up luminosity and muon hit triggers, respectively.
- LVL2 The level 2 trigger (LVL2) simply verifies the level 1 decisions concerning charged particles by replacing the ITC tracking information with the more accurate TPC tracking information.
- LVL3 The level 3 trigger (LVL3) is performed by software to reject background such as beam gas interactions and off-momentum events. A series of dedicated Event Processors analyze the full ensemble of data to verify LVL 1 and LVL 2.

3.2.6 Energy-Flow Objects

The informations from the tracking detectors and the calorimeters are combined in an energy-flow algorithm [46]. For each event, the algorithm provides a set of charged and neutral reconstructed particles, called *energy-flow objects* in the following.

3.2.7 Detector Simulation

The ALEPH detector is simulated using a complex package called GALEPH [49]. The heart of GALEPH is the CERN Monte Carlo package GEANT [50,51]. GALEPH combines GEANT with the geometrical and electronic model of ALEPH to simulate the response of the detector to high energy particles. The resulting simulated data can be reconstructed and analysed in exactly the same way as real data.

Chapter 4

Inclusive D$^{*\pm}$ Production in Two-Photon Events

The inclusive production of D$^{*\pm}$ mesons in two-photon collisions is measured with the ALEPH detector at e$^+$e$^-$ centre-of-mass energies ranging from $183\,\mathrm{GeV}$ to $209\,\mathrm{GeV}$ with an integrated luminosity $\mathcal{L}$ of $699\,\mathrm{pb}^{-1}$. Contributions from the main processes involved are separated using event shape variables. Differential cross sections of D$^{*\pm}$ production as function of the transverse momentum $p_\mathrm{t}^{\mathrm{D}^{*+}}$ and of the pseudorapidity $\eta^{\mathrm{D}^{*+}}$ of the D$^{*\pm}$ meson are measured in the range $2\,\mathrm{GeV}/c < p_\mathrm{t}(D^{*\pm}) < 12\,\mathrm{GeV}/c$ and $|\eta^{\mathrm{D}^{*+}}| < 1.5$. They are compared to next-to-leading order (NLO) perturbative QCD calculations. The extrapolation of the integrated visible D$^{*\pm}$ cross section to the total charm cross section is performed.

4.1 Two-Photon Events Selection

Two-photon events, $\gamma\gamma \rightarrow hadrons$, are separated from background events coming from processes other than two-photon. The possible background processes considered in this analysis have been simulated using appropriate Monte Carlo generators as indicated in Table 4.1. The following selection criteria were defined using several event variables based upon the ALEPH energy-flow object package [46] and were motivated by Monte Carlo studies.

- Two-photon events have smaller invariant mass in comparison to annihilation events. That is due to the fact that the beam electrons transfer only a small fraction of their energies to the radiated photons. Figure 4.1 shows the visible invariant mass W_vis distributions for the $\gamma\gamma \rightarrow c\bar{c}$ signal and considered background processes. A major part of annihilation background was rejected by requiring that W_vis must be less than $55\,\mathrm{GeV}/c^2$. Additionally, since at the very low-end of the W_vis distribution e$^+$e$^- \rightarrow$ e$^+$e$^-\tau^+\tau^-$ is the dominant process and more importantly two-photon events are poorly reconstructed in this region, the W_vis was required to be at least $4\,\mathrm{GeV}/c^2$.

4. Inclusive $D^{*\pm}$ Production in Two-Photon Events

Process	Monte Carlo Generator
$e^+e^- \to q\bar{q}$	PYTHIA 5.7 [44]
$e^+e^- \to W^+W^-$	KORALW 1.21 [52]
$e^+e^- \to \tau^+\tau^-$	KORALZ 4.2 [53]
$e^+e^- \to e^+e^-\tau^+\tau^-$	PHOT02 [54]

Table 4.1: Considered background processes and associated Monte Carlo generators

Year	$\sqrt{s_{e^+e^-}}$ (GeV)	$\mathcal{L}$ (pb^{-1})	Number of selected $\gamma\gamma$-events
1997	183	59.18	425 284
1998	189	177.08	1 225 333
1999	192-204	241.61	1 703 451
2000	200-209	219.99	1 605 536

Table 4.2: Number of selected $\gamma\gamma$-events in the analysed data samples together with their corresponding e^+e^- centre-of-mass energies and integrated luminosities $\mathcal{L}$.

- The total energy of charged particles E_{ch}, defined as the sum of energies of all final-state charged particles, is shown in Fig. 4.2. The annihilation and W-pair productions dominate over two-photon process at large E_{ch}, therefore E_{ch} should not exceed $35\,\text{GeV}$ for an event to be kept.

- The visible transverse momentum $p_{\text{t,vis}}$ of the the final state, shown in Fig. 4.3, is required to be less than $8\,\text{GeV}/c$, as the $p_{\text{t,vis}}$ distribution has a much longer tail for all considered background processes.

- The event must contain at least 3 charged particles, $N_{\text{ch}} \geq 3$, in order to be retained. This cut reduces the background coming from $e^+e^- \to e^+e^-l^+l^-$ ($l = e, \mu, \tau$) processes. The charged multiplicity distribution, N_{ch}, is shown in Fig. 4.4.

- Figure 4.5 shows the scatter plot N_{ch} vs. the total visible energy, E_{vis}, of the event for signal and considered background processes. A cut combining these two quantities is applied: $N_{\text{ch}} < 40 - \frac{2}{3}E_{\text{vis}}(\text{GeV})$.

- Finally, in order to select only events with almost on-shell photons an anti-tagging condition was applied, i.e. tagged events were rejected. A tag in this analysis is defined as an energy-flow object in the luminosity calorimeters (LCAL or SICAL) with an energy of at least $30\,\text{GeV}$.

This selection retains a sample of more than 4.9 million events (Table 4.2). Monte Carlo studies on possible background sources predict a $\gamma\gamma$ purity of 98.8%.
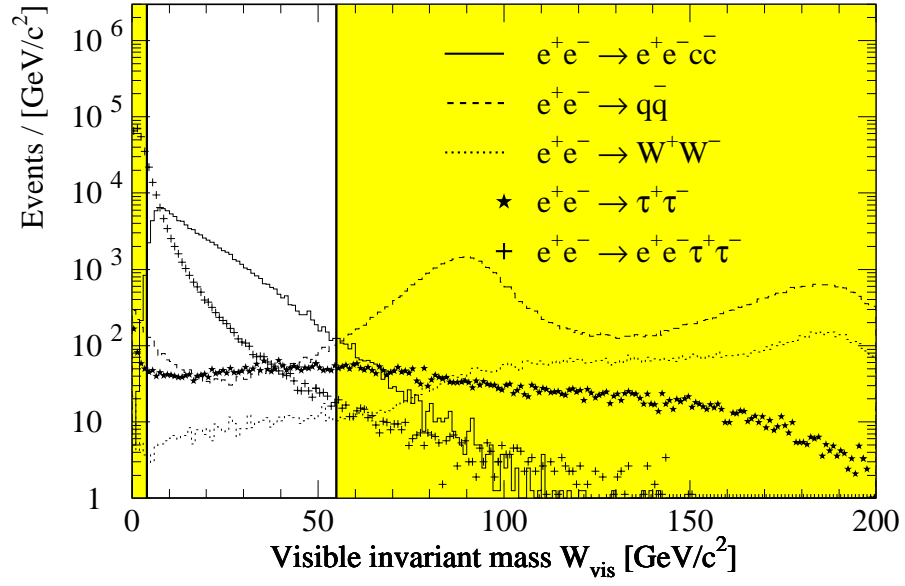
Figure 4.1: The visible invariant mass W_{vis} of the final state for the signal process, $\gamma\gamma \to c\bar{c}$, and all considered background processes. Their luminosities were normalized to the total integrated luminosity of the analysed data sample (699 pb^{-1}). The shaded areas are rejected.
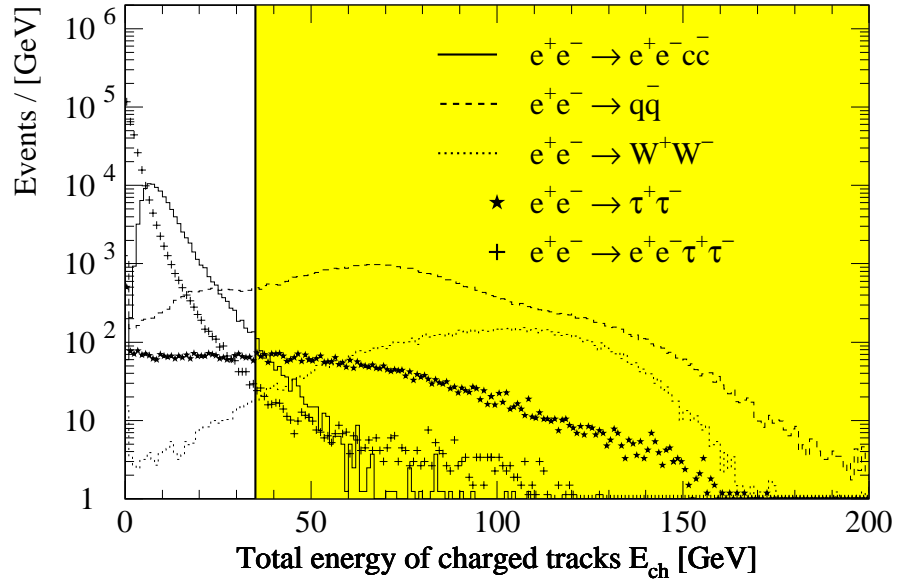
Figure 4.2: The total energy of charged particles E_{ch}.
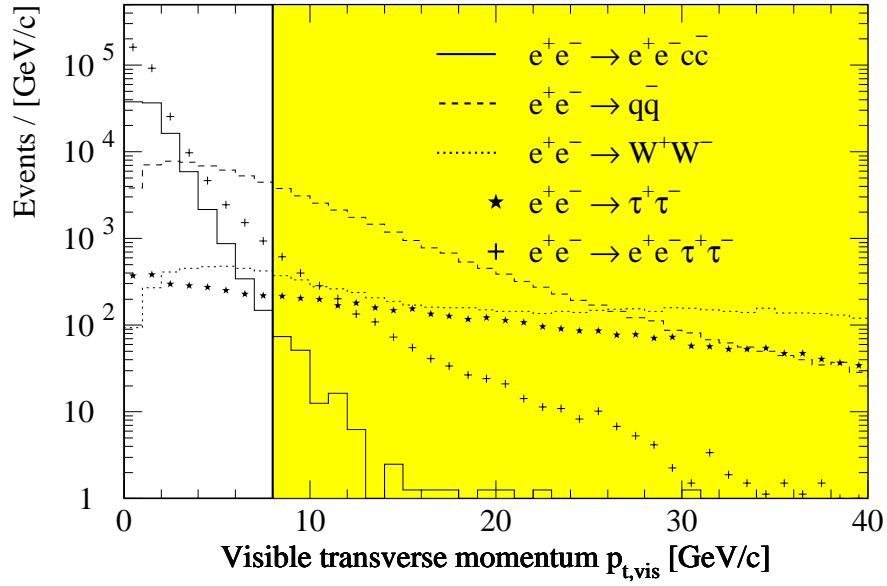
Figure 4.3: The visible transverse momentum of the final state $p_{t,\text{vis}}$.
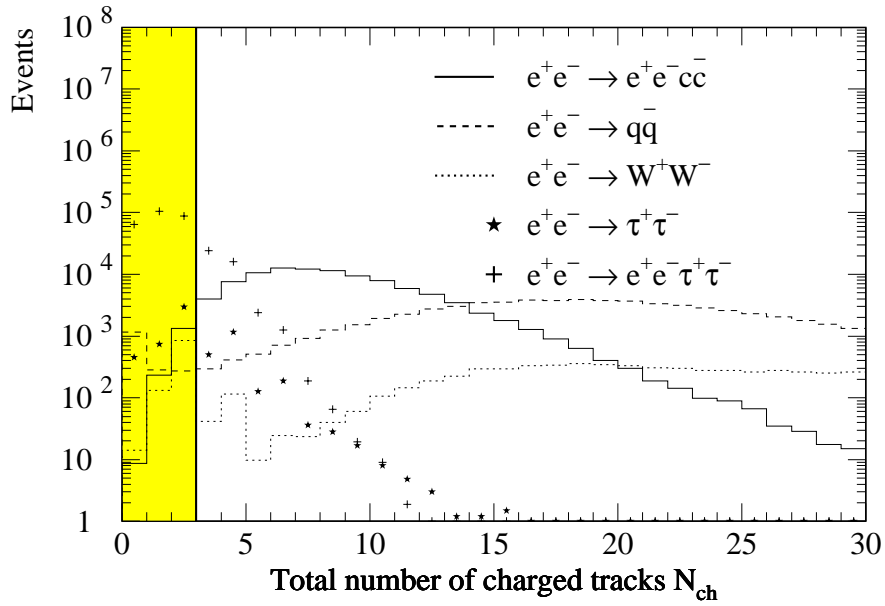
Figure 4.4: Charged multiplicity N_{ch}.
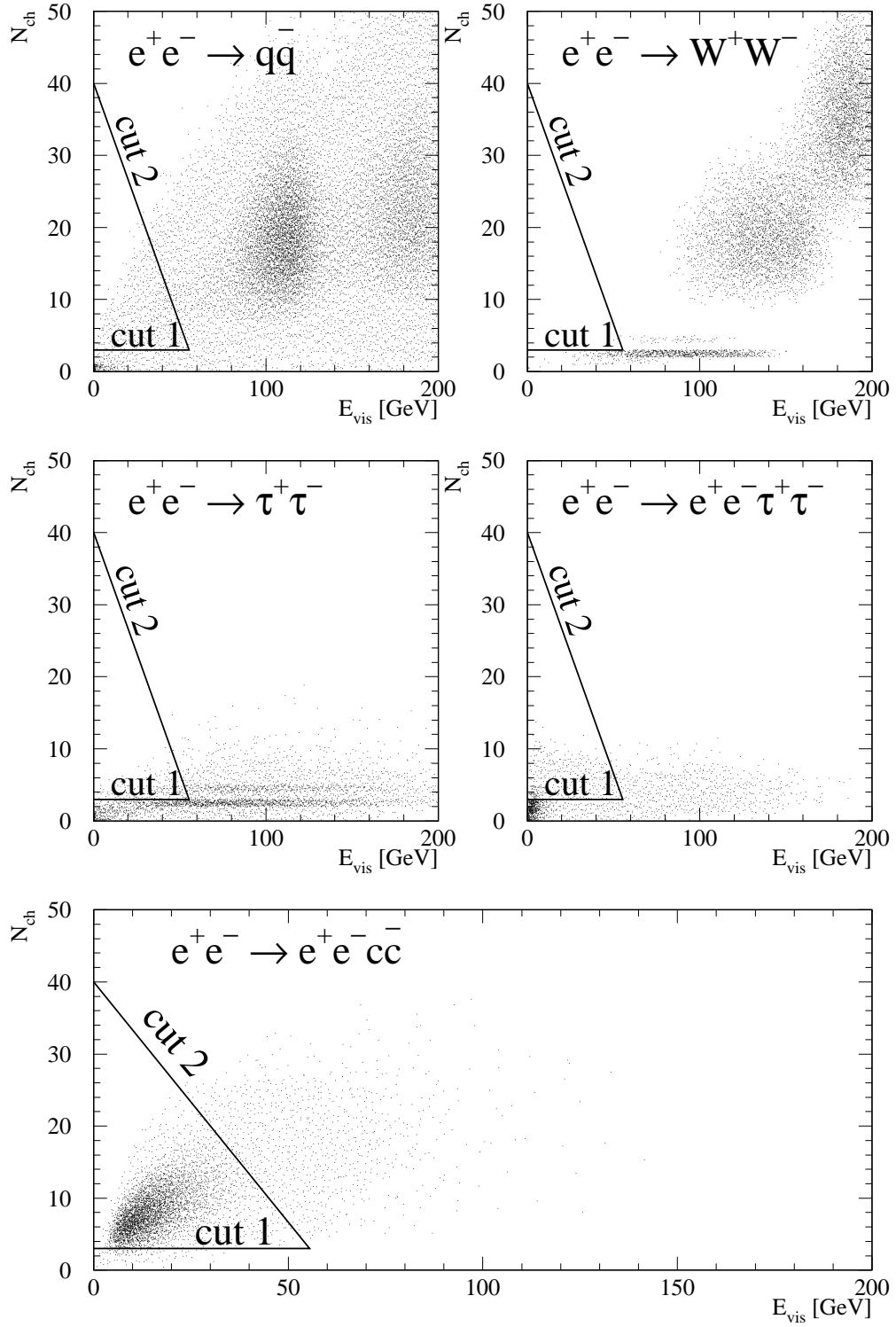
Figure 4.5: The scatter plots: total number of charged particles N_{ch} as a function of the total visible energy E_{vis} for signal and considered background processes. The triangular area defined by cut 1, $N_{\text{ch}} \geq 3$, and cut 2, $N_{\text{ch}} < 40 - \frac{2}{3}E_{\text{vis}}(\text{GeV})$, is selected.

4.2 D$^{*\pm}$ Meson Selection

Having selected a sample of two-photon events, the tagging of charmed quarks is performed using exclusively reconstructed D^{*+} mesons in their dominant decay to D$^0\pi^+$ with the D^0 mesons being identified in the following three decay modes (branching ratios given in parentheses from [40]):

(1) D$^0 \to$K$^-\pi^+$ $(3.85 \pm 0.09)\%$,

(2) D$^0 \to$K$^-\pi^+\pi^0$ $(13.9 \pm 0.9)\%$,

(3) D$^0 \to$K$^-\pi^+\pi^+\pi^-$ $(7.6 \pm 0.4)\%$.

Charge conjugated particles and their decays are implicitly included throughout this thesis.

The favourable aspect of the decay D$^{*+} \to$ D$^0\pi^+$ is that the available kinetic energy is only about $6\,\mathrm{MeV}$ for the decay products in the rest-frame of the D^{*+}. That is due to the small mass difference of the D^{*+} and D^0 mesons ($\Delta m = m_{\mathrm{D}^{*+}} - m_{\mathrm{D}^0} = 145.5\ \mathrm{MeV}/c^2$). A clean signal is obtained by plotting the Δm for all reconstructed candidates.

4.2.1 D^{*+} Meson Reconstruction

Charged Particle Selection

As a basis for possible K$^\pm$ and $\pi^\pm$ candidates well-reconstructed tracks of charged particles are selected. Well-reconstructed tracks are defined as originating from the vicinity of the interaction point with transverse impact parameter $|d_0| < 2\,\mathrm{cm}$ and longitudinal impact parameter $|z_0| < 8\,\mathrm{cm}$, having at least four TPC hits, a polar angle θ with respect to the beam axis in the range $20° < \theta < 160°$ and a momentum of at least $100\,\mathrm{MeV}/c$. The related distributions are shown in Fig. 4.6. Having survived the selection criteria above, charged particles are identified by a simultaneous measurement of their specific ionization energy loss $\mathrm{d}E/\mathrm{d}x$ and momentum p in the TPC. Figure 4.7 shows the scatter-plot of $\mathrm{d}E/\mathrm{d}x$ versus momentum p for all selected tracks in the data sample. Superimposed on that figure are the expected specific energy loss curves for various particle species: e, π, K, p and d. The measurement errors cause the measured $\mathrm{d}E/\mathrm{d}x$ to spread over a certain range forming a broad band around the expected ionisation curves. At low momentum these bands are well separated allowing particles to be identified individually. But over the significant range of momentum they overlap each other making an unambiguous individual identification impossible and a statistical method has to be applied. An estimator χ_h can be formed to test a particle hypothesis h:

$$\chi_\mathrm{h} = \left(\frac{\mathrm{d}E/\mathrm{d}x_\mathrm{meas} - \mathrm{d}E/\mathrm{d}x_\mathrm{exp,h}}{\sigma_\mathrm{exp,h}} \right) \quad , \tag{4.1}$$
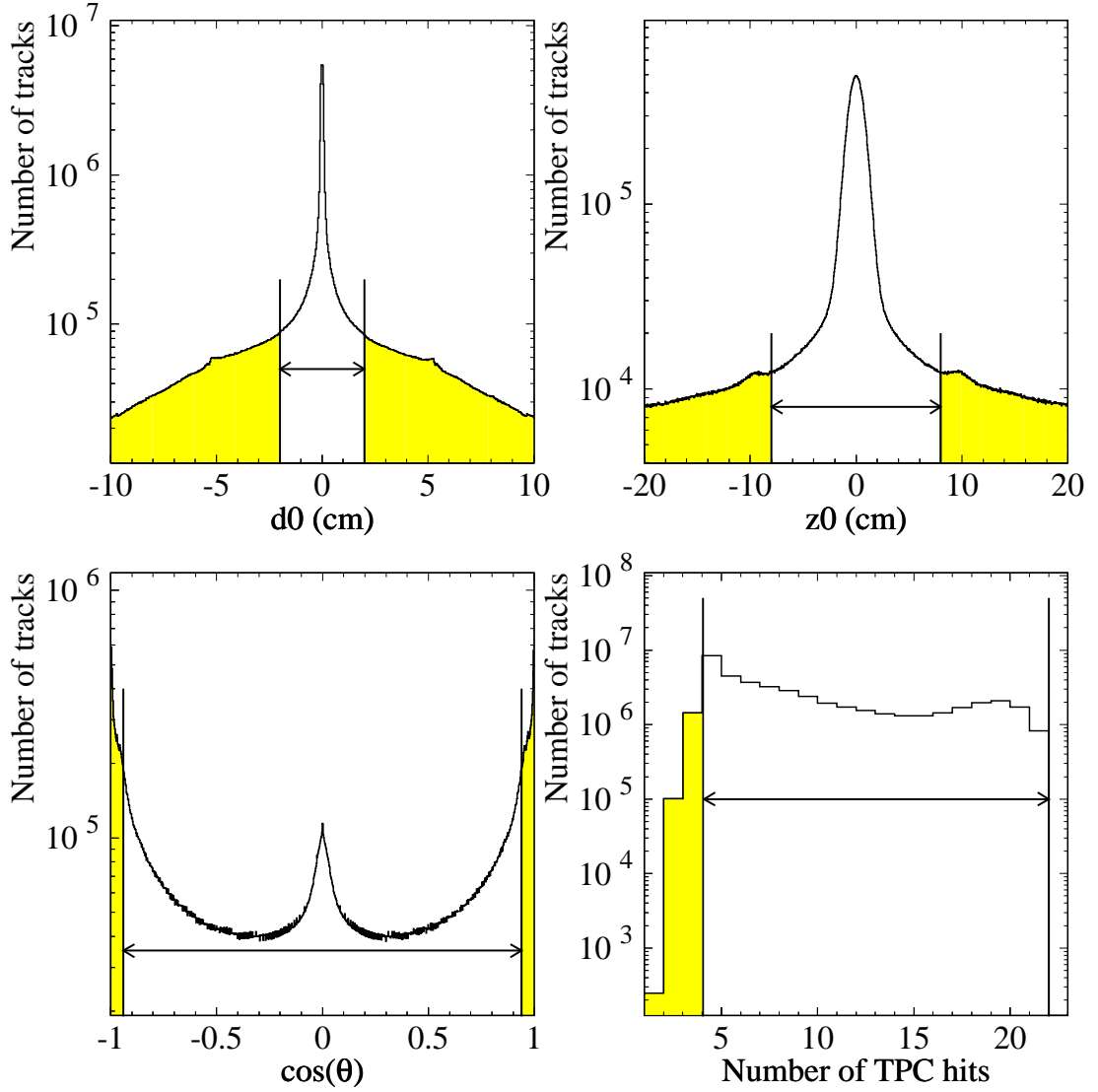
Figure 4.6: Quality parameters of the reconstructed tracks of charged particles: the transverse and longitudinal impact parameters $|d_0|$ and $|z_0|$, $\cos\theta$ and number of hits in the TPC. The shaded areas are rejected.

where $dE/dx_{\text{exp,h}}$ and $\sigma_{\text{exp,h}}$ denote the expected specific energy loss and its estimated uncertainty for the particle hypothesis h, respectively. Using the estimator χ_{h}, one can judge on whether the tested mass hypothesis is accepted or not, by relying on the χ_{h} values itself or calculating χ^2-probability, $P_{\text{h}}(\chi_0^2)$. The later quantity can be calculated with one degree of freedom by integrating the normalised χ^2-distribution

$$P_{\text{h}}(\chi_0^2) = \int_{\chi_0^2}^{\infty} P_1(z)dz \quad . \tag{4.2}$$
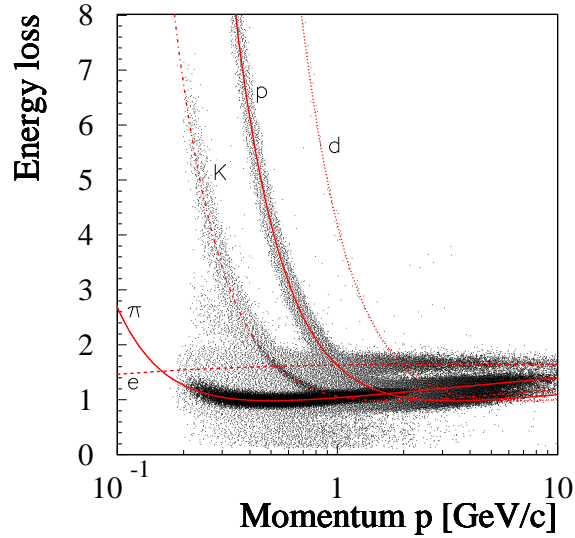
Figure 4.7: Energy loss $\mathrm{d}E/\mathrm{d}x$ as a function of momentum p for all selected charged particles. Also shown are the expected $\mathrm{d}E/\mathrm{d}x$ curves for e, π, K, p and d.
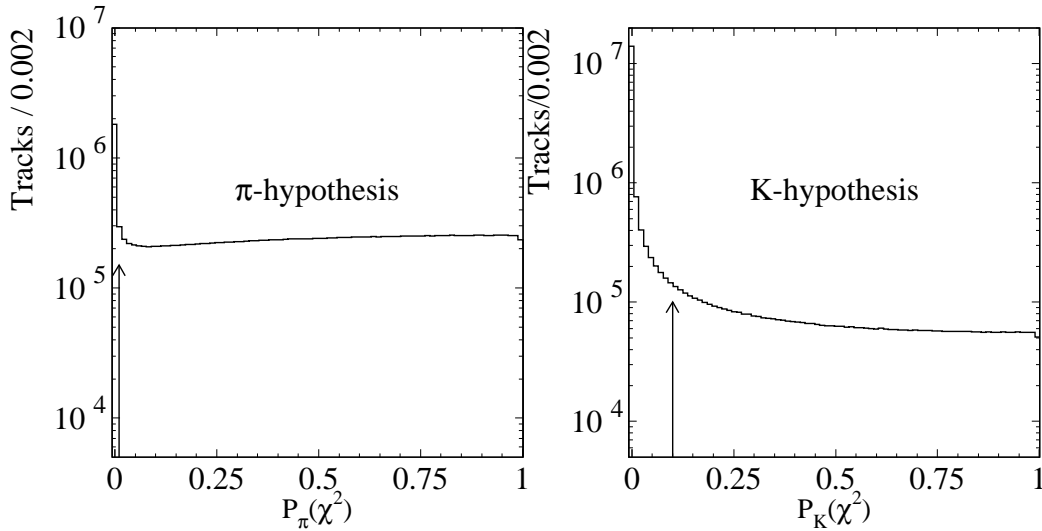
Figure 4.8: The χ^2-probability distribution for pion and kaon mass hypotheses. The arrows indicate the selection cuts.

The χ^2-probability P_K and P_π distributions for K and π mass hypotheses are shown in Fig. 4.8. A charged particle is classified as a K$^+$ if the corresponding probability P_K is greater than 10% and as a pion if P_{π^+} is at least 1% . Thus, each track can be flagged as a kaon or pion or both or neither.

π^0 **Reconstruction**

The π^0 candidates are formed from pairs of photons found in ECAL with an energy E_γ of at least $250\,\mathrm{MeV}$ each and an invariant mass $m_{\gamma\gamma}$ within $85\,\mathrm{MeV}/c^2$ of the nominal π^0 mass. The invariant mass $m_{\gamma\gamma}$ distribution is shown in Fig. 4.9 in which a clear signal of the π^0 meson is seen. In order to improve the energy resolution of these π^0s the energies of the photons are refitted using the π^0 mass as constraint. If the confidence level of this fit is greater than 5% (Fig. 4.10) and if $|\cos\theta_{\pi^0}| < 0.93$, where θ_{π^0} is the polar angle of the π^0 candidate with respect to the beam axis, the π^0 candidate is retained.
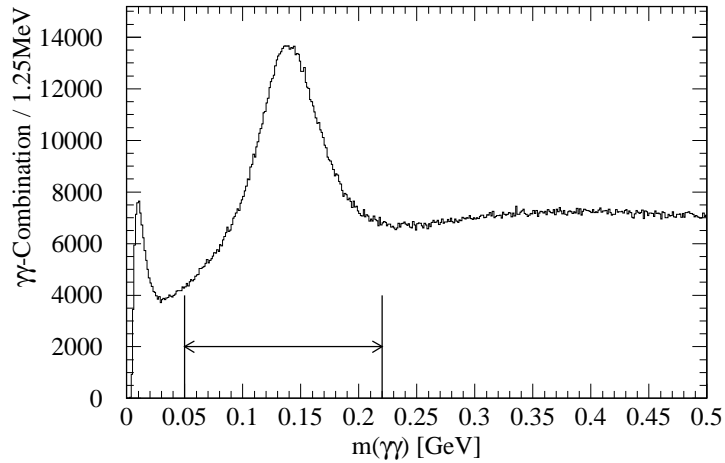
Figure 4.9: Invariant mass $m_{\gamma\gamma}$ distribution. The acceptance mass range used to classify the π^0 candidate, $50\,\mathrm{MeV}/c^2 < m_{\gamma\gamma} < 220\,\mathrm{MeV}/c^2$, is also indicated.
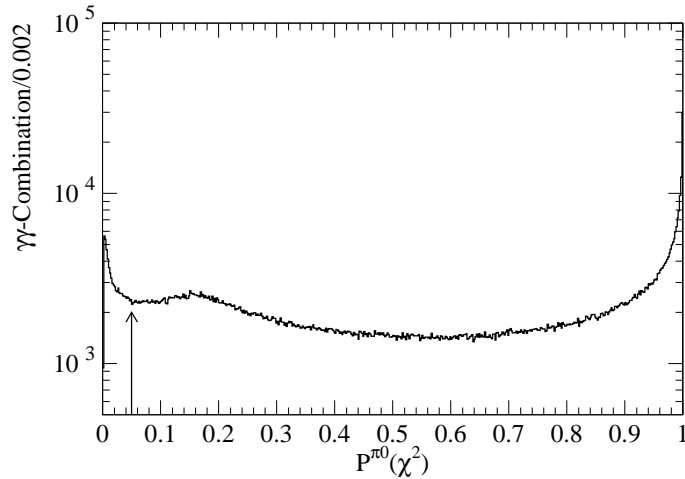
Figure 4.10: The χ^2-probability of the mass-constraint fit.
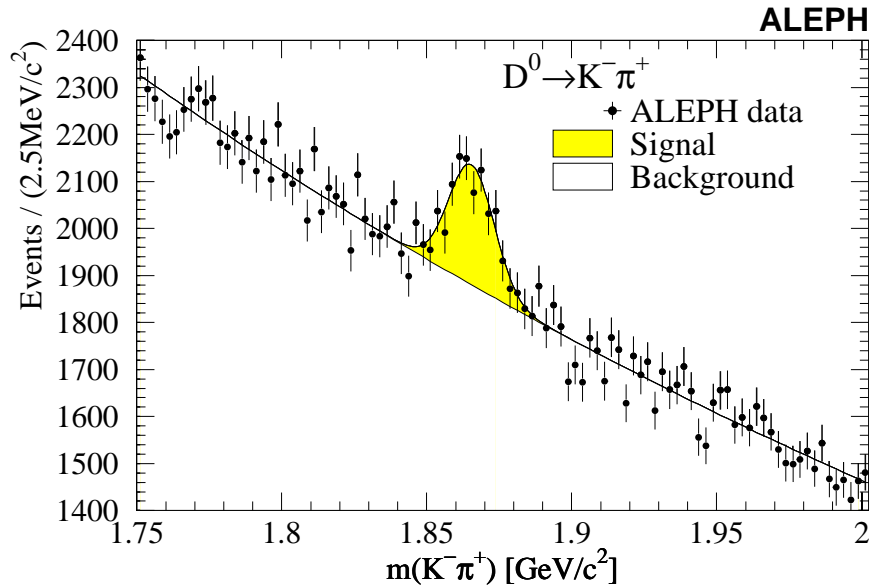
Figure 4.11: The invariant mass distribution reconstructed in the decay mode $D^0 \to K^-\pi^+$. The distribution was fitted by a Gaussian representing the D^0 signal and an exponential describing the background.

D^0 Selection

The D^0 candidates are formed from appropriate combinations of identified kaons and pions according to the three considered decay modes (1) $K^-\pi^+$, (2) $K^-\pi^+\pi^0$, and (3) $K^-\pi^+\pi^-\pi^+$. In order to reduce the combinatorial background in mode (3) the four tracks composing the D^0 are fitted to a common vertex and the probability of this fit is required to be greater than 0.2%. A clear D^0 signal is visible only in the decay mode $D^0 \to K^-\pi^+$ due to its low multiplicity and therefore low combinatorial background (Fig. 4.11). The invariant mass of D^0 candidates reconstructed in the analysed data is shown in Fig. 4.12 for the three considered decay modes separately.

The D^0 candidate is retained if it has an invariant mass within $20\,\mathrm{MeV}/c^2$, $65\,\mathrm{MeV}/c^2$, and $20\,\mathrm{MeV}/c^2$ of the nominal D^0 mass, $m_{D^0} = 1864.4\,\mathrm{MeV}/c^2$ [40], for decay mode (1), (2), and (3), respectively. The acceptance mass ranges used in each decay mode to classify D^0 candidates were set according to the mass resolution determined in the Monte Carlo simulation of the detector. The invariant mass distributions of the D^0 mesons simulated by the PYTHIA Monte Carlo is shown in Fig. 4.13. The wider acceptance mass range for the decay mode $D^0 \to K^-\pi^+\pi^0$ reflects the poor resolution of the reconstructed π^0 meson (Fig. 4.13 and Table. 4.3).
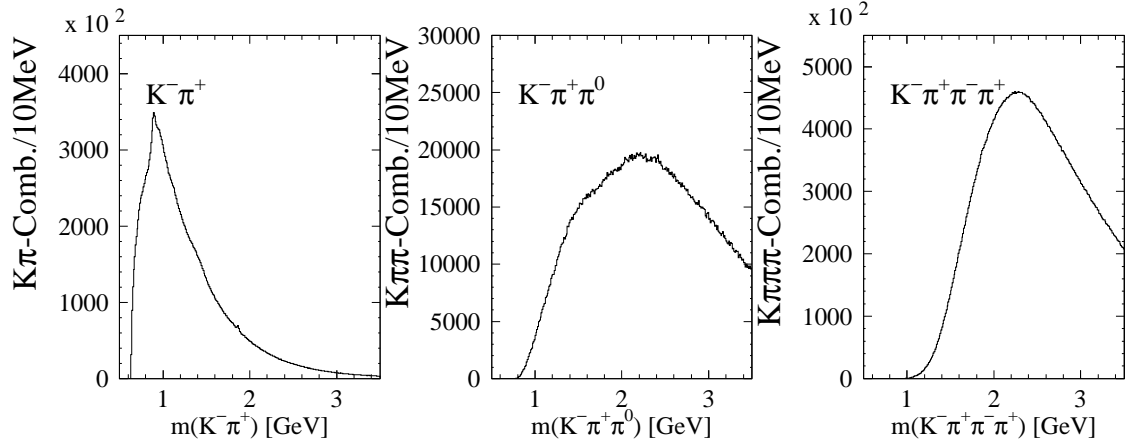
Figure 4.12: Invariant mass m_{D^0} distributions for three considered decay modes (1) $K^-\pi^+$, (2) $K^-\pi^+\pi^0$, and (3) $K^-\pi^+\pi^-\pi^+$ in the analysed data.
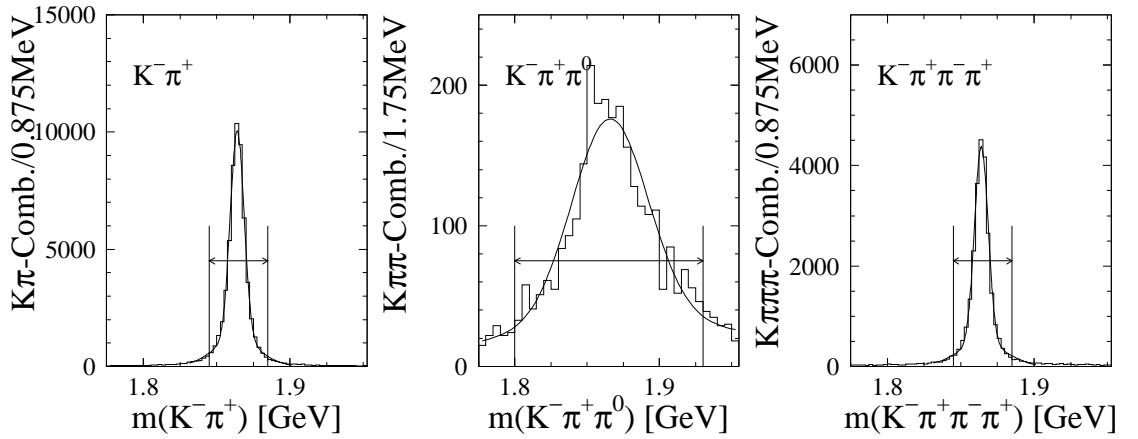
Figure 4.13: Invariant mass m_{D^0} distributions for the three considered decay modes in the Monte Carlo simulation. The acceptance mass ranges for D^0 candidates in each decay mode are also indicated.

Decay mode	σ(GeV)	Accepted mass range (MeV/c^2)
$D^0 \to K^-\pi^+$	4.73 ± 0.04	1845-1885
$D^0 \to K^-\pi^+\pi^0$	26.9 ± 1.1	1800-1930
$D^0 \to K^-\pi^+\pi^-\pi^+$	4.62 ± 0.05	1845-1885

Table 4.3: The mass resolution of the reconstructed D^0 mesons simulated by the PYTHIA Monte Carlo for the considered decay modes. The acceptance mass ranges used to select D^0 candidates are given in the last column.

4.2.2 D$^{*\pm}$ Extraction

Having selected a D^0 candidate each combination of this D^0 with one of the remaining π^+ candidates is considered to be a D^{*+} candidate. In order to reduce combinatorial background and to limit the kinematic range of the D^{*+} to the acceptance range of the detector with reasonable efficiency, cuts were applied to the transverse momentum $p_{\mathrm{t}}^{\mathrm{D}^{*+}}$ and the pseudorapidity $\eta = -\ln(\tan(\theta/2))$ of the D^{*+}:

$$2\,\mathrm{GeV}/c < p_{\mathrm{t}}^{\mathrm{D}^{*+}} < 12\,\mathrm{GeV}/c\,, \quad |\eta^{\mathrm{D}^{*+}}| < 1.5 \quad . \tag{4.3}$$

The restriction imposed on $|\eta^{\mathrm{D}^{*+}}|$ implies that the polar angle $\theta_{\mathrm{D}^{*+}}$ of the D^{*+} candidate with respect to the beam axis must be in the range of $25° < \theta_{\mathrm{D}^{*+}} < 155°$. The upper limit on the $p_{\mathrm{t}}^{\mathrm{D}^{*+}}$ is formally applied since there is no D^{*+} candidate found in the analysed data beyond $12\,\mathrm{GeV}/c$. If there are several D^{*+} candidates found in one event the corresponding D^0 candidates are compared in mass and only the candidate with its D^0 mass nearest to the value given in [40] is retained. If two or more D^{*+} candidates share the same D^0 candidate all of them are retained. As a result, there is only one D^{*+} candidate per event in the signal region.

For D^{*+} candidates selected by this procedure the mass difference $\Delta m = m_{\mathrm{D}^{*+}} - m_{\mathrm{D}^0}$ is calculated. Figure 4.14 shows the Δm distribution for all the three considered decay modes together. The spectrum rises at the lower threshold given by the charged pion mass. A clear peak is seen at $145.5\,\mathrm{MeV}/c^2$. In order to extract the number of D^{*+} events the data distribution is fitted with the following parametrization:

$$F(\Delta m) = N \left[\frac{1}{\sqrt{2\pi}\sigma} \exp\left\{ -\frac{1}{2}\left(\frac{\Delta m - 145.5\,\mathrm{MeV}/c^2}{\sigma}\right)^2 \right\} + C\,(\Delta m - m_{\pi^+})^P \right] \quad . \tag{4.4}$$

where the Gaussian describes the D^{*+} signal and the combinatorial background is represented by the power-law function. In order to exclude systematic binning effects an unbinned likelihood fit is performed where C and P are used as free parameters. The normalization N follows from the normalization constraint that the integral of $F(\Delta m)$ over the range of the fit, $130\,\mathrm{MeV}/c^2 < \Delta m < 200\,\mathrm{MeV}/c^2$, has to be equal to the number of entries in this region. The width σ of the Gaussian describing the peak is fixed to $0.5\,\mathrm{MeV}/c^2$, as determined in Monte Carlo studies. The number of D^{*+} events is then obtained by integrating the Gaussian part of (4.4) in the range of $145.5\,\mathrm{MeV}/c^2 \pm 3\sigma$,

$$144.0\,\mathrm{MeV}/c^2 < \Delta m < 147.0\,\mathrm{MeV}/c^2 \quad . \tag{4.5}$$

In the data sample analyzed a total number of $(360 \pm 27\,(\mathrm{stat.}))$ D^{*+} events are observed for all three considered decay modes together.

Among the possible background processes, only the contribution from the process $\gamma\gamma \to b\bar{b} \to \mathrm{D}^{*\pm}X$ is found to be sizeable. This contribution is estimated
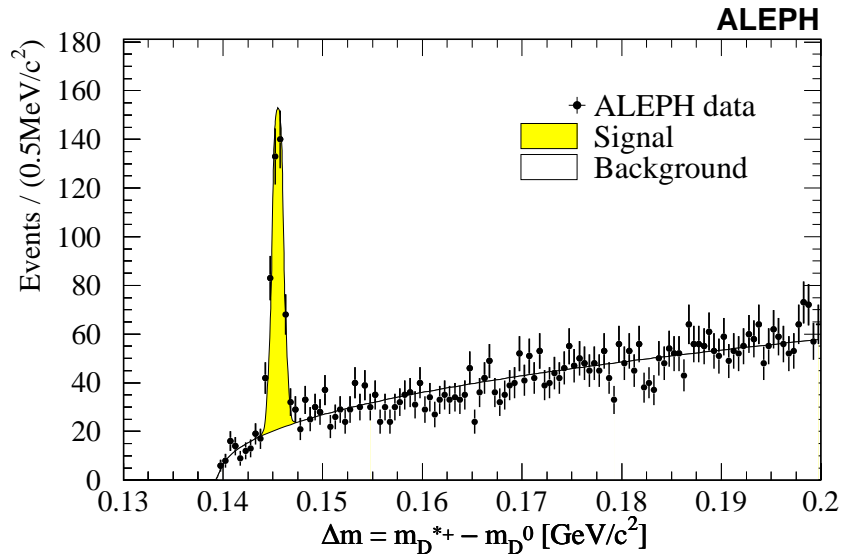
Figure 4.14: Mass difference of reconstructed D^{*+} and D^0 candidates for all considered D^0 decay modes together. The points show ALEPH data, the error bars represent statistical uncertainties, and the solid line describes the result of an unbinned likelihood fit.
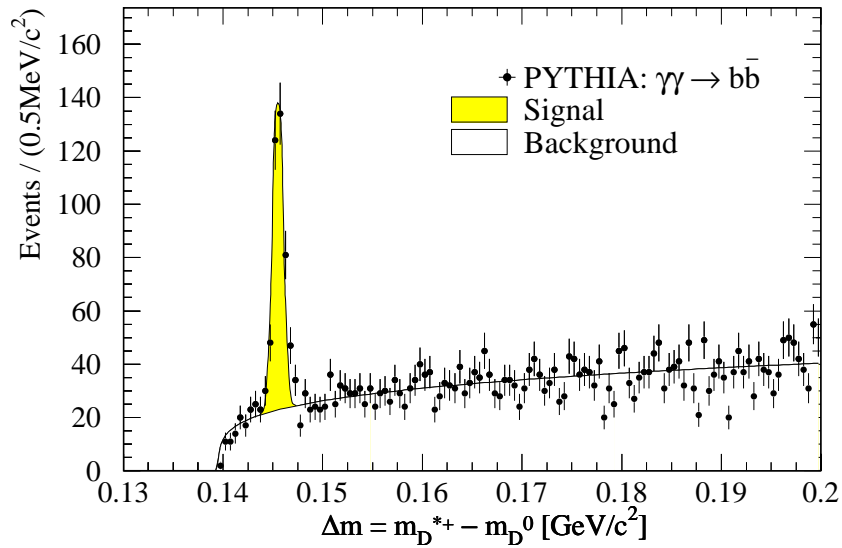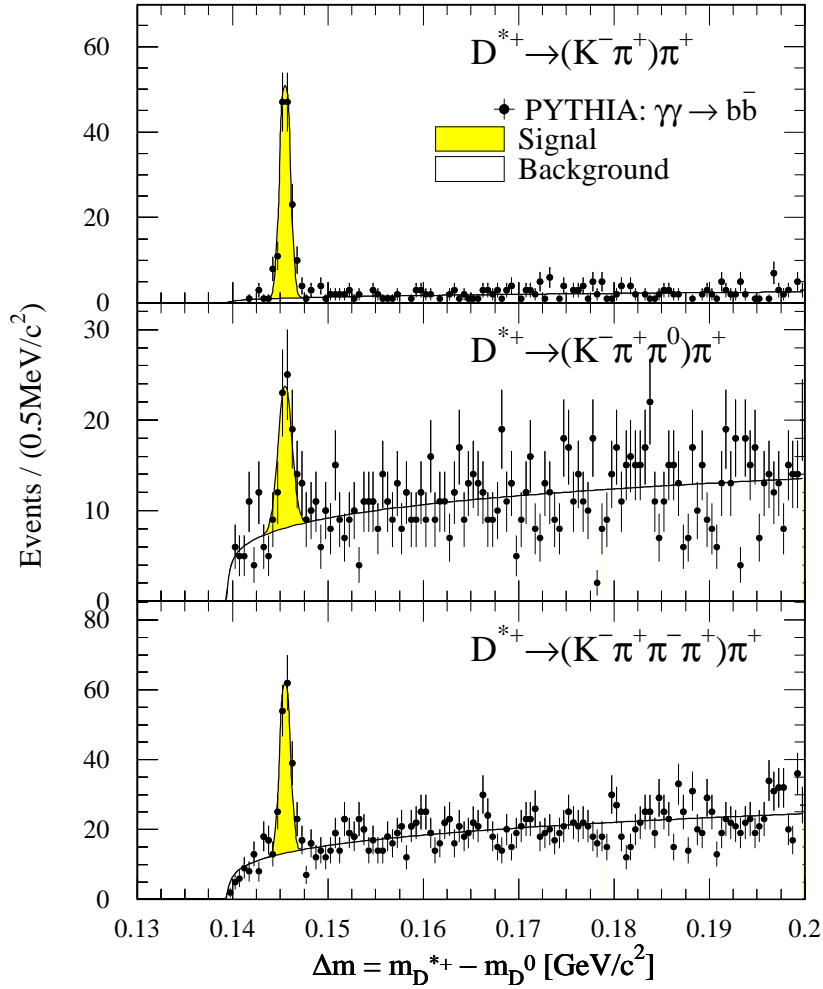

Figure 4.15: Mass difference of reconstructed D^{*+} and D^0 candidates for all considered D^0 decay modes together using $(\gamma\gamma \to b\bar{b})$ PYTHIA Monte Carlo sample. The points show data, the error bars represent statistical uncertainties, and the solid line describes the result of an unbinned likelihood fit.
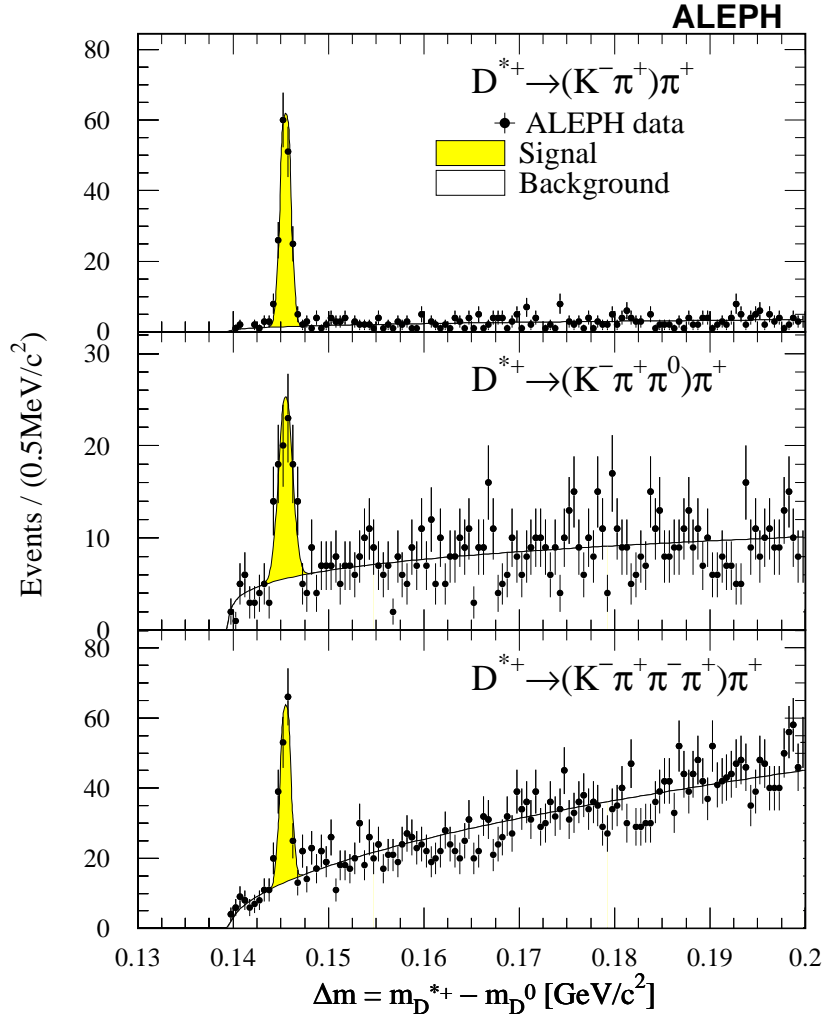
Figure 4.16: Mass difference of reconstructed D^{*+} and D^0 candidates for three considered D^0 decay modes separately. The notations are the same as in Fig. 4.14

using a Monte Carlo sub-sample of $140\,000$ $(\gamma\gamma \to b\bar{b})$ events and the total bottom cross-section $\sigma(e^+e^- \to e^+e^-b\bar{b}) = 13.1 \pm 2.0\,\text{(stat.)} \pm 2.4\,\text{(syst.)}$ as measured by the L3 collaboration [55]. This $\gamma\gamma \to b\bar{b}$ Monte Carlo sub-sample, whose luminosity is estimated to be about 15 times higher than that of the analysed data sample, is analysed in exactly the same way as the data sample. Figure 4.15 shows the Δm distribution for all the three considered decay modes together. As a result of the unbinned likelihood fit $(313 \pm 25\,\text{(stat.)})$ D^{*+} events are observed. Normalizing the luminosity of this Monte Carlo sub-sample to the luminosity of the analysed data sample, the expected number of D^{*+} events coming from b-production is determined to be $(20.5 \pm 1.6\,\text{(stat.)})$. Subtracting this background, a total number of $(339.5 \pm 27.0\,\text{(stat.)})$ D^{*+} events is found in the data sample analyzed.

Figure 4.17: Mass difference of reconstructed D^{*+} and D^0 candidates for three considered D^0 decay modes separately using $(\gamma\gamma \rightarrow b\bar{b})$ PYTHIA Monte Carlo sample.

Figure 4.16 shows the Δm distributions using selected ALEPH data for the three considered decay modes separately. A clean signal of the D^{*+} mesons is clearly observed in all three decay modes under study. Among them, the decay $D^{*+} \rightarrow (K^-\pi^+)\pi^+$, although having the smallest branching ratio, gives the best signal due to its low multiplicity. A poor efficiency of reconstructing π^0 causes the decay $D^{*+} \rightarrow (K^-\pi^+\pi^0)\pi^+$, even though being the best channel in terms of branching ratio, to contribute the least to the overall statistics. The high multiplicity results in a fast rise of the combinatorial background after the peak in decay mode $D^{*+} \rightarrow (K^-\pi^+\pi^-\pi^+)\pi^+$. The total number of D^{*+} mesons found in each considered decay mode is determined in much the same way as described above. The width σ of the

Gaussian describing the signal is fixed to $0.5\,\mathrm{MeV}/c^2$, $0.7\,\mathrm{MeV}/c^2$, and $0.5\,\mathrm{MeV}/c^2$ for decay mode (1), (2), and (3), respectively. These are determined in Monte Carlo studies for three decay modes separately. The poorer resolution for decay mode (2), $D^{*+} \rightarrow (K^-\pi^+\pi^0)\pi^+$, is a consequence of the poor resolution of the reconstructed π^0 meson. The expected $b\bar{b}$ background is again determined using the $(\gamma\gamma \rightarrow b\bar{b})$ PYTHIA Monte Carlo sub-sample (Fig. 4.17).

A total number of $(156.4 \pm 14.9\,(\mathrm{stat.}))$, $(67.4 \pm 12.3\,(\mathrm{stat.}))$ and $(128.4 \pm 16.3\,(\mathrm{stat.}))$ D^{*+} mesons is found in the decay mode (1), (2) and (3) respectively with the expected contribution from $b\bar{b}$ production having been subtracted.

4.2.3 Trigger efficiency

The ALEPH trigger was optimised for annihilation events therefore such events enjoy almost 100% trigger efficiency whereas two-photon events do not. Reasons being that two-photon events are boosted along the beam axis and have much smaller invariant masses and multiplicities in comparison to annihilation events (Sect. 4.1). More importantly the trigger was not simulated in Monte Carlo events. Thus, the efficiency at which the detector triggers two-photon events has to be determined for possible correction should it be significantly smaller than 100%.

Various components of the ALEPH detector were employed to build up a set of 32 individual triggers. Figure 4.18 shows the number of individual triggers being fired in the selected D^{*+} events in the signal region (4.5). There are six events triggered by a single trigger and one event triggered simultaneously by eleven individual triggers.

To derive the trigger efficiency in this analysis, a method proposed and developed in [56] is employed. At first efficiencies of individual triggers are determined which are then combined to estimate the overall trigger efficiency. Assuming that there are two independent triggers A and B. The efficiency $\epsilon_{A(B)}$ of trigger A with respect to trigger B is defined as the ratio of the number of events triggered by both triggers A and B, $N_{A\cap B}$, and the number of events N_B triggered by trigger B,

$$\epsilon_{A(B)} = N_{A\cap B}/N_B \quad . \tag{4.6}$$

Given a set of individual trigger efficiencies $\epsilon_A, \epsilon_B...$ the overall trigger efficiency $\epsilon_{trigger}$ is calculated as

$$\epsilon_{trigger} = 1 - (1 - \epsilon_A)(1 - \epsilon_B)... \quad . \tag{4.7}$$

In this analysis, the following four triggers are found to be fired most often in the selected D^{*+} events:

- SNG-C-EM The single charged electromagnetic energy trigger is set if there is energy deposited in the ECAL and evidence of a track in an ITC sector pointing to it.
- DBL-C-E2 The double charged electromagnetic energy trigger is the same as SNG-C-EM with evidence of at least one more track in other ITC sectors.
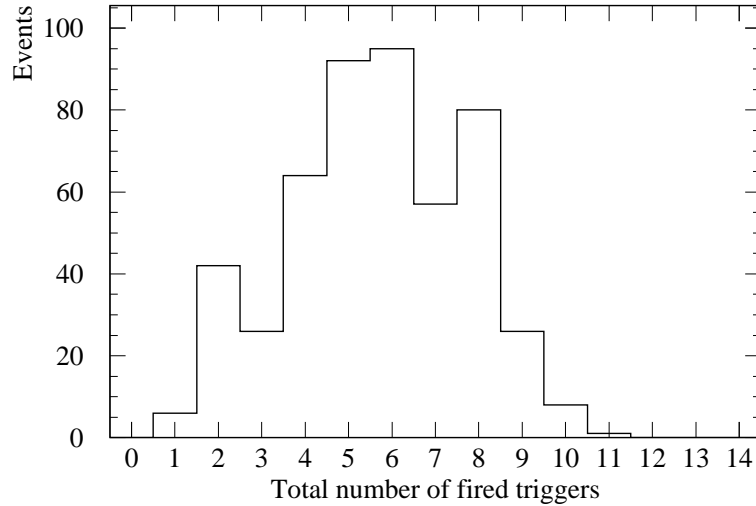
Figure 4.18: The total number of fired triggers for D^{*+} events in the signal region.

Efficiency of trigger	calculated with respect to trigger			
	SNG-N-EL	SNG-C-EM	TRK-CNT2	DBL-C-E2
SNG-N-EL	–	0.801 ± 0.084	0.673 ± 0.099	0.664 ± 0.091
SNG-C-EM	0.982 ± 0.077	–	0.822 ± 0.085	0.808 ± 0.078
TRK-CNT2	0.884 ± 0.071	0.880 ± 0.064	–	0.884 ± 0.072
DBL-C-E2	0.957 ± 0.075	0.950 ± 0.067	0.970 ± 0.066	–

Table 4.4: The efficiencies of four considered triggers calculated with respect to each other for the selected D^{*+} events in the signal region.

- SNG-N-EL The single neutral electromagnetic energy trigger is set if there is a high energy cluster in the ECAL and no evidence of a track in the ITC pointing to it.
- TRK-CNT2 This trigger requires two tracks back-to-back in the ITC.

Table 4.4 shows the efficiencies and their corresponding statistical uncertainties of these triggers calculated with respect to each other. The fact that these triggers are not truly independent of each other, since they all involve the use of the ITC, is a limiting factor. But the estimated efficiencies are still reliable should the ITC sectors have efficiencies close to 100%. That seems to be the case, if one compares the efficiency of SNG-C-EM(SNG-N-EL) to that of DBL-C-E2(SNG-N-EL). The latter requires simultaneously evidences of two tracks in two different sectors of the ITC, while the earlier needs only evidence of a track in one ITC sector and yet they have similar efficiencies. The overall trigger efficiency of the selected D^{*+} events is estimated to be consistent with 100% with a statistical uncertainty of 1%.

4.3 Relative Fractions of *Direct* and *Single Resolved* Contributions

The open charm production in $\gamma\gamma$ collisions at LEP2 energy (183–209 GeV) is dominated by contributions from *direct* and *single resolved* processes since the contribution from the double-resolved represents only a negligible margin [38], [34]. The separation into direct, single-resolved and double-resolved processes is physically meaningful only up to next-to-leading (NLO) QCD. At higher orders, all channels are mixed and the separation as such has no meaning any more. In this Section the relative fractions of direct and single-resolved contributions are determined with the help of the LO PYTHIA Monte Carlo.

4.3.1 Event Variables

In the LO QCD, the $c\bar{c}$ pair makes up the final state of the $\gamma\gamma$ system in the direct case whereas in the single resolved case the partons of the resolved photon (photon-residue) in addition to the $c\bar{c}$ pair constitute the final state (Fig. 4.19).

a) Direct process b) Single resolved process

Figure 4.19: Main contributions to charm production in $\gamma\gamma$ events

Two variables sensitive to this different behaviour have been studied. The same variables have been used in [57]:

- x_γ^{min} In the detector only the fragmentation products of the coloured partons (quarks and gluons), namely the colourless hadrons, are observed. The coloured partons themselves cannot be directly observed due to the colour confinement property in the framework of QCD. If the energy is sufficiently large, the hadrons originating from a parton are collimated into a bundle called a jet. Conclusions about the momentum and direction of the primary parton can be made should the jet be succesfully reconstructed. In this

analysis, the jets were reconstructed using the KTCLUS algorithm described in [58]. This algorithm splits the set of jets of an event into a part coming from the hard subprocess (hard jets) and a part considered as the underlying event (remnant jets) on the basis of a cut in the normalized transverse momentum of the clustered objects [59]. About $47\,\%$ of the selected D^{*+} events are found to be di-jet events. A di-jet event in this analysis is defined as an event with exactly two hard jets. For this type of event, a pair of variables x_γ^+ and x_γ^- can be defined as

$$x_\gamma^+ = \frac{\sum_{\text{jets}}(E + p_z)}{\sum_{\text{e\,flow}}(E + p_z)} \qquad \text{and} \qquad x_\gamma^- = \frac{\sum_{\text{jets}}(E - p_z)}{\sum_{\text{e\,flow}}(E - p_z)} \quad , \qquad (4.8)$$

where p_z is the momentum component along the beam axis and E is the energy of the jet or hadron. The sum in the numerators run over the two charm jets and the sums in the denominator run over all energy-flow objects found by the detector. Ideally, in the direct case both x_γ^+ and x_γ^- should be close to 1 because the total hadronic system is contained in the two charm jets. In the single resolved case at least one of the $x_\gamma^\pm$ should be significantly below 1 because in the numerators the remnant jet is not considered. Hence, the two processes should separate in

$$x_\gamma^{\text{min}} = \min(x_\gamma^+, x_\gamma^-) \quad . \qquad (4.9)$$

The validity of this assumption is clearly proven at least in the framework of the PYTHIA Monte Carlo. Figure 4.20 shows the scatter plot x_γ^+ versus x_γ^- for selected D^{*+} di-jet events in the direct and single-resolved processes simulated by PYTHIA Monte Carlo separately. The corresponding x_γ^{min} distributions are shown in Fig. 4.21. In the direct process the x_γ^{min} distribution peaks around 0.9 whereas in case of the single-resolved process it is around 0.4.

- The transverse momentum $p_{\text{t}}^{D^{*+}}$ of the D^{*+} is correlated with the invariant mass of the $c\bar{c}$ system and the total visible invariant mass W_{vis} in turn is correlated with the invariant mass of the total $\gamma\gamma$ system. So the fraction $p_{\text{t}}^{D^{*+}}/W_{\text{vis}}$ should be distributed at higher values for the direct case compared to the distribution of single resolved events as shown in Fig. 4.22. This variable is valid for all selected D^{*+} events.

4.3.2   Determination of the Main Contributions

Figures 4.24 and 4.25 show the distributions of $p_{\text{t}}^{D^{*+}}/W_{\text{vis}}$ and x_γ^{min} in data for all D^{*+} events found in the signal region (4.5) of the mass difference spectrum. The combinatorial and $b\bar{b}$ background have to be subtracted. In order to determine the combinatorial background in the signal region, the $p_{\text{t}}^{D^{*+}}/W_{\text{vis}}$ and x_γ^{min} distributions

a) Direct process

b) Single-resolved process
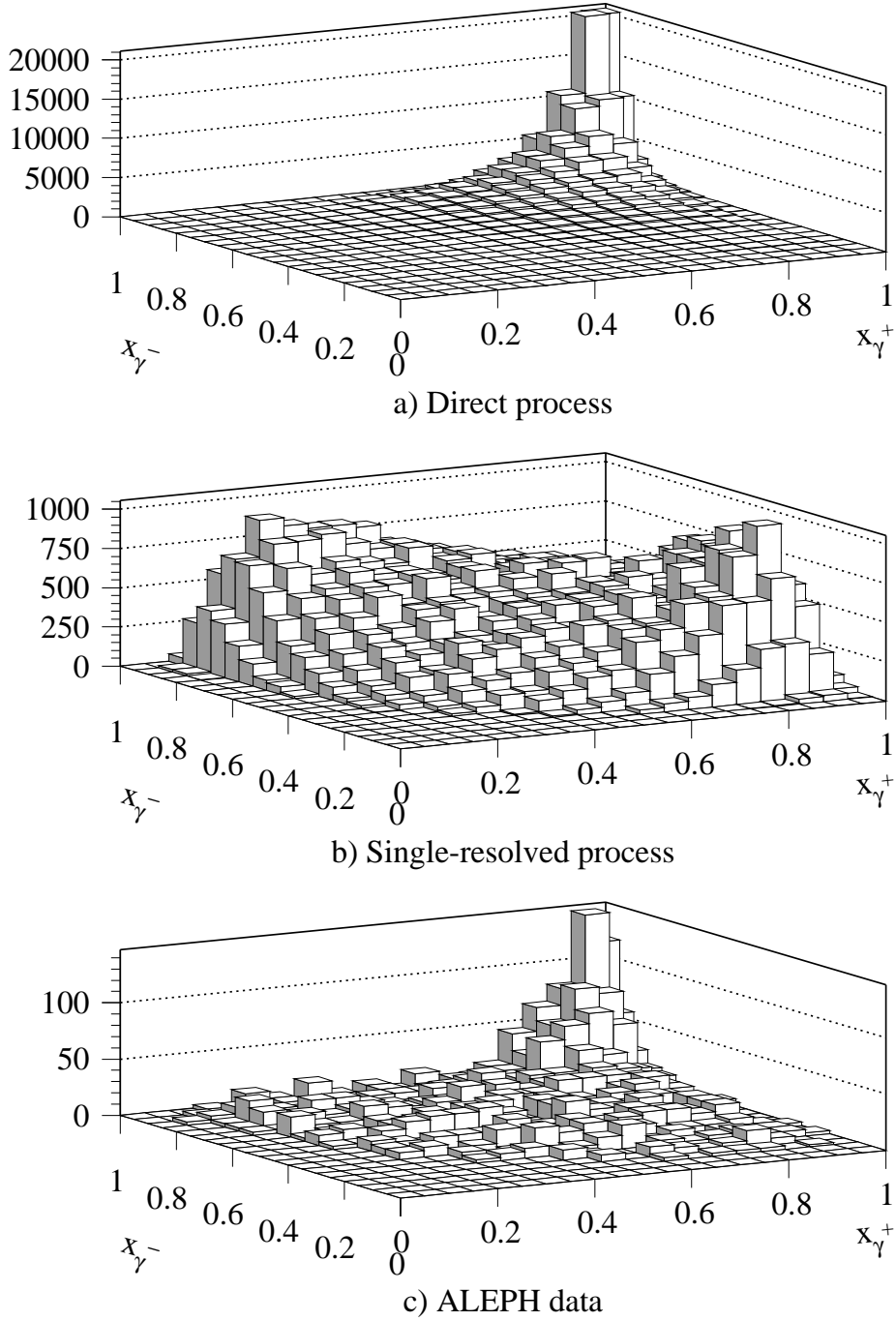
c) ALEPH data

Figure 4.20: x_γ^+ vs. x_γ^- for selected D^{*+} events in the direct and single-resolved sub-samples generated using PYTHIA Monte Carlo. Also being shown is the same distribution for selected D^{*+} events in the analysed ALEPH data.
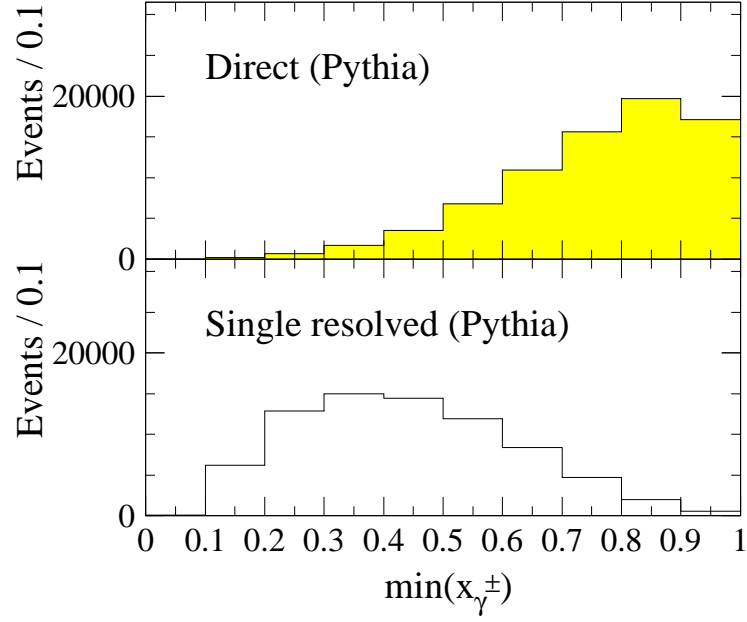
Figure 4.21: x_γ^{min} distribution for reconstructed di-jet Monte Carlo events containing a D^{*+}. The *direct* part is given by the shaded histogram, the *single resolved* one by the open histogram.
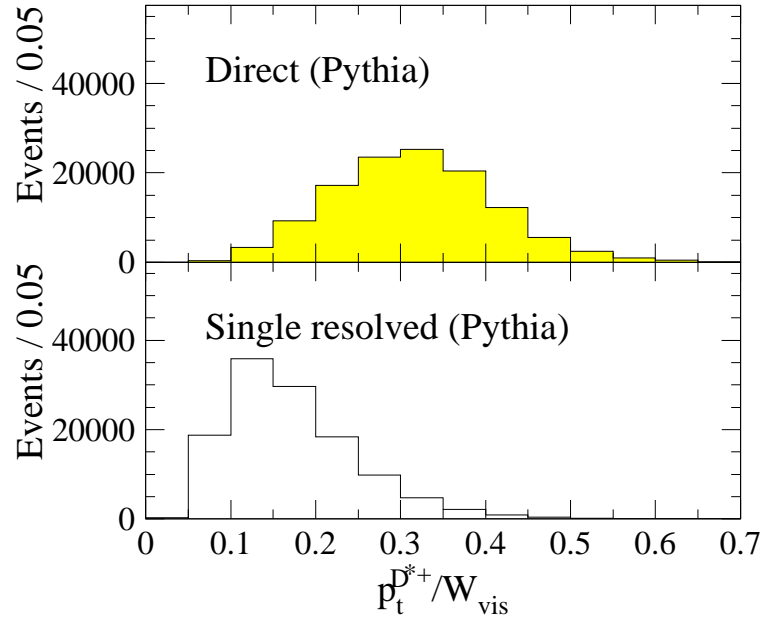
Figure 4.22: $p_t^{\mathrm{D}^{*+}}/W_{\mathrm{vis}}$ distribution for reconstructed Monte Carlo D^{*+} events. The *direct* part is given by the shaded histogram, the *single resolved* one by the open histogram.
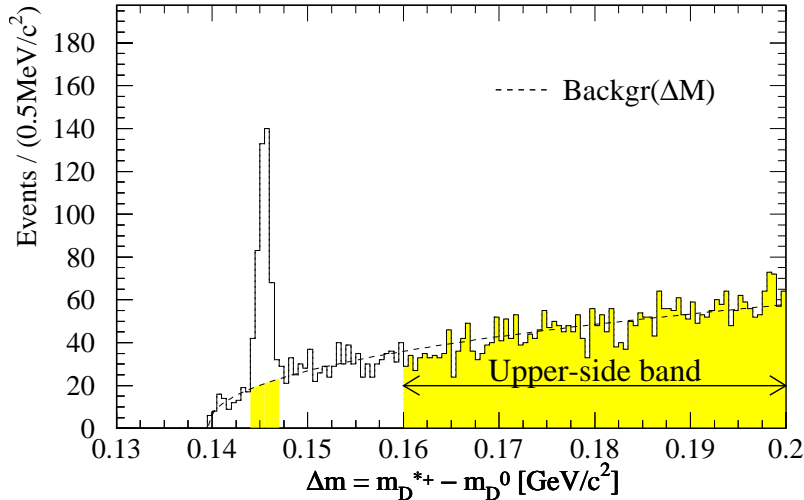
Figure 4.23: Mass difference of reconstructed D^{*+} and D^0 candidates for all considered D^0 decay modes together. The histogram shows ALEPH data. The dashed line indicates the combinatorial backgound $Backgr(\Delta m)$ as the result of the unbinned likelyhood fit. The upper-side band is indicated by the shaded area.

of the events found in the upper-side band $(0.16\,\mathrm{GeV}/c^2 < \Delta m < 0.2\,\mathrm{GeV}/c^2)$ of the mass difference spectrum (Fig. 4.23) are determined at first. These distributions are then normalized using the shape of the combinatorial background, which was determined as described in Sect. 4.2.2. Precisely, they are scaled by a factor f defined as

$$f = \frac{\int_{\mathrm{Signalregion}} Backgr(\Delta m) \cdot d(\Delta m)}{\int_{\mathrm{Upper-sideband}} Backgr(\Delta m) \cdot d(\Delta m)}$$

where $Backgr(\Delta m) = N \cdot C \cdot (\Delta m - m_{\pi^+})^P$ is the power-law function describing the combinatorial background that constitutes part of (4.4). The $b\bar{b}$ background is determined in two steps. At first, the combinatorial background in $p_{\mathrm{t}}^{\mathrm{D}^{*+}}/W_{\mathrm{vis}}$ and x_γ^{min} distributions for selected D^{*+} in the $(\gamma\gamma \to b\bar{b})$ Monte Carlo sub-sample are determined and subtracted in exactly the same way as described above. The corresponding luminosities of the obtained distributions are then normalized to the luminosity of the analysed data sample (Sect. 4.2.2) in the final step. The normalized combinatorial and $b\bar{b}$ background distributions of $p_{\mathrm{t}}^{\mathrm{D}^{*+}}/W_{\mathrm{vis}}$ and x_γ^{min} are superimposed on Fig. 4.24 and Fig. 4.25.

Figure 4.26 shows the $p_{\mathrm{t}}^{\mathrm{D}^{*+}}/W_{\mathrm{vis}}$ distribution with background subtracted. The relative fractions are then determined by fitting the sum of the direct and single resolved Monte Carlo distributions (shown in Fig. 4.22 separately) to data with the relative fraction as a free parameter of the fit. The total number of entries of this Monte Carlo sum is required to be equal to the number of entries in the

data distribution. The different efficiencies of the two samples were implicitly taken into account by using samples generated in equal amounts in the considered D^{*+} acceptance range (4.3). Hence, the determined fractions are valid for the accepted region only. The fit yields a relative fraction of the direct process of $r_{\mathrm{dir}} = (62.6 \pm 4.2)\%$ and a single resolved contribution of $r_{\mathrm{res}} = 1 - r_{\mathrm{dir}} = (37.4 \pm 4.2)\%$, accordingly. The same procedure is applied to the x_γ^{min} distribution (Fig. 4.27). The fit determines the fraction of direct (single resolved) events to be $r_{\mathrm{dir}} = (72.5 \pm 7.4)\%$ ($r_{\mathrm{res}} = (27.5 \pm 7.4)\%$). This is, within the statistical errors, consistent with the fit result in $p_{\mathrm{t}}^{D^{*+}}/W_{\mathrm{vis}}$. Since in the $p_{\mathrm{t}}^{D^{*+}}/W_{\mathrm{vis}}$ distribution all the selected D^{*+} events contributed, its fit result was taken

$$r_{\mathrm{dir}} = (62.6 \pm 4.2)\% \quad . \tag{4.10}$$

This relative fraction r_{dir} has been measured using the same method by two other LEP experiments, the DELPHI and OPAL collaborations, to be $(55. \pm 11.)\%$ [60] and $(51. \pm 10.)\%$ [57], respectively. Within the given uncertainties, these are consistent with the result of this analysis (4.10).

The theoretical value of r_{dir} calculated in [34] for the acceptance range (4.3) is

$$r_{\mathrm{dir}} = 70.4 \, {}^{+4.6}_{-7.2} \, \% \qquad (\text{NLO QCD, Frixione et al. [34] }) \tag{4.11}$$

Even being somewhat larger, but this is still in agreement with this analysis despite the fact that the definition of the measured r_{dir} and the predicted r_{dir} are slightly different. In this analysis the definition of r_{dir} is based on the variables x_γ^{min} and $p_{\mathrm{t}}^{D^{*+}}/W_{\mathrm{vis}}$ in the LO QCD scenario and the measurement is carried out with the help of LO PYTHIA Monte Carlo. While in the case of the theoretical prediction it is based on Feynman diagram considerations at the NLO. Although meaningless at higher orders, this comparison is physically sensible when theoretical predictions are accurate to NLO as in the present case.

Having measured the relative fractions of the direct and single-resolved contributions in data, several characteristic distributions of the selected data events containing D^{*+} mesons are compared to those of Monte Carlo events. The combinatorial and $b\bar{b}$ background is subtracted from the data as described in Sect. 4.3.2. The contributions from direct and single-resolved processes in the Monte Carlo are added up according to their measured relative fractions (4.10). The total number of entries of this Monte Carlo sum is then normalized to the number of entries in the data distribution. The distributions of the visible invariant mass W_{vis}, total visible energy E_{vis}, total energy of charged particles E_{ch}, visible transverse momentum $p_{\mathrm{t,vis}}$, and charged multiplicity N_{ch} are shown in Fig. 4.28, 4.29, 4.30, 4.31 and 4.32, respectively. These are in fact the event variables used to select two-photon events (Sect. 4.1). The overall agreement between data and Monte Carlo is satisfactory taking into account the low statistics of data. The number of jets found in data events is well simulated by Monte Carlo (Fig. 4.33).
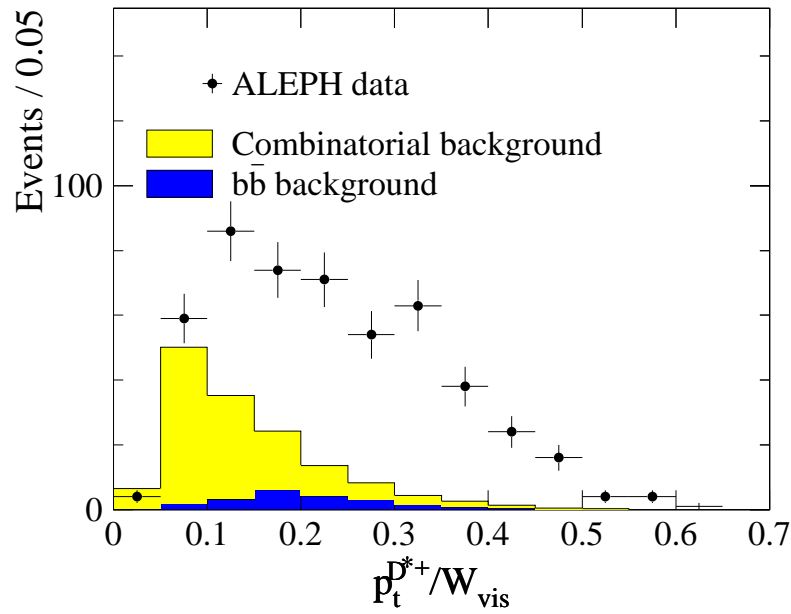
Figure 4.24: $p_t^{D^{*+}}/W_{vis}$ distribution for reconstructed D^{*+} events. The crosses show data. The combinatorial and expected $b\bar{b}$ background are also indicated.
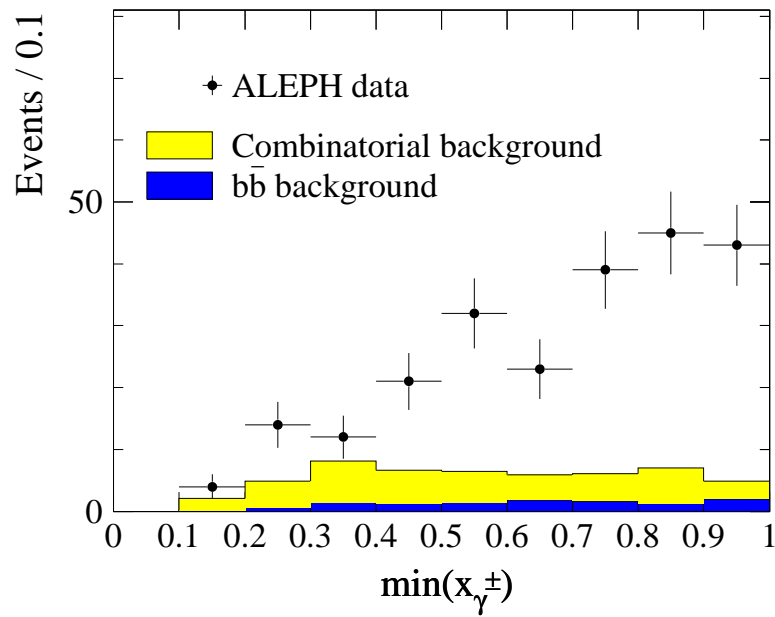
Figure 4.25: x_γ^{min} distribution for reconstructed di-jet events containing a D^{*+}. The crosses show data. Contributions of the combinatorial and $b\bar{b}$ background are represented by shaded histograms.
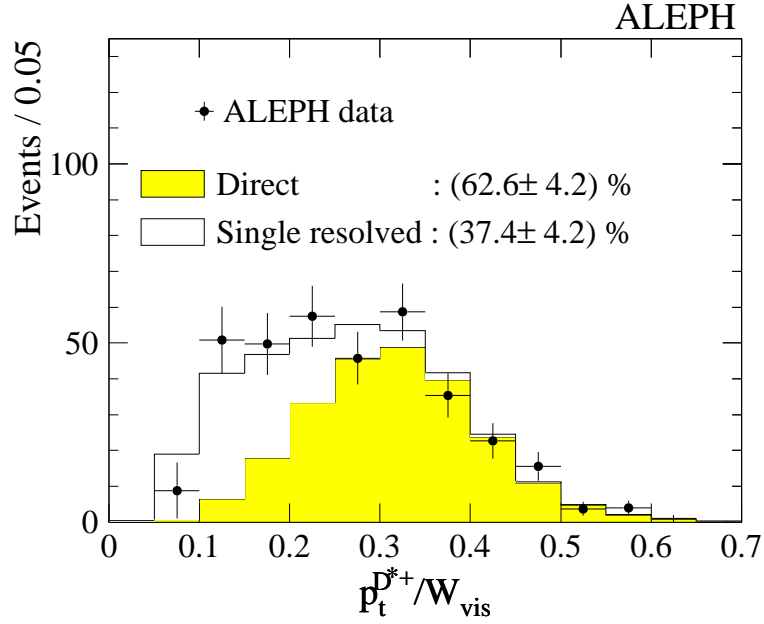
Figure 4.26: $p_t^{D^{*+}}/W_{vis}$ distribution, background has been subtracted, for reconstructed D^{*+} events. The crosses show data. Contributions of the two MC samples considered are fitted to data with the relative fraction as a fit parameter. The *direct* part is given by the shaded histogram, the *single resolved* one by the open histogram.

Figure 4.27: x_γ^{min} distribution, background has been subtracted, for reconstructed di-jet events containing a D^{*+}. The crosses show data. Contributions of the two MC samples considered are fitted to data with the relative fraction as a fit parameter. The *direct* part is given by the shaded histogram, the *single resolved* one by the open histogram.

Figure 4.28: The visible invariant mass of the selected data events containing D^{*+} mesons in the signal region (4.3) in comparison to that of PYTHIA Monte Carlo events. The points with error bars show ALEPH data, background has been subtracted. The contributions from direct, shaded histogram, and single-resolved, open histogram, processes in Monte Carlo are shown according to their relative fractions determined in Sect. 4.3.2.
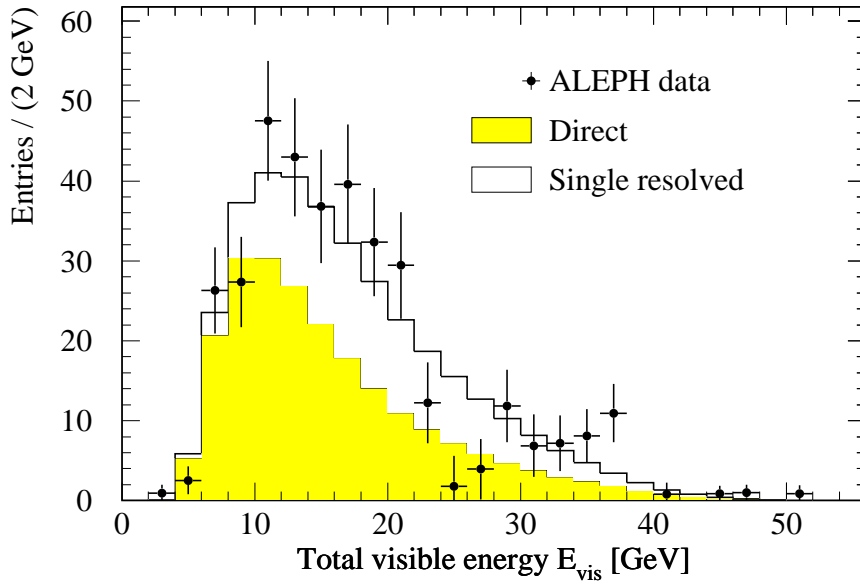
Figure 4.29: The visible energy of the selected data events containing D^{*+} mesons in the signal region (4.3) in comparison to that of PYTHIA Monte Carlo events. The notations are as the same as in Fig. 4.28.
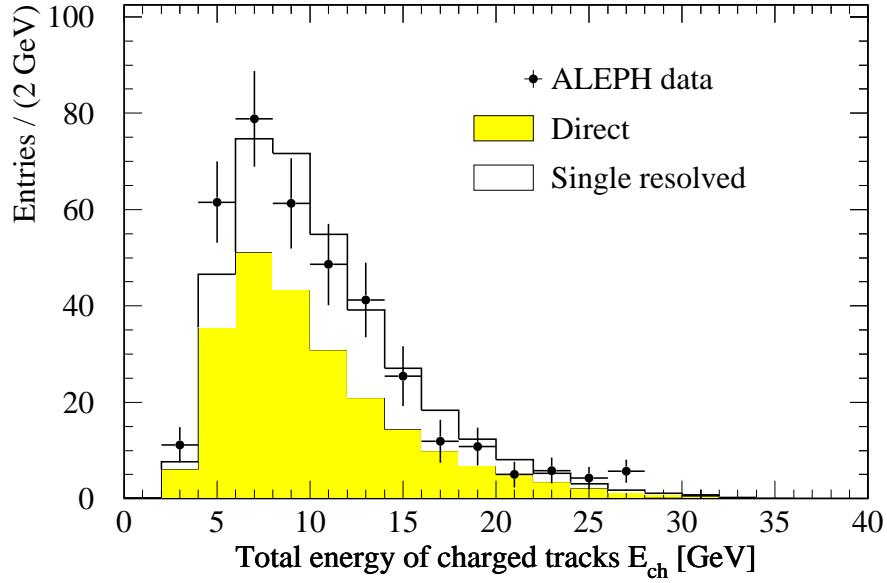
Figure 4.30: The total energy of charged particles in the selected data events containing D^{*+} mesons in the signal region (4.3) in comparison to that of PYTHIA Monte Carlo events. The notations are the same as in Fig. 4.28.
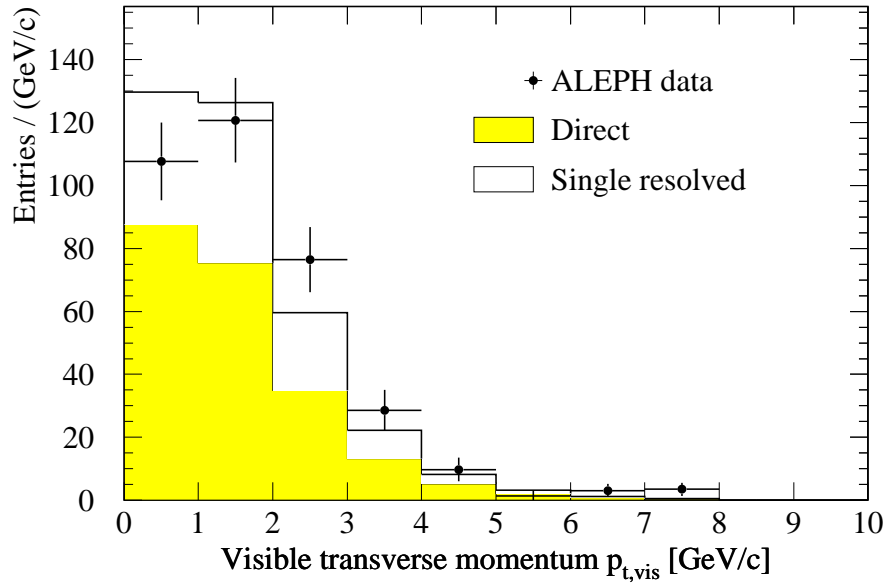
Figure 4.31: The visible transverse momentum of the selected data events containing D^{*+} mesons in the signal region (4.3) in comparison to that of PYTHIA Monte Carlo events. The notations are the same as in Fig. 4.28.
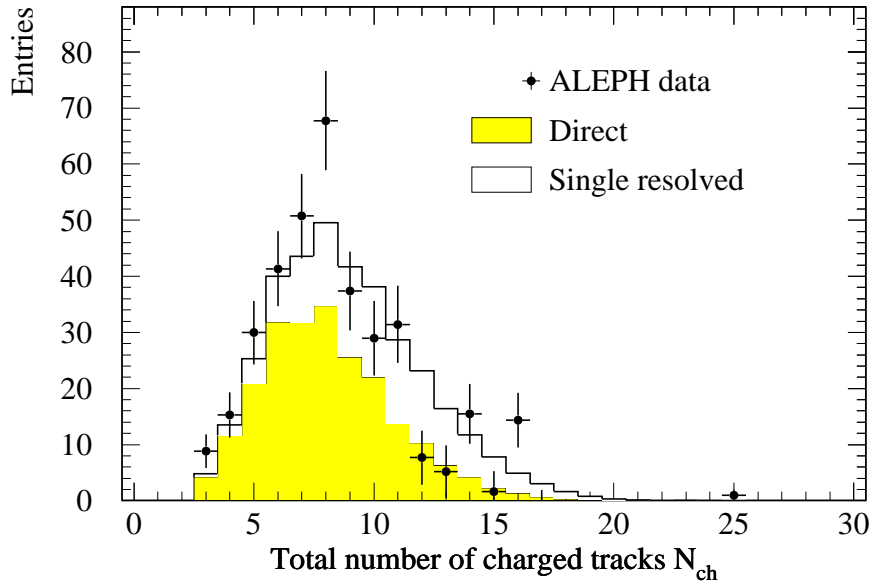
Figure 4.32: The total number of charged particles of the selected data events containing D^{*+} mesons in the signal region (4.3) in comparison to that of PYTHIA Monte Carlo events. The notations are the same as in Fig. 4.28.
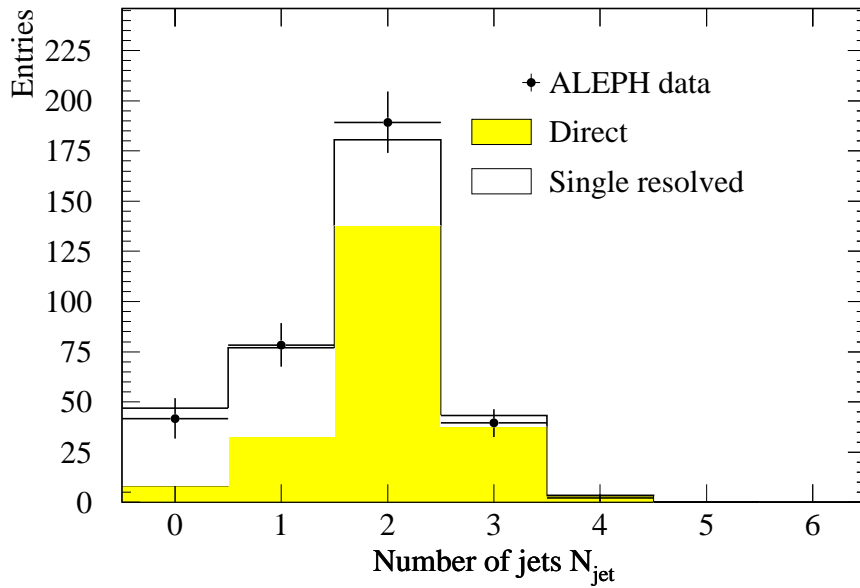
Figure 4.33: The number of hard jets found in the selected data events containing D^{*+} mesons in the signal region (4.3) in comparison to that of PYTHIA Monte Carlo events. The notations are the same as in Fig. 4.28.

4.4 Differential Cross Sections

The transverse momentum $p_{\mathrm{t}}^{\mathrm{D}^{*+}}$ and pseudorapidity $\eta^{\mathrm{D}^{*+}}$ distributions of the D^{*+} mesons give more insight into the production mechanism of the D^{*+} mesons and therefore more comprehensive tests of the theory at the parton level than the total cross-section alone. In this analysis the differential cross-section of the D^{*+} mesons is measured with respect to the transverse momentum $p_{\mathrm{t}}^{\mathrm{D}^{*+}}$, $\mathrm{d}\sigma/\mathrm{d}p_{\mathrm{t}}^{\mathrm{D}^{*+}}$, and pseudorapidity $\eta^{\mathrm{D}^{*+}}$, $\mathrm{d}\sigma/\mathrm{d}|\eta^{\mathrm{D}^{*+}}|$, of the D^{*+} mesons in the acceptance range (4.3). The results are then compared to NLO QCD calculations as well as to similar measurements from other LEP experiments.

4.4.1 Measurements

The differential cross-section $\mathrm{d}\sigma/\mathrm{d}p_{\mathrm{t}}^{\mathrm{D}^{*+}}$ is measured in three $p_{\mathrm{t}}^{\mathrm{D}^{*+}}$ bins: [2–3, 3–5, 5–12] GeV/c, while $\mathrm{d}\sigma/\mathrm{d}|\eta^{\mathrm{D}^{*+}}|$ is measured in three $|\eta^{\mathrm{D}^{*+}}|$ bins: [0–0.5, 0.5–1.0, 1.0–1.5] (Fig. 4.34). All considered decay modes are treated separately. The average differential cross section $\mathrm{d}\sigma/\mathrm{d}p_{\mathrm{t}}^{\mathrm{D}^{*+}}$ for a given $p_{\mathrm{t}}^{\mathrm{D}^{*+}}$ bin is obtained by

$$\frac{\mathrm{d}\sigma}{\mathrm{d}p_{\mathrm{t}}^{\mathrm{D}^*}} = \frac{N_{\mathrm{found}}^{\mathrm{D}^{*+}}}{\Delta p_{\mathrm{t}}^{\mathrm{D}^{*+}} \cdot \mathcal{L} \cdot B_* \cdot B_0 \cdot \epsilon_{p_{\mathrm{t}}^{\mathrm{D}^{*+}}}} \qquad , \qquad (|\eta^{\mathrm{D}^{*+}}| < 1.5) \quad . \qquad (4.12)$$

Analogously one obtains $\mathrm{d}\sigma/\mathrm{d}|\eta^{\mathrm{D}^{*+}}|$ for a given bin in $|\eta^{\mathrm{D}^{*+}}|$

$$\frac{\mathrm{d}\sigma}{\mathrm{d}|\eta^{\mathrm{D}^*}|} = \frac{N_{\mathrm{found}}^{\mathrm{D}^{*+}}}{\Delta|\eta^{\mathrm{D}^{*+}}| \cdot \mathcal{L} \cdot B_* \cdot B_0 \cdot \epsilon_{|\eta^{\mathrm{D}^{*+}}|}} \qquad , \qquad (2\,\mathrm{GeV}/c < p_{\mathrm{t}}^{\mathrm{D}^{*+}} < 12\,\mathrm{GeV}/c) \quad ,$$

where

- $N_{\mathrm{found}}^{\mathrm{D}^{*+}}$ is the number of D^{*+} found in the considered bin with $\mathrm{b}\bar{\mathrm{b}}$ background having been subtracted,
- $\Delta p_{\mathrm{t}}^{\mathrm{D}^{*+}}$, $\Delta|\eta^{\mathrm{D}^{*+}}|$ are the considered intervals in $p_{\mathrm{t}}^{\mathrm{D}^{*+}}$ and $|\eta^{\mathrm{D}^{*+}}|$,
- $\mathcal{L} = 699\,\mathrm{pb}^{-1}$ is the integrated luminosity of the data analyzed,
- B_* is the branching ratio $\mathrm{BR}(\mathrm{D}^{*+} \to \mathrm{D}^0\pi^+) = (68.3 \pm 1.4)\%$ [40],
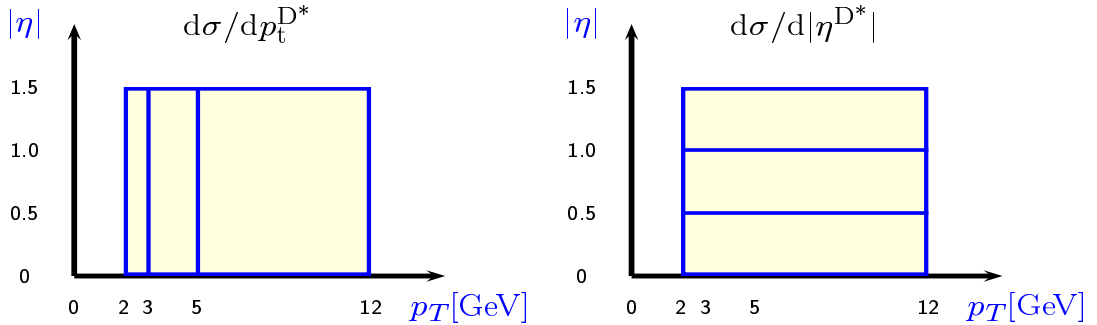
Figure 4.34: The considered intervals in $p_{\mathrm{t}}^{\mathrm{D}^{*+}}$ and $\eta^{\mathrm{D}^{*+}}$.

- B_0 is the branching ratio of the considered D^0 decay mode [40],
- $\epsilon_{p_t^{D*+}}$ ($\epsilon_{|\eta^{D*+}|}$) is the efficiency of reconstructing a D^{*+} candidate in the given p_t^{D*+} ($|\eta^{D*+}|$) bin for the considered decay mode. Since efficiencies are determined separately for direct and single resolved processes ($\epsilon_{p_t^{D*+}}^{\text{dir}}$ and $\epsilon_{p_t^{D*+}}^{\text{res}}$ respectively) the total efficiency is a weighted combination using the fractions as determined in Sect. 4.3,

$$\epsilon_{p_t^{D*+}} = r_{\text{dir}} \cdot \epsilon_{p_t^{D*+}}^{\text{dir}} + r_{\text{res}} \cdot \epsilon_{p_t^{D*+}}^{\text{res}} \qquad \text{and} \qquad \epsilon_{|\eta^{D*+}|} = r_{\text{dir}} \cdot \epsilon_{|\eta^{D*+}|}^{\text{dir}} + r_{\text{res}} \cdot \epsilon_{|\eta^{D*+}|}^{\text{res}} \quad .$$

The number of D^{*+} mesons in each considered bin and mode is determined as described in Sect. 4.2.2. Figures 4.35 and 4.36 show the Δm distributions in all considered p_t^{D*+} and η^{D*+} bins for the three decay modes under study, respectively. The results of the unbinned likelihood fits are superimposed onto these distributions. The number of D^{*+} mesons observed, $N_{\text{observed}}^{D^{*+}}$, as the result of the fit is listed in Table 4.5 and Table 4.7. The shapes of the Δm distributions in η^{D*+} bins are very similar for the same decay mode as they should be. Combinatorial background for the low p_t^{D*+} range, $2\,\text{GeV}/c < p_t^{D*+} < 3\,\text{GeV}/c$, is significant in the decay modes $D^{*+} \rightarrow (K^-\pi^+\pi^0)\pi^+$ and $D^{*+} \rightarrow (K^-\pi^+\pi^-\pi^+)\pi^+$, as expected. Also listed in Tables 4.5 and 4.7 are the expected numbers of D^{*+} mesons, $N_{\text{expected}}^{D^{*+}}$, coming from $b\bar{b}$ background together with their estimated uncertainties. These uncertainties are determined by combining the uncertainties of the total cross section $\sigma(e^+e^- \rightarrow e^+e^-b\bar{b})$ [55] and the statistical uncertainties of $N_{\text{expected}}^{D^{*+}}$.

The efficiency of reconstructing a D^{*+} meson is calculated using the PYTHIA Monte Carlo simulation in all considered p_t^{D*+} and η^{D*+} bins for the considered decay modes. The efficiencies $\epsilon_{p_t^{D*+}}^{\text{dir}}$ and $\epsilon_{p_t^{D*+}}^{\text{res}}$ are shown in Fig. 4.37. In general the efficiency increases as p_t^{D*+} increases, since the higher the p_t^{D*+} the better the decay products of the D^{*+} are measured. Figure 4.38 shows the efficiencies $\epsilon_{|\eta^{D*+}|}^{\text{dir}}$ and $\epsilon_{|\eta^{D*+}|}^{\text{res}}$ for the three considered decay modes. In the high $|\eta^{D*+}|$ range, $1.0 < |\eta^{D*+}| < 1.5$, the efficiency drops significantly. This follows from the poor acceptance of the detector in the forward direction. A slightly better efficiency of the direct process in comparison to that of the single-resolved process is observed in all considered bins and modes. That is due to the fact that single-resolved events are more likely to be produced in the problematic forward direction.

Tables 4.5 and 4.7 show the number of D^{*+} mesons found, $N_{\text{found}}^{D^{*+}}$, in the chosen p_t^{D*+} and $|\eta^{D*+}|$ bins with the $b\bar{b}$-background having been subtracted, as well as the derived differential cross sections $d\sigma/dp_t^{D*}$ and $d\sigma/d|\eta^{D*}|$ with their statistical and systematic errors (in that order). The systematic errors are discussed in the next section. The resulting cross sections for the different D^{*+} decay modes are consistent with each other for all bins in p_t^{D*+} as well as in $|\eta^{D*+}|$, taking into account the statistical uncertainties. The weighted average over all of the considered D^{*+} decay modes is given in Tables 4.6 and 4.8 for each p_t^{D*+} and $|\eta^{D*+}|$ bin, where only the dominating statistical uncertainties were used for weighting.
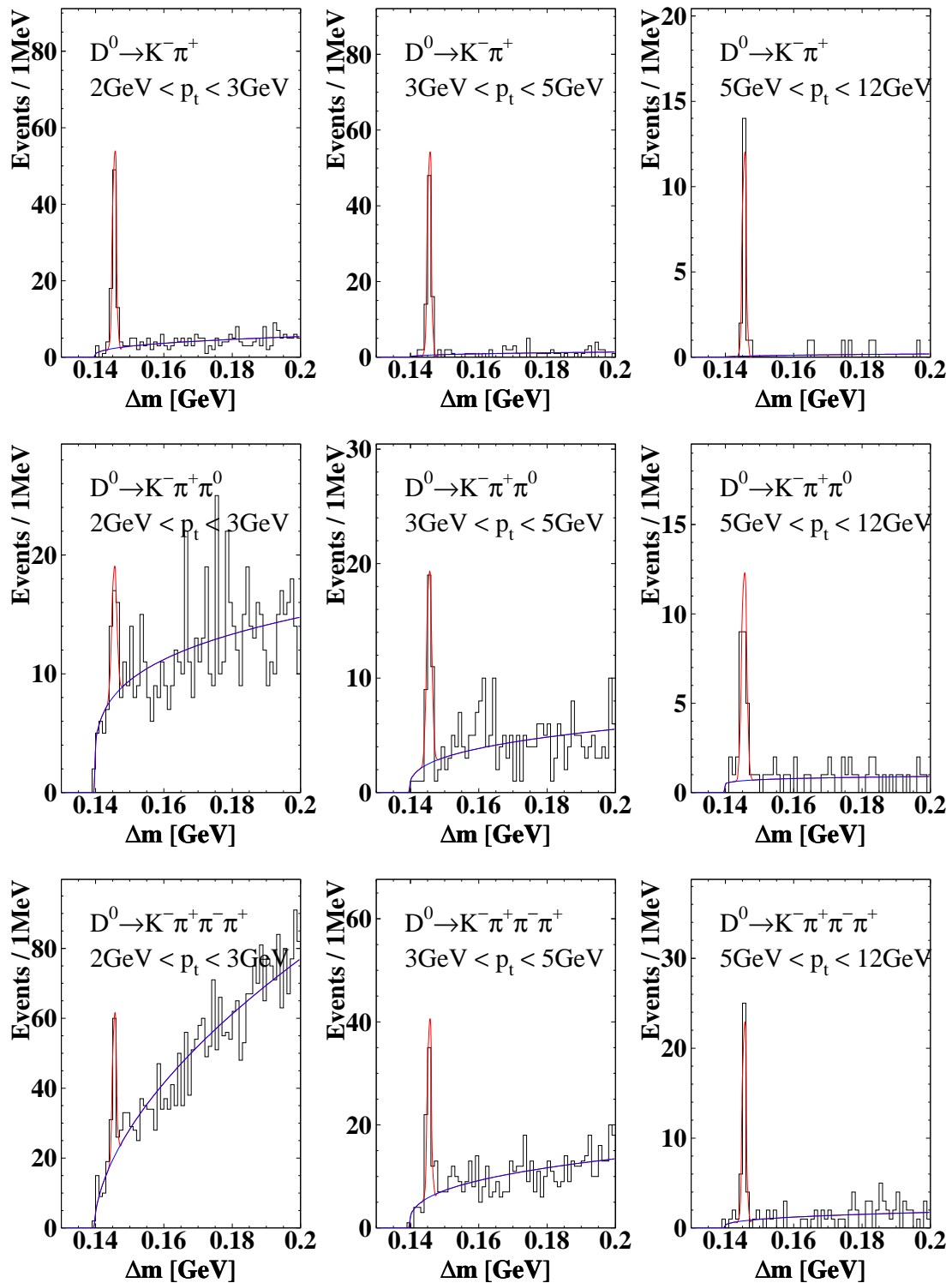
Figure 4.35: The mass difference Δm distributions for considered $p_t^{\mathrm{D}^{*+}}$ bins and decay modes. The histograms show ALEPH data and the solid lines describe the results of the unbinned likelihood fits.
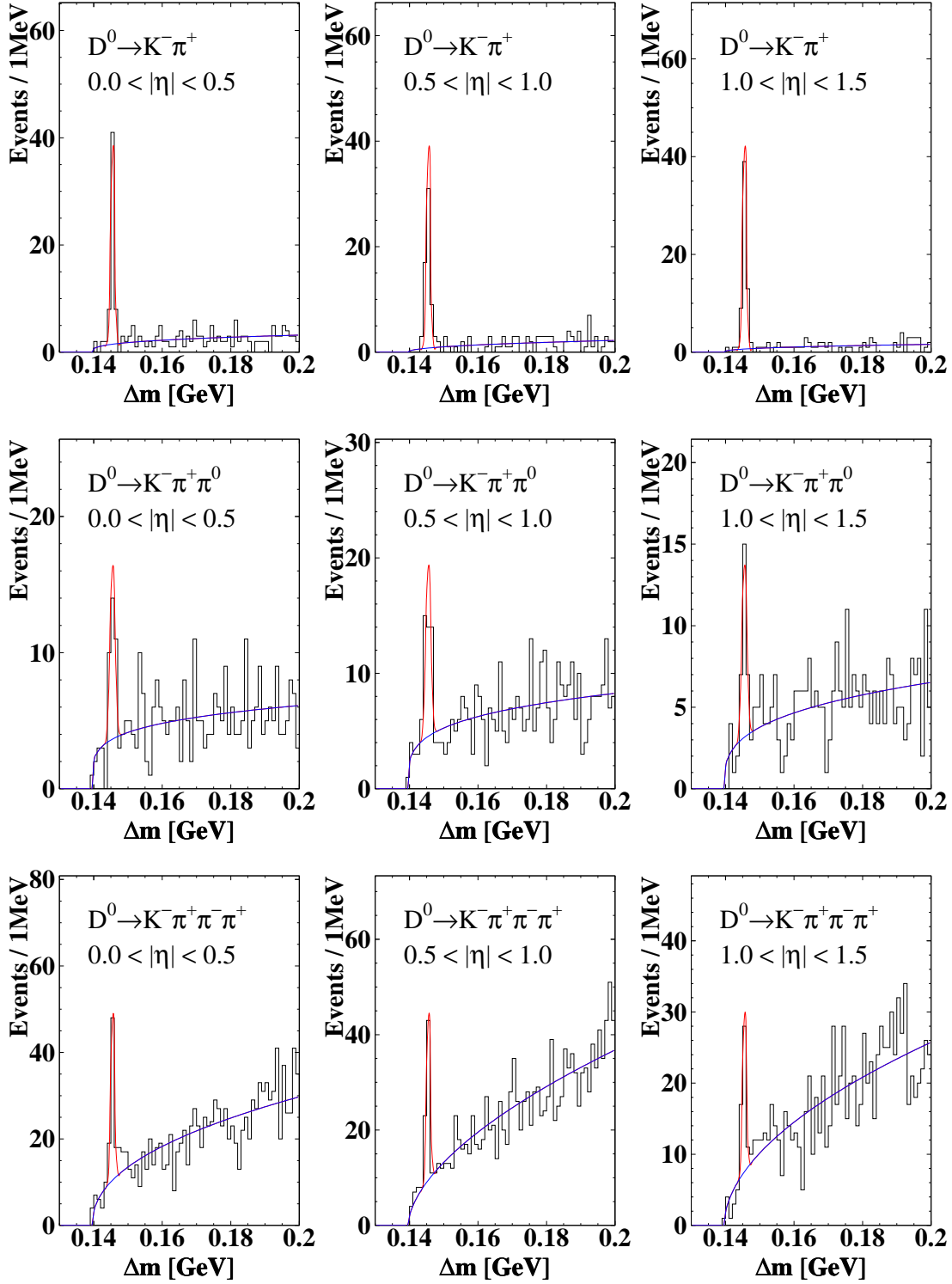
Figure 4.36: The mass difference Δm distributions for considered $|\eta^{D^{*+}}|$ bins and decay modes. The histograms show ALEPH data and the solid lines describe the results of the unbinned likelihood fits.
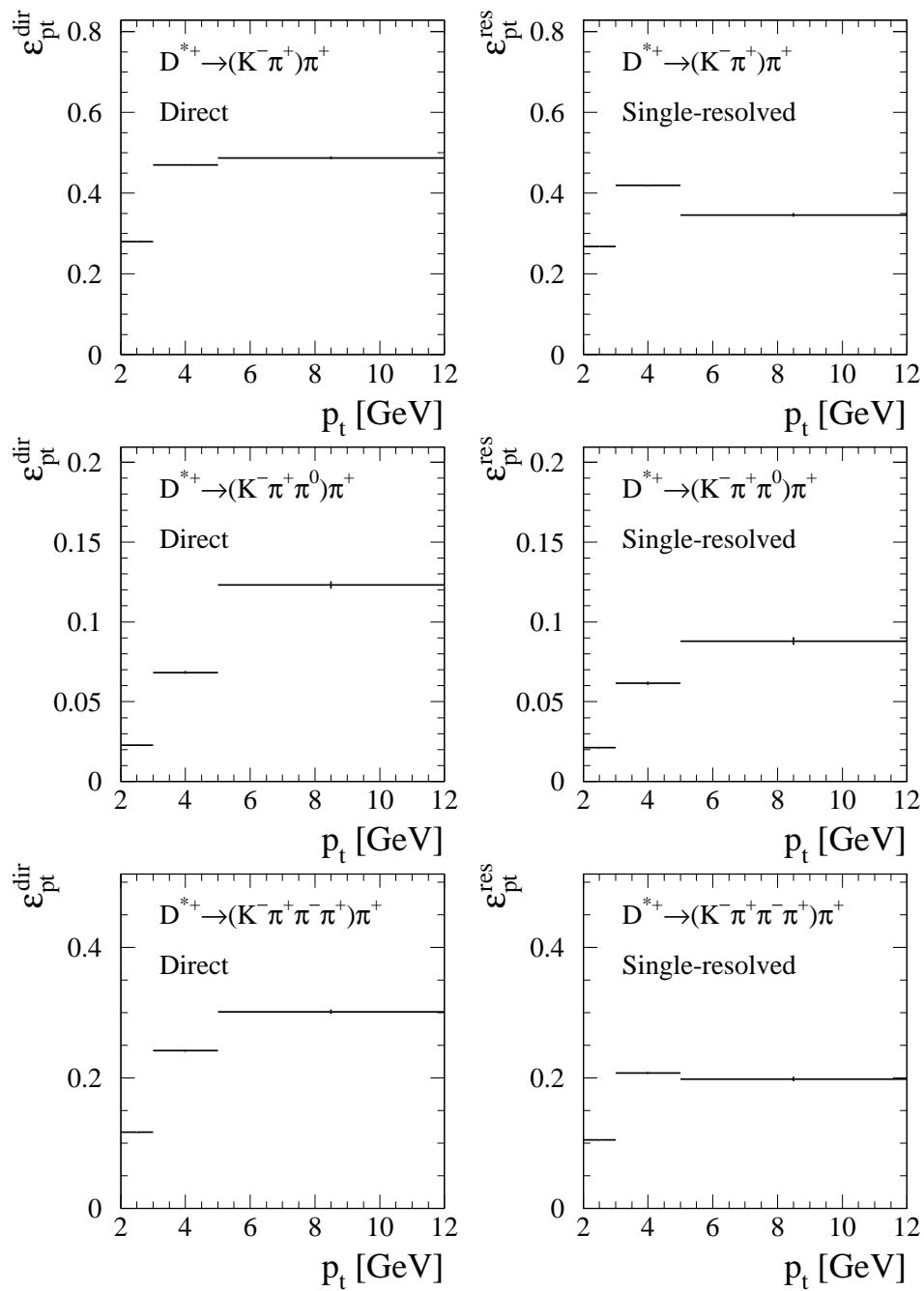
Figure 4.37: Efficiencies of reconstructing a D^{*+} meson determined by the PYTHIA Monte Carlo in the considered $p_t^{D^{*+}}$ bins for the three decay modes under study.
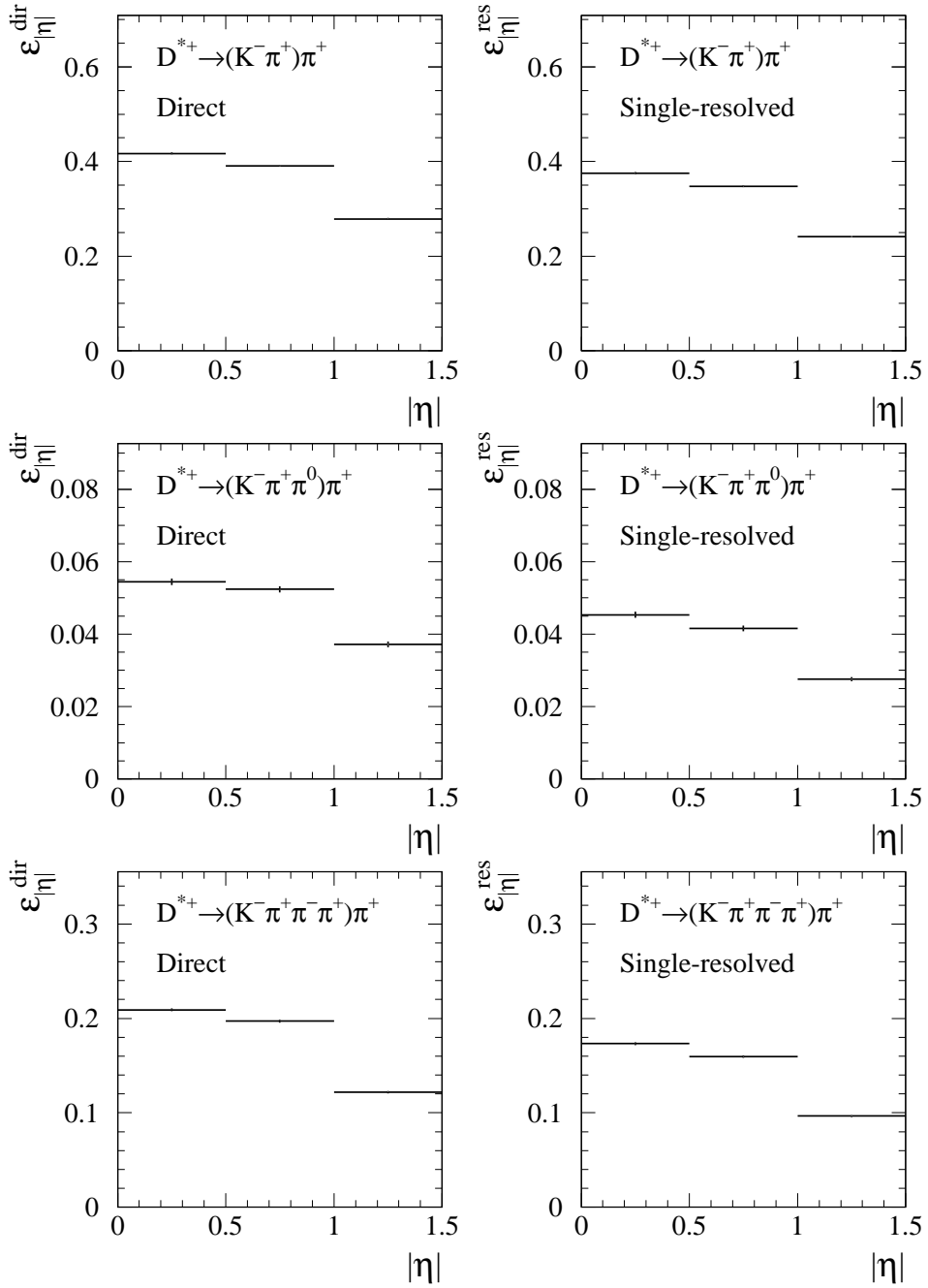
Figure 4.38: Efficiencies of reconstructing a D^{*+} meson determined by the PYTHIA Monte Carlo in the considered $|\eta^{D^{*+}}|$ bins for the three decay modes under study.

$p_t^{D^{*+}}$ range [GeV/c]	$N_{\text{observed}}^{D^{*+}}$ as the result of the unbinned likelihood fit		
	$D^{*+} \to (K^-\pi^+)\pi^+$	$D^{*+} \to (K^-\pi^+\pi^0)\pi^+$	$D^{*+} \to (K^-\pi^+\pi^-\pi^+)\pi^+$
2–3	73.0 ± 10.7	19.9 ± 6.2	57.6 ± 10.2
3–5	76.0 ± 8.1	31.0 ± 7.8	48.9 ± 9.7
5–12	16.9 ± 3.0	21.5 ± 5.7	31.3 ± 6.8
	$N_{\text{expected}}^{D^{*+}}$ from b$\bar{\text{b}}$ background		
	$D^{*+} \to (K^-\pi^+)\pi^+$	$D^{*+} \to (K^-\pi^+\pi^0)\pi^+$	$D^{*+} \to (K^-\pi^+\pi^-\pi^+)\pi^+$
2–3	3.2 ± 0.9	1.2 ± 0.5	3.1 ± 0.9
3–5	3.8 ± 1.0	2.0 ± 0.7	4.0 ± 1.1
5–12	1.8 ± 0.5	0.6 ± 0.3	2.1 ± 0.7
	$N_{\text{found}}^{D^{*+}}$ after subtracting b$\bar{\text{b}}$ background		
	$D^{*+} \to (K^-\pi^+)\pi^+$	$D^{*+} \to (K^-\pi^+\pi^0)\pi^+$	$D^{*+} \to (K^-\pi^+\pi^-\pi^+)\pi^+$
2–3	69.8 ± 10.7	18.7 ± 6.2	54.5 ± 10.3
3–5	72.2 ± 8.1	29.0 ± 7.8	44.9 ± 9.7
5–12	15.1 ± 3.0	20.9 ± 5.7	29.2 ± 6.8

	Efficiency for direct process $\epsilon_{p_t^{D^{*+}}}^{\text{dir}}$ (%)		
	$D^{*+} \to (K^-\pi^+)\pi^+$	$D^{*+} \to (K^-\pi^+\pi^0)\pi^+$	$D^{*+} \to (K^-\pi^+\pi^-\pi^+)\pi^+$
2–3	27.96 ± 0.13	2.27 ± 0.04	11.66 ± 0.09
3–5	46.94 ± 0.20	6.83 ± 0.10	24.16 ± 0.17
5–12	48.73 ± 0.34	12.32 ± 0.23	30.13 ± 0.33

	Efficiency for single resolved process $\epsilon_{p_t^{D^{*+}}}^{\text{res}}$ (%)		
	$D^{*+} \to (K^-\pi^+)\pi^+$	$D^{*+} \to (K^-\pi^+\pi^0)\pi^+$	$D^{*+} \to (K^-\pi^+\pi^-\pi^+)\pi^+$
2–3	26.81 ± 0.12	2.12 ± 0.04	10.49 ± 0.09
3–5	41.95 ± 0.21	6.17 ± 0.10	20.78 ± 0.18
5–12	34.59 ± 0.41	8.8 ± 0.24	19.83 ± 0.36

	$d\sigma/dp_t^{D^{*+}}$ (pb/GeV/c)		
	$D^{*+} \to (K^-\pi^+)\pi^+$	$D^{*+} \to (K^-\pi^+\pi^0)\pi^+$	$D^{*+} \to (K^-\pi^+\pi^-\pi^+)\pi^+$
2–3	$13.80 \pm 2.12 \pm 1.04$	$12.70 \pm 4.21 \pm 1.20$	$13.38 \pm 2.51 \pm 0.89$
3–5	$4.36 \pm 0.49 \pm 0.22$	$3.32 \pm 0.90 \pm 0.27$	$2.70 \pm 0.58 \pm 0.17$
5–12	$0.27 \pm 0.05 \pm 0.01$	$0.41 \pm 0.11 \pm 0.03$	$0.44 \pm 0.10 \pm 0.03$

Table 4.5: The number of D^{*+} mesons found with $|\eta^{D^{*+}}| < 1.5$ in bins of $p_t^{D^{*+}}$ for the three decay modes after subtracting b$\bar{\text{b}}$ background. The efficiency is listed separately for direct and single resolved processes. The cross section $d\sigma/dp_t^{D^{*+}}$ measured in each decay mode is given together with statistical and systematic errors.

	$p_t^{D^{*+}}$ range [GeV/c]		
	2–3	3–5	5–12
$d\sigma/dp_t^{D^{*+}}$ [pb/GeV/c]	$13.50 \pm 1.51 \pm 1.03$	$3.61 \pm 0.34 \pm 0.21$	$0.32 \pm 0.04 \pm 0.02$

Table 4.6: The combined differential cross section $d\sigma/dp_t^{D^{*+}}$ together with statistical and systematic errors (in that order).

$|\eta^{D^{*+}}|$ range	$N_{\text{observed}}^{D^{*+}}$ as the result of the unbinned likelihood fit		
	$D^{*+} \to (K^-\pi^+)\pi^+$	$D^{*+} \to (K^-\pi^+\pi^0)\pi^+$	$D^{*+} \to (K^-\pi^+\pi^-\pi^+)\pi^+$
0.0–0.5	52.5 ± 8.9	23.6 ± 6.8	54.3 ± 10.0
0.5–1.0	54.2 ± 8.2	27.3 ± 7.6	49.2 ± 9.5
1.0–1.5	58.8 ± 7.9	19.5 ± 6.3	31.5 ± 7.6
	$N_{\text{expected}}^{D^{*+}}$ from bb background		
	$D^{*+} \to (K^-\pi^+)\pi^+$	$D^{*+} \to (K^-\pi^+\pi^0)\pi^+$	$D^{*+} \to (K^-\pi^+\pi^-\pi^+)\pi^+$
0.0–0.5	3.3 ± 0.9	1.8 ± 0.6	3.2 ± 1.0
0.5–1.0	3.4 ± 0.9	0.9 ± 0.4	3.4 ± 1.0
1.0–1.5	2.3 ± 0.7	1.0 ± 0.4	2.2 ± 0.7
	$N_{\text{found}}^{D^{*+}}$ after subtracting bb background		
	$D^{*+} \to (K^-\pi^+)\pi^+$	$D^{*+} \to (K^-\pi^+\pi^0)\pi^+$	$D^{*+} \to (K^-\pi^+\pi^-\pi^+)\pi^+$
0.0–0.5	49.2 ± 8.9	21.8 ± 6.8	51.1 ± 10.0
0.5–1.0	50.8 ± 8.3	26.4 ± 7.6	45.8 ± 9.5
1.0–1.5	56.4 ± 7.9	18.5 ± 6.3	29.3 ± 7.6

	Efficiency for direct process $\epsilon_{|\eta^{D^{*+}}|}^{\text{dir}}$ (%)		
	$D^{*+} \to (K^-\pi^+)\pi^+$	$D^{*+} \to (K^-\pi^+\pi^0)\pi^+$	$D^{*+} \to (K^-\pi^+\pi^-\pi^+)\pi^+$
0.0–0.5	41.71 ± 0.19	5.45 ± 0.09	20.90 ± 0.16
0.5–1.0	39.07 ± 0.19	5.24 ± 0.08	19.70 ± 0.16
1.0–1.5	27.88 ± 0.17	3.72 ± 0.07	12.19 ± 0.13

	Efficiency for single resolved process $\epsilon_{|\eta^{D^{*+}}|}^{\text{res}}$ (%)		
	$D^{*+} \to (K^-\pi^+)\pi^+$	$D^{*+} \to (K^-\pi^+\pi^0)\pi^+$	$D^{*+} \to (K^-\pi^+\pi^-\pi^+)\pi^+$
0.0–0.5	37.55 ± 0.20	4.53 ± 0.08	17.31 ± 0.16
0.5–1.0	34.74 ± 0.19	4.16 ± 0.08	15.95 ± 0.15
1.0–1.5	24.08 ± 0.16	2.75 ± 0.06	9.66 ± 0.11

	$d\sigma/d|\eta^{D^*}|$ [pb]		
	$D^{*+} \to (K^-\pi^+)\pi^+$	$D^{*+} \to (K^-\pi^+\pi^0)\pi^+$	$D^{*+} \to (K^-\pi^+\pi^-\pi^+)\pi^+$
0.0–0.5	$13.33 \pm 2.40 \pm 0.85$	$12.86 \pm 4.02 \pm 1.10$	$14.40 \pm 2.80 \pm 1.00$
0.5–1.0	$14.78 \pm 2.40 \pm 0.86$	$16.48 \pm 4.75 \pm 1.36$	$13.81 \pm 2.87 \pm 0.91$
1.0–1.5	$23.22 \pm 3.24 \pm 2.10$	$16.59 \pm 5.63 \pm 1.73$	$14.35 \pm 3.70 \pm 1.31$

Table 4.7: The number of D^{*+} mesons found in $|\eta^{D^{*+}}|$ bins for the three decay modes after subtracting background. The efficiency is listed separately for direct and single resolved processes. The cross section $d\sigma/d|\eta^{D^{*+}}|$ measured in each considered decay mode is given together with statistical and systematic errors.

	$|\eta^{D^{*+}}|$ range		
	0.0–0.5	0.5–1.0	1.0–1.5
$d\sigma/d|\eta^{D^{*+}}|$ [pb]	$13.62 \pm 1.65 \pm 0.94$	$14.65 \pm 1.71 \pm 0.94$	$18.93 \pm 2.23 \pm 1.75$

Table 4.8: The combined differential cross sections, $d\sigma/d|\eta^{D^{*+}}|$ together with statistical and systematic errors (in that order).

4.4.2 Systematic Errors of Differential Cross Sections

The study on systematic errors was performed separately for each $p_t^{D^{*+}}$ and $|\eta^{D^{*+}}|$ bin and for each of the considered D^{*+} decay modes, unless otherwise specified.

The systematic error introduced by the event selection was estimated by varying the cuts within the resolution obtained from the Monte Carlo detector simulation. The systematic uncertainty was estimated by the resulting relative variation of the efficiency. This yields an uncertainty of 0.6%–6.4%, depending on the considered $p_t^{D^{*+}}$ or $|\eta^{D^{*+}}|$ bin and on the D^{*+} decay mode.

The selection of pion and kaon candidates depends essentially on the dE/dx measurement as well as on the expectation values $dE/dx_{exp,h}$ used to calculate the probability for a given mass hypothesis m_h in (4.1) and (4.2). In the present analysis the expectation values entering the estimator χ_h in (4.1) are taken from a recalibration of the dE/dx expectation performed for the preselected data sample [61]. The analysis was repeated with the general dE/dx calibration used in ALEPH. The deviations in the cross sections, 0.5%–5.7%, are used as an estimate of the systematic error due to the uncertainty of the dE/dx calibration.

The systematic error due to the acceptance mass range used to classify D^0 candidates was examined by comparison of the mass distributions of D^0 candidates which contributed to the D^{*+} signal in data and Monte Carlo for each D^0 decay mode separately. A Gaussian fit was applied to these distributions. The fraction of the fitted Gaussian which lies within the acceptance mass range differs between data and Monte Carlo by less than 0.6%. Thus, no uncertainty due to this source is taken into account.

In order to estimate the error introduced by the method for extracting the number of D^{*+} events as described in Sect. 4.2.2 the mean of the fitted Gaussian (4.4) were varied by $\pm 0.05\,\text{MeV}/c^2$, and the width were varied by 10% about its values as obtained in Monte Carlo. This yields a relative error on the efficiencies of 0.8%–2.1%.

A variation of the interval that defines the upper side band yields a variation in the r_{dir} below 0.05%. Hence, this source is neglected. The present analysis assumes the fraction r_{dir} to be constant over the considered kinematic range. Monte Carlo studies showed a variation of the fraction in this range up to 12%, depending on the bin in $p_t^{D^{*+}}$ and $|\eta^{D^{*+}}|$. A relative uncertainty of 10% is therefore added in quadrature to the statistical uncertainty of r_{dir}. A variation of $r_{dir/res}$ within these uncertainties yields a variation in the cross section of 0.3%–3.4% which is used to estimate the introduced uncertainty.

The statistical error of $b\bar{b}$ background subtraction and the uncertainties of the total cross section $\sigma(e^+e^- \rightarrow e^+e^-b\bar{b})$ yield a systematic error of 1.2%–3.4% on the differential cross sections.

The overall trigger efficiency of the selected D^{*+} events is determined to be consistent with 100% (Sect. 4.2.3). Thus no correction is made for this source.

The relative errors on the branching ratios given in [40] are used to estimate

Source	Estimated uncertainty
Event selection	$(0.6\text{–}6.4)\%$
K/π selection	$(0.5\text{–}5.7)\%$
Accepted mass range for D^0	$< 0.16\%$, neglected
D^{*+} selection	$(0.8\text{–}2.1)\%$
D^{*+} from annihilation events	$< 1\%$, neglected
b$\bar{\text{b}}$ background subtraction	$(1.2\text{–}3.4)\%$
Fraction of direct/resolved $r_{\text{dir}}/r_{\text{res}}$	$(0.3\text{–}3.4)\%$
BR(D$^{*+} \to$ D$^0\pi^+$)	2.0%
BR(D$^0 \to$ K$^-\pi^+$)	2.3%
BR(D$^0 \to$ K$^-\pi^+\pi^0$)	6.5%
BR(D$^0 \to$ K$^-\pi^+\pi^-\pi^+$)	5.3%
statistical limitation in Monte Carlo	$(0.5\text{–}2.3)\%$

Table 4.9: Sources of systematic uncertainty on the differential cross sections.

the corresponding relative systematic uncertainties in the cross sections.

Similarly the relative uncertainties in the efficiencies due to finite statistics in the Monte Carlo samples, $(0.5\text{–}2.3)\%$, are taken into account.

All systematic errors are assumed to be uncorrelated and therefore added in quadrature. Table 4.9 shows a summary of systematic studies.

4.4.3 Comparison to Theory and other LEP Experiments

The charmed quark mass, $m_\text{c} \gg \Lambda_{\text{QCD}}$, makes the perturbative QCD calculations reliable, by cutting off collinear singularities and by setting a large scale at which the strong coupling constant α_s can be evaluated and found to be small enough. The differential cross sections $\mathrm{d}\sigma/\mathrm{d}p_\text{t}^{\text{D}^{*+}}$ and $\mathrm{d}\sigma/\mathrm{d}|\eta^{\text{D}^{*+}}|$ were calculated up to next-to-leading order (NLO) accuracy using two different approaches, the fixed-order (FO) [34] and the resummed (RES) [35] NLO QCD. In the FO approach (also known as massive approach), only light quarks ($q = u, d$, and s) are present as the active flavours in the photons. The charm quark is assumed to be massive and produced dynamically in the hard subprocess. The FO NLO QCD calculation is expected to be reliable in the region where the transverse momentum $p_\text{t}(\text{c})$ of the charm quark is comparable to the charm quark mass m_c. In the high $p_\text{t}(\text{c})$ range, terms containing $\log\left(p_\text{t}(\text{c})/m_\text{c}\right)$ become too large and may spoil the convergence of the perturbation series [34]. In such a case, the RES NLO QCD calculation exists as an alternative approach which allows the resummation of the dominant $\log\left(p_\text{t}(\text{c})/m_\text{c}\right)$ terms to all orders. In this approach, the charm quark is also assumed to be present as a massless active flavour inside the photon. All the mass singularity terms, occurring as powers of $\log\left(p_\text{t}(\text{c})/m_\text{c}\right)$, are absorbed into the parton distribution function (PDF) of the photon and the fragmentation

function describing the transition $c \rightarrow D^{*+}$ [35]. This approach is also known as massless approach, in the sense that it does not include the contributions that are suppressed by powers of $m_c/p_t(c)$ into the cross section. More details about these two NLO QCD approaches can be found in [34–37].

Figures 4.39 and 4.40 show the measured $d\sigma/dp_t^{D^{*+}}$ and $d\sigma/d|\eta^{D^{*+}}|$ in comparison to the NLO perturbative QCD calculations, the FO NLO and the RES NLO. In both cases, the charm quark mass m_c is set to $1.5\,\mathrm{GeV}$, the renormalization scale μ_R and the factorization scale μ_F are chosen such that $\mu_F^2 = 4 \cdot \mu_R^2 = m_T^2 \equiv m_c^2 + p_t(c)^2$, where $p_t(c)$ is the transverse momentum of the charm quark. For the resolved contribution the photonic parton densities of the GRS-HO parametrization is chosen [17] in the FO NLO calculation, whereas the RES NLO uses GRV-HO [10]. The fragmentation of the charm quark to the D^{*+} is modelled by the fragmentation function suggested by Peterson et al. [39], with $\epsilon_c = 0.035$ in case of FO NLO. The RES NLO calculation uses $\epsilon_c = 0.185$, which was determined by using nonperturbative fragmentation functions fitted [35] to ALEPH measurement on the inclusive D^{*+} production in e^+e^- annihilation [62]. The results of the two NLO QCD calculations are represented by the dashed lines (for RES NLO) and dot-dashed lines (for FO NLO) in both Fig. 4.39 and Fig. 4.40. In order to estimate the theoretical uncertainties, the FO NLO calculation was repeated with the charm mass and the renormalization scale varied as described in the figures. The RES NLO calculation is also repeated using the AFG [19] as an alternative for the parton density function and varying the renormalization and factorization scales. The resulting theoretical uncertainties are indicated by the bands around the corresponding default values in Fig. 4.39 and Fig. 4.40.

Altogether, the measurement of $d\sigma/dp_t^{D^{*+}}$ seems to favour a harder $p_t^{D^{*+}}$ spectrum than predicted. The RES NLO calculation clearly overestimates the measurement in the low $p_t^{D^{*+}}$ region, while the FO NLO calculation slightly underestimates it in the $p_t^{D^{*+}} > 3.0\,\mathrm{GeV}/c$ region. The measured $d\sigma/d|\eta^{D^{*+}}|$ is consistent with the almost flat distribution predicted by both NLO calculations. But the measurement of $d\sigma/d|\eta^{D^{*+}}|$ is again overestimated by the RES NLO calculation and somewhat underestimated by the FO NLO calculation.

All three other LEP experiments DELPHI [60], L3 [65], and OPAL [57] have also measured these distributions. Figure 4.41 shows the results of their $d\sigma/dp_t^{D^{*+}}$ measurements in comparison to that of this analysis. Also shown in Fig. 4.41 are the NLO perturbative QCD calculations described above. The overall agreement between the LEP experiments is satisfactory, although there is some scatter in the low $p_t^{D^{*+}}$ region. The measurement of OPAL is reproduced very well by the RES NLO calculation, while FO NLO gives a reasonable description of L3 result. As far as the shape is concerned, the result of this analysis has the hardest $p_t^{D^{*+}}$ spectrum.

Figure 4.42 shows the $d\sigma/d|\eta^{D^{*+}}|$ distribution, where only the results of ALEPH and OPAL are included. The other two experiments measured $d\sigma/d|\eta^{D^{*+}}|$ in different acceptance ranges and binnings. The result of OPAL is again in good agreement with the RES NLO calculation.
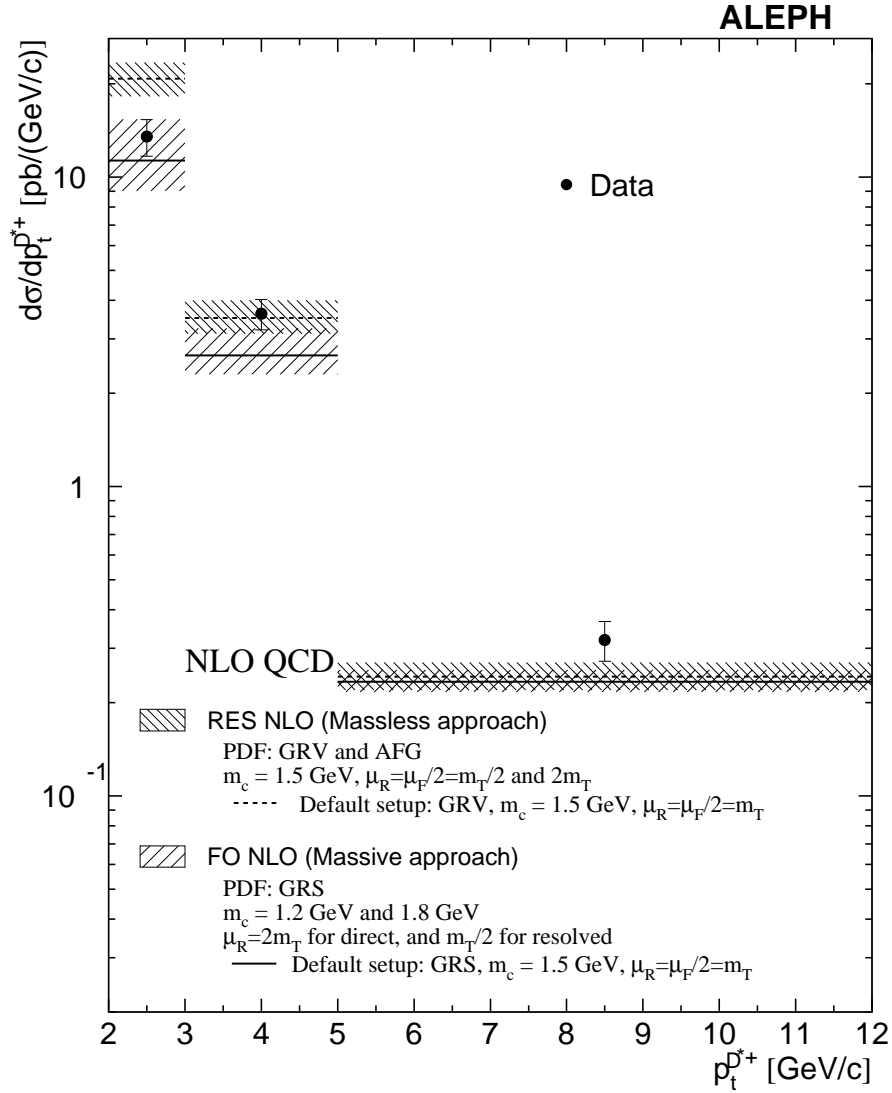
Figure 4.39: Differential cross section $\mathrm{d}\sigma/\mathrm{d}p_{\mathrm{t}}^{\mathrm{D}^{*+}}$ for the inclusive D^{*+} production. The points show the combined differential cross sections from all three decay modes under study. The vertical bars correspond to the quadratic sum of statistical and systematic uncertainties. The data are compared to the fixed-order (FO) NLO [34] and the resummed (RES) NLO [35] calculations shown as the solid and dashed lines respectively. The shaded bands represent the theoretical uncertainties of these calculations.
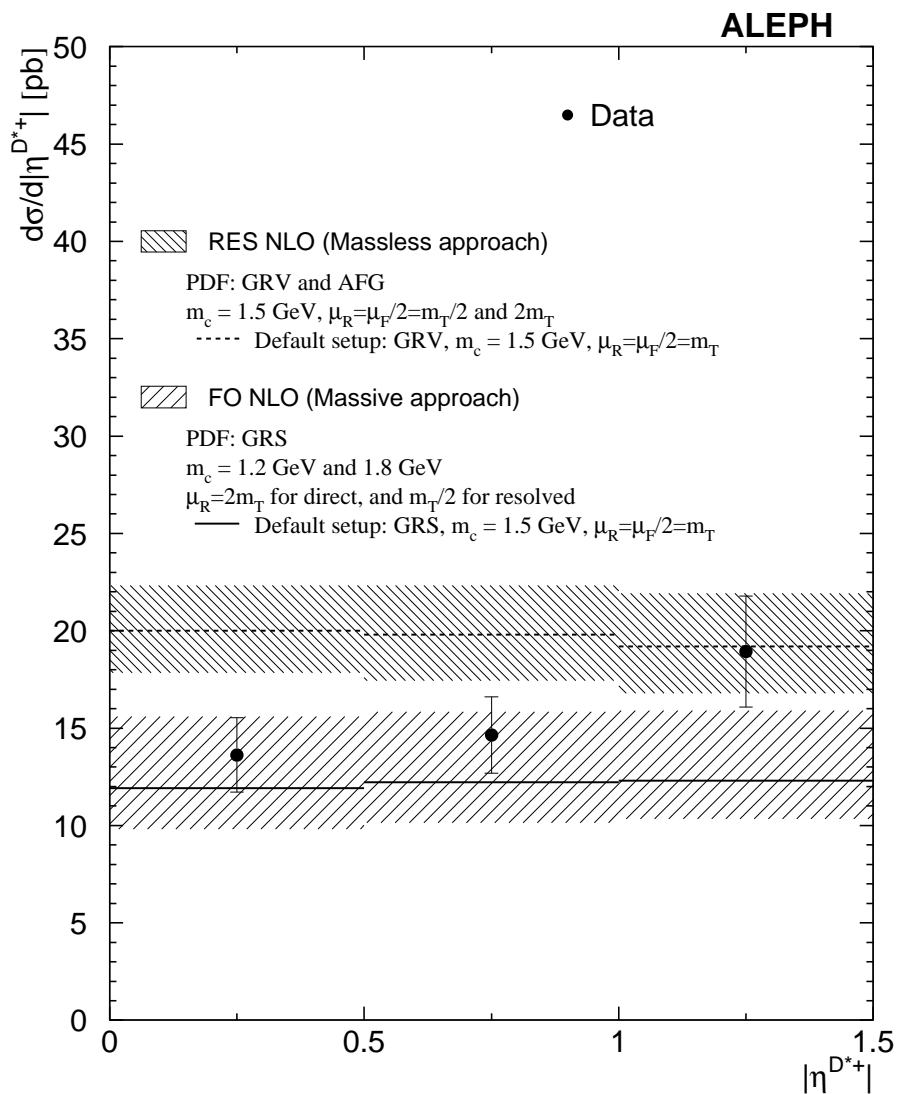
Figure 4.40: Differential cross section $d\sigma/d|\eta^{D^{*+}}|$ for the inclusive D^{*+} production. The points show the combined differential cross sections from all three decay modes under study. The vertical bars correspond to the quadratic sum of statistical and systematic uncertainties. The data are compared to the fixed-order (FO) NLO [34] and the resummed (RES) NLO [35] calculations shown as the solid and dashed lines respectively. The shaded bands represent the theoretical uncertainties of these calculations.
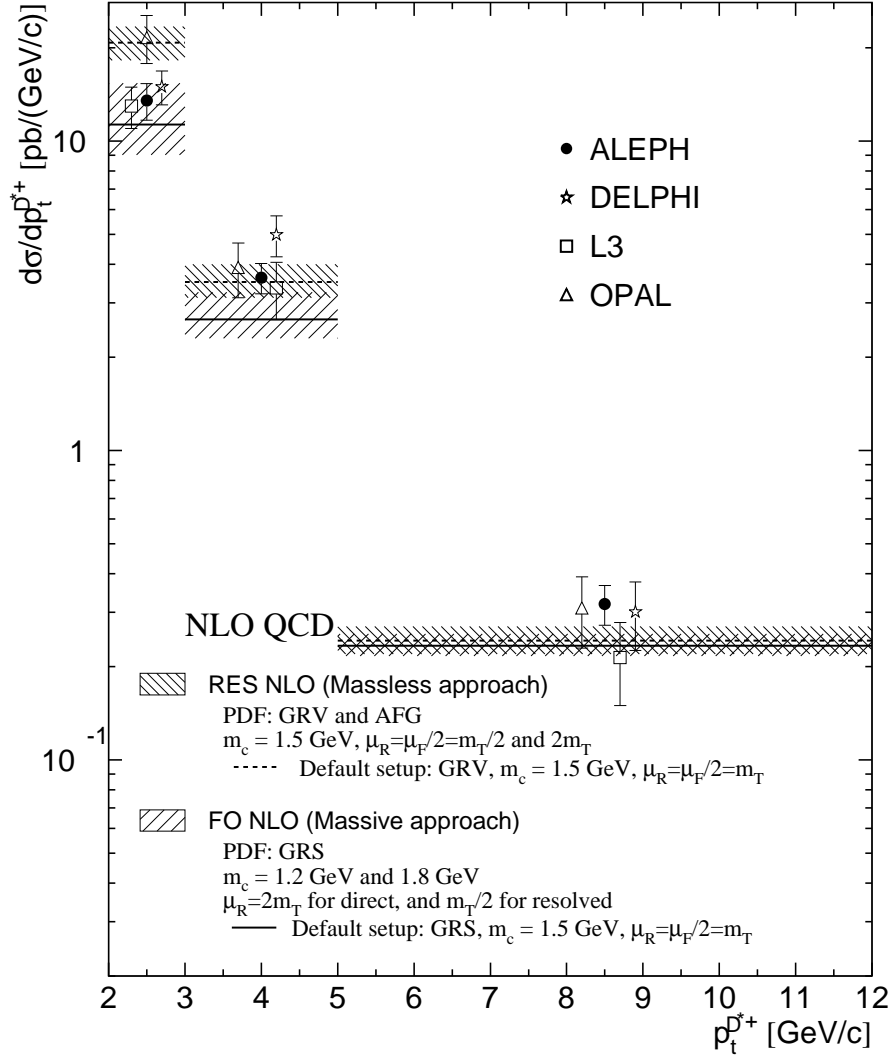
Figure 4.41: Differential cross section $\mathrm{d}\sigma/\mathrm{d}p_t^{\mathrm{D}^{*+}}$ for the inclusive D^{*+} production. The points show the results of this analysis in comparison to those of other LEP experiments (DELPHI, L3, and OPAL) and NLO QCD calculations.
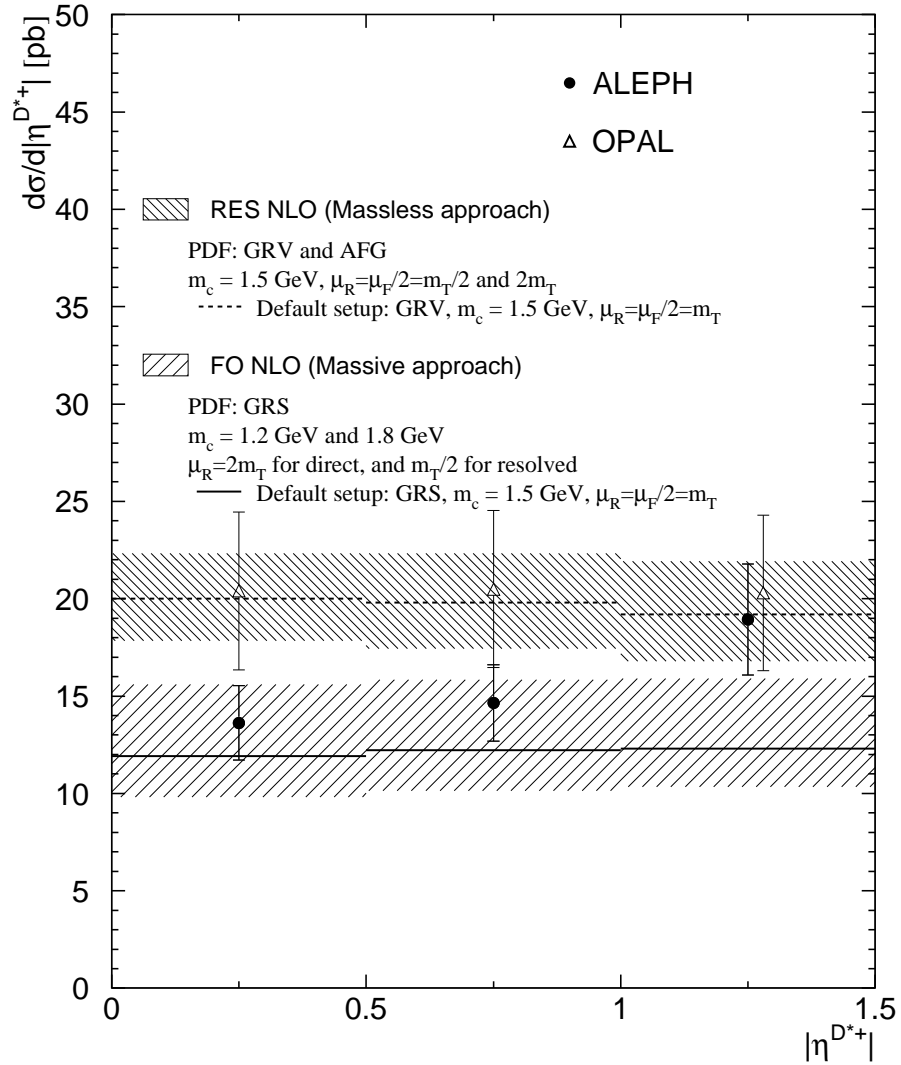
Figure 4.42: Differential cross section $\mathrm{d}\sigma/\mathrm{d}|\eta^{\mathrm{D}^{*+}}|$ for the inclusive D^{*+} production. The points show the results of this analysis in comparison to that of the OPAL collaboration NLO QCD calculations.

4.5 Visible Cross Section

The visible cross section $\sigma_{\text{vis}}^{\text{D}^*}(\text{e}^+\text{e}^- \to \text{e}^+\text{e}^-\text{D}^*X)$ is calculated separately in the acceptance range (4.3) for the three considered decay modes by

$$\sigma_{\text{vis}}^{\text{D}^*}(\text{e}^+\text{e}^- \to \text{e}^+\text{e}^-\text{D}^*X) = \frac{N_{\text{found}}^{\text{D}^{*+}}}{\mathcal{L} \cdot B_* \cdot B_0 \cdot \epsilon} \qquad , \tag{4.13}$$

where the notation is the same as in (4.12). The determination of $N^{\text{D}^{*+}}$ was described in detail in Sect. 4.2.2. The number of D^{*+} found and the efficiencies of reconstructing a D^{*+} candidate for direct and single resolved processes are listed in Table 4.10 together with the derived visible cross sections $\sigma_{\text{vis}}^{\text{D}^*}(\text{e}^+\text{e}^- \to \text{e}^+\text{e}^-\text{D}^*X)$ and their uncertainties for the three decay modes. The systematic error is determined in the same way as for differential cross sections in Sect. 4.4.2. The weighted average over all considered decay modes using the dominating statistical uncertainties for weighting is

$$\sigma_{\text{vis}}^{\text{D}^*}(\text{e}^+\text{e}^- \to \text{e}^+\text{e}^-\text{D}^{*+}X) = 23.39 \pm 1.64\,(\text{stat.}) \pm 1.52\,(\text{sys.})\,\text{pb} \quad . \tag{4.14}$$

The theoretical cross section predicted by the FO NLO QCD [34] is equal to

$$\sigma_{\text{vis}}^{\text{D}^*}(\text{e}^+\text{e}^- \to \text{e}^+\text{e}^-\text{D}^*X) = 17.3\ {}^{+5.1}_{-2.9}\ \text{pb} \qquad , \tag{4.15}$$

where the asymmetric theoretical uncertainty is due to the uncertainties of the charm quark mass and of the renormalization scale.

The RES NLO QCD [35] predicts a significant higher cross section

$$\sigma_{\text{vis}}^{\text{D}^*}(\text{e}^+\text{e}^- \to \text{e}^+\text{e}^-\text{D}^*X) = 29.5 \pm 2.8\,\text{pb} \qquad , \tag{4.16}$$

where the uncertainty originates from the variations of the renormalization and factorization scales and from the choice of PDF.

As far as the central value is concerned, the FO NLO QCD calculation underestimates while the RES NLO QCD overestimates the measurement of this analysis. Nevertheless, the agreement between ALEPH data and the FO NLO QCD calculation is still reasonable taking into account the given uncertainties.

The OPAL experiment has measured the visible cross section $\sigma_{\text{vis}}^{\text{D}^*}(\text{e}^+\text{e}^- \to \text{e}^+\text{e}^-\text{D}^*X)$ in the same acceptance range to be $\sigma_{\text{vis}}^{\text{D}^*}(\text{e}^+\text{e}^- \to \text{e}^+\text{e}^-\text{D}^*X) = 30.7 \pm 2.8\,(\text{stat.}) \pm 3.3\,(\text{sys.})\,\text{pb}$ [57]. The RES NLO calculation again describes OPAL data very well. Two other LEP experiments, DELPHI and L3, also measured this quantity but in different acceptance ranges, therefore their results cannot be compared here.

The visible cross section, $\sigma_{\text{vis}}^{\text{D}^*}(\text{e}^+\text{e}^- \to \text{e}^+\text{e}^-\text{D}^*X)$, together with the differential cross sections, $\text{d}\sigma/\text{d}p_{\text{t}}^{\text{D}^{*+}}$ and $\text{d}\sigma/\text{d}|\eta^{\text{D}^{*+}}|$ measured in the restricted acceptance range (4.3) provide sensible comparisons between data and theory, since both data and theory have relatively small uncertainties. The fully extrapolated total cross section to the full phase space has very large theoretical uncertainties.

	$(K^-\pi^+)\pi^+$	$(K^-\pi^+\pi^0)\pi^+$	$(K^-\pi^+\pi^-\pi^+)\pi^+$
$N_{\mathrm{found}}^{\mathrm{D}^{*+}}$	156.4 ± 14.9	67.4 ± 12.3	128.4 ± 16.3
$\epsilon_{\mathrm{dir}}(\%)$	36.47 ± 0.1	4.81 ± 0.05	17.71 ± 0.09
$\epsilon_{\mathrm{res}}(\%)$	31.68 ± 0.1	3.76 ± 0.04	14.07 ± 0.08
$\sigma_{\mathrm{vis}}^{\mathrm{D}^{*+}}$ (pb)	$24.68 \pm 2.35 \pm 1.47$	$23.04 \pm 4.21 \pm 1.91$	$21.76 \pm 2.76 \pm 1.41$

Table 4.10: The number of D^{*+} mesons found in the acceptance range $2\,\mathrm{GeV}/c < p_{\mathrm{t}}^{\mathrm{D}^{*+}} < 12\,\mathrm{GeV}/c, \quad |\eta^{\mathrm{D}^{*+}}| < 1.5$ for the three decay modes after background subtraction. The efficiency is listed separately for direct and single resolved processes. The visible cross section $\sigma_{\mathrm{vis}}^{\mathrm{D}^{*+}}$ for each considered decay mode is given together with its statistical and systematic errors.

4.6   Total Cross Section

Having measured the visible cross section $\sigma_{\mathrm{vis}}^{\mathrm{D}^{*+}}$, the total cross section for charm production, $\sigma(\mathrm{e^+e^-} \to \mathrm{e^+e^-c\bar{c}})$, is obtained by extrapolating the cross section from the restricted acceptance range (4.3) to the full phase space. Two methods of extrapolation are employed. The first makes use of the LO PYTHIA Monte Carlo and the second bases upon the FO NLO calculation.

Using LO PYTHIA Monte Carlo, the total cross section for the reaction $\mathrm{e^+e^-} \to \mathrm{e^+e^-c\bar{c}}$ is given by

$$\sigma(\mathrm{e^+e^-} \to \mathrm{e^+e^-c\bar{c}}) = \frac{\sigma_{\mathrm{vis}}^{\mathrm{D}^{*+}}}{2 \cdot P_{\mathrm{c}\to\mathrm{D}^{*+}}} \cdot (r_{\mathrm{dir}} \cdot R_{\mathrm{dir}} + r_{\mathrm{res}} \cdot R_{\mathrm{res}}) \quad , \tag{4.17}$$

where

- $\sigma_{\mathrm{vis.}}^{\mathrm{D}^{*+}}$ is the visible inclusive D^{*+} cross section determined in the previous section,
- $P_{\mathrm{c}\to\mathrm{D}^{*+}}$ is the probability for a charm quark to fragment into a D^{*+} meson. Taking the combined quantity $P_{\mathrm{c}\to\mathrm{D}^{*+}} \times BR(\mathrm{D}^{*+} \to \mathrm{D}^0\pi^+) = 0.1631 \pm 0.0050$ from [63] and using $BR(\mathrm{D}^{*+} \to \mathrm{D}^0\pi^+) = (68.3 \pm 1.4)\%$ [40] we obtain $P_{\mathrm{c}\to\mathrm{D}^{*+}} = 0.2388 \pm 0.0088$.
- The factor 2 in the denominator takes into account that for the single inclusive cross sections both the D^{*+} as well as the D^{*-} mesons were counted.
- r_{dir} and r_{res} are the fractions of the direct and single resolved contributions in the considered acceptance range as described in Sect. 4.3
- R_{dir} is the ratio

$$R_{\mathrm{dir}} = \frac{\sigma_{\mathrm{tot,dir}}^{\mathrm{D}^*}}{\sigma_{\mathrm{vis,dir}}^{\mathrm{D}^*}}$$

of the total D^{*+} cross section to the visible cross section in the considered acceptance range (4.3) for direct processes. It describes the extrapolation

of the measured cross section to the total phase space available. R_{res} is the corresponding quantity for the single resolved case.

R_{dir} and R_{res} are estimated using separate samples for direct and single resolved processes generated by the PYTHIA Monte Carlo. The following set of parameters is used to determine R_{dir} and R_{res}. The charm mass is set to $m_{\text{c}} = 1.5\,\text{GeV}$. The heavy quark fragmentation is modelled by the parametrization suggested by Peterson et al. [39] with $\epsilon_{\text{c}} = 0.031$. For the *single resolved* sample the SaS-1D parametrization [20] which is the default choice in PYTHIA is used to describe the resolved photons. This yields $R_{\text{dir}} = 12.74 \pm 0.45\,(\text{stat.})$ and $R_{\text{res}} = 18.62 \pm 0.80\,(\text{stat.})$.

The main theoretical uncertainties entering the calculation of the extrapolation factors stem from the modelling of the fragmentation of charm quarks to D^{*+} mesons. A variation of the charm mass to $m_{\text{c}} = 1.3\,\text{GeV}$ and $m_{\text{c}} = 1.7\,\text{GeV}$ yields a relative error on R_{dir} of $\pm 10\%$ each and on R_{res} an error of $+43\%$ and -19%, respectively. These values are taken as an estimate of the systematic error due to the fragmentation modelling.

In the single resolved case an additional uncertainty enters R_{res} by the choice of the parton density functions describing the resolved photon. Alternatively to the default choice the GRV-LO parametrization [64] was used to calculate R_{res}. This yields a relative deviation of 12%. It is added to the other systematic uncertainty of R_{res} in quadrature. Thus R_{dir} and R_{res} are determined to be:

$$R_{\text{dir}} = 12.7 \pm 1.3 \quad,$$
$$R_{\text{res}} = 18.6 \begin{array}{c} +8.3 \\ -4.2 \end{array} \quad.$$

The uncertainties in r_{dir}, $\sigma_{\text{vis}}^{\text{D}^*}$, and $P_{\text{c}\to\text{D}^{*+}}$, which are assumed to be uncorrelated, are taken into account in the estimation of the statistical and systematic error of the total cross section by Gaussian error propagation.

This results in a total cross section of the reaction $e^+e^- \to e^+e^-c\bar{c}$ at e^+e^- centre-of-mass energies of $\sqrt{s_{e^+e^-}} = (183 - 209)\,\text{GeV}$ of

$$\sigma(e^+e^- \to e^+e^-c\bar{c}) = 731 \pm 74\,(\text{stat.}) \pm 47\,(\text{syst.})\,^{+157}_{-86}\,(\text{extr.})\,\text{pb} \quad. \tag{4.18}$$

Alternatively, the total cross section $\sigma(e^+e^- \to e^+e^-c\bar{c})$ is determined using the FO NLO calculation. Instead of (4.17) in this case $\sigma(e^+e^- \to e^+e^-c\bar{c})$ is calculated as

$$\sigma(e^+e^- \to e^+e^-c\bar{c}) = \frac{\sigma_{\text{vis}}^{\text{D}^{*+}}}{2 \cdot P_{\text{c}\to\text{D}^{*+}}} \cdot R_{\text{tot}} \quad. \tag{4.19}$$

The values for R_{tot} can be extracted from [34] by determining the ratio of the calculated total charm cross section to the charm cross section calculated for the visible D^{*+} range considered in the present analysis, which yields $R_{\text{tot}} = 22.2$. The

variation of the parameter set controlling the calculation yields deviations in the range from -33% to $+72\%$ which are used as an estimate of the systematic error due to the extrapolation. This results in a total cross section

$$\sigma(\mathrm{e^+e^-} \to \mathrm{e^+e^-c\bar{c}}) = 1087 \pm 86\,\mathrm{(stat.)} \pm 70\,\mathrm{(syst.)}^{+783}_{-357}\mathrm{(extr.)\,pb} \quad . \qquad (4.20)$$

The measured total cross sections (4.18) and (4.20) are shown in Fig. 4.43 in comparison to results from other experiments [57, 60, 65–75] and the NLO QCD prediction of Drees et al. [38]. In this NLO QCD calculation, the cross section is given as function of the centre-of-mass energy $\sqrt{s_{\mathrm{e^+e^-}}}$ with the renormalization μ_{R} and the factorization scale μ_{F} are set to $\mu_{\mathrm{F}}^2 = \mu_{\mathrm{R}}^2 = 2 \cdot m_{\mathrm{c}}^2 = 2 \cdot (1.6)^2\,\mathrm{GeV/c^2}$. The GRV parametrization is adopted as PDF for the resolved photon. The theoretical uncertainty due to variations of the charm quark mass m_{c} and the renormalization μ_{R} is about $\pm 40\%$ resulting in a broad band as indicated in Fig. 4.43. At low energies, PETRA/PEP/TRISTAN range, the direct production mechanism is by far the dominant. At LEP2 energies, the single-resolved contribution becomes sizeable and comparable to that of the direct process, while the double-resolved contribution remains negligible.

Within the given uncertainties, this NLO QCD prediction is in good agreement with our measurement and others [76]. As far as the central value is concerned, the preliminary result from DELPHI extrapolated using LO PYTHIA Monte Carlo [60] is in good agreement with the LO result (4.18) of this analysis. Whereas the measurement of the L3 experiment using the same NLO extrapolation method [65] agrees well with the NLO ALEPH result (4.20). The smaller uncertainty of L3's measurement reflects the fact that the acceptance range in that analysis is wider towards the low $p_{\mathrm{t}}^{\mathrm{D^{*+}}}$ range, $1\,\mathrm{GeV/c} < p_{\mathrm{t}}^{\mathrm{D^{*+}}} < 12\,\mathrm{GeV/c}$. The wider acceptance range reduces the uncertainty of the unseen part, especially at low $p_{\mathrm{t}}^{\mathrm{D^{*+}}}$ whose contribution dominates the total cross section (Fig. 4.41).
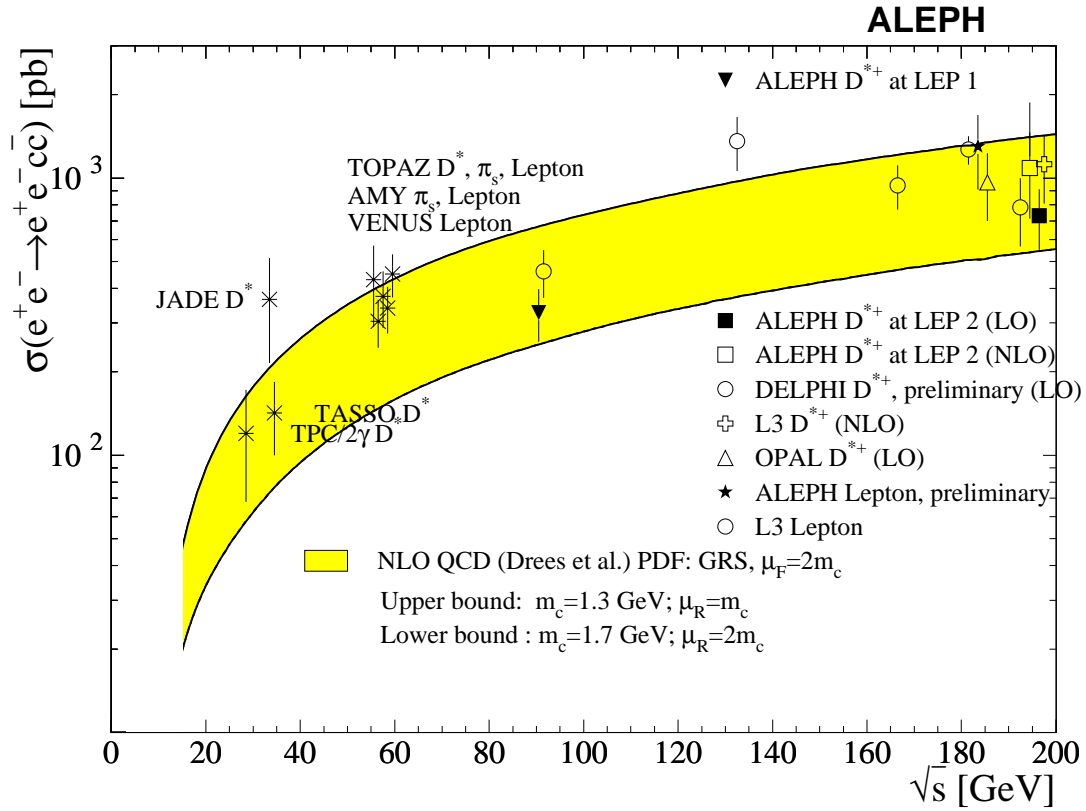
Figure 4.43: The total cross section for charm production $\sigma(\text{e}^+\text{e}^- \rightarrow \text{e}^+\text{e}^-\text{c}\bar{\text{c}})$ versus the centre-of-mass energy $\sqrt{s}$ of the e^+e^- system. The measurements of this analysis are shown as open (NLO) and close (LO) squares at the centre-of-mass energy $\sqrt{s} = 197\,\text{GeV}$. Also shown in this figure is the result of the similar measurement of the ALEPH collaboration at LEP 1 energy [41]. The band represents the range of the NLO QCD prediction [38]. The results obtained by the DELPHI, L3 and OPAL using the D^{*+}-tagging method are reported in [60], [65] and [57], respectively. The L3 and ALEPH measurements using lepton tag can be found in [66] and [67]. Early measurements reported by TPC/2γ [69], JADE [70], TASSO [71], TOPAZ [72, 73], AMY [74], and VENUS [75] at low e^+e^- centre-of-mass energy range are also shown.

Chapter 5

Conclusion

The inclusive production of D^{*+} mesons in two-photon collisions was measured with the ALEPH detector at e^+e^- centre-of-mass energies from $183\,\text{GeV}$ to $209\,\text{GeV}$ in the decay mode $D^{*+} \rightarrow D^0\pi^+$. The D^0 mesons were identified in the decay modes $K^-\pi^+$, $K^-\pi^+\pi^0$, and $K^-\pi^+\pi^-\pi^+$. A total of 339.5 ± 27.0 D^{*+} events from $\gamma\gamma \rightarrow c\bar{c}$ was found from an integrated luminosity of $699\,\text{pb}^{-1}$ in the kinematic region $2\,\text{GeV}/c < p_t^{D^{*+}} < 12\,\text{GeV}/c$ and $|\eta^{D^{*+}}| < 1.5$.

The relative contributions of the main processes, direct and single-resolved, were determined using the event variable $p_t^{D^{*+}}/W_{\text{vis}}$ to be $r_{\text{dir}} = (62.6 \pm 4.2)\%$ and $r_{\text{res}} = 1 - r_{\text{dir}} = (37.4 \pm 4.2)\%$, within the acceptance.

The differential cross sections $d\sigma/dp_t^{D^{*+}}$ and $d\sigma/d|\eta^{D^{*+}}|$ were measured and compared to the fixed-order (FO) NLO QCD calculation [34] and the resummed (RES) NLO QCD calculation [35], as well as to similar measurements from other LEP experiments. While the results of this analysis show a slightly harder spectrum in the $p_t^{D^{*+}}$ distribution compared to both theoretical calculations, the almost flat distribution of $d\sigma/d|\eta^{D^{*+}}|$ which is predicted by the NLO calculations for the visible D^{*+} region is in agreement with the measurement. Overall, the measurements of $d\sigma/dp_t^{D^{*+}}$ and $d\sigma/d|\eta^{D^{*+}}|$ were slightly underestimated by the FO NLO calculation and overestimated by the RES NLO calculation. The agreement between the results of the four LEP experiments is satisfactory, although there is a discrepancy in the low $p_t^{D^{*+}}$ range.

For the integrated visible D^{*+} cross section a value of $\sigma_{\text{vis}}^{D^{*+}} = 23.39 \pm 1.64_{\text{stat}} \pm 1.52_{\text{syst}}$ pb is obtained which is consistent with the FO NLO calculation.

The extrapolation of the visible D^{*+} cross section to the total cross section of charm production introduces large theoretical uncertainties, of which the uncertainty of the charm quark mass and the choice of parton density functions (PDF) used to describe the resolved photon are the main sources. By employing the LO PYTHIA Monte Carlo, the total cross section was determined to be

$$\sigma(e^+e^- \rightarrow e^+e^-c\bar{c})_{<\sqrt{s}>=197\,\text{GeV}} = 731 \pm 74_{\text{stat}} \pm 47_{\text{syst}} {}^{+157}_{-86_{\text{extr}}}\ \text{pb}\quad.$$

5. Conclusion

A different method using the results from the FO NLO calculation yields a higher cross section and a larger error

$$\sigma(\mathrm{e^+e^-} \to \mathrm{e^+e^-c\bar{c}}) = 1087 \pm 86_\mathrm{stat} \pm 70_\mathrm{syst}\,{}^{+783}_{-357}{}_\mathrm{extr}\ \mathrm{pb} \quad .$$

The measured total cross sections $\sigma(\mathrm{e^+e^-} \to \mathrm{e^+e^-c\bar{c}})$ are in good agreement with the NLO QCD calculation as well as with the results from other experiments.

The result of this analysis will be published by the ALEPH Collaboration.

Bibliography

[1] A. Salam and J. C. Ward, Phys. Lett. **13** (1964) 168.

[2] S. Weinberg, Phys. Rev. **19** (1967) 1264.

[3] S. L. Glashow, Phys. Rev. **D2** (1970) 1285.

[4] Gerhard A. Schuler and Torbjörn Sjöstrand. Workshop on Two Photon Physics from DAΦNE to LEP200 and Beyond, 1994. CERN-TH-7193/94.

[5] E. Witten, Nucl. Phys. **B120** (1977) 189.

[6] J. J. Sakurai, Ann. Phys. **11** (1960) 1.

[7] J. J. Sakurai and D. Schildknecht, Phys. Lett. **B40** (1972) 121.

[8] R. Nisius, *The photon structure from deep inelastic electron-photon scattering,* Phys. Rep., **332** (2000) 165-317.

[9] M. Glück, E. Reya and A. Vogt, Z. Phys., **C53** (1992) 127.

[10] M. Glück, E. Reya and A. Vogt, Phys. Rev., **D46** (1992) 1973.

[11] M. Glück, E. Reya and A. Vogt, Z. Phys., **C53** (1992) 651.

[12] G. Altarelli and G. Parisi, Nucl. Phys., **B126** (1977) 298.

[13] Yu. L. Dokshitzer, Sov. Phys. JETP, **46** (1977) 641.

[14] L. N. Lipatov, Sov. J. Nucl. Phys., **15** (1972) 438.

[15] V. N. Gribov and L. N. Lipatov, Sov. J. Nucl. Phys., **15** (1972) 438.

[16] G. Altarelli, Phys. Rev., **81** (1982) 1.

[17] M. Glück, E. Reya, and I. Schienbein, Phys. Rev. **D 60** (1999) 54019.

[18] M. Glück, E. Reya and I. Schienbein, Eur. Phys. J., **C10** (1999) 313.

[19] P. Aurenche, J.P. Guillet, and M. Fontannaz, Z. Phys. **C 64** (1994) 621.

BIBLIOGRAPHY

[20] G. A. Schuler and T. Sjöstrand, Z. Phys. **C 68** (1995) 607.

[21] Proceedings of PHOTON 2001, Ascona (2001), Eds. : M. Kienzle-Focacci and M. Wadhwa, World Scientific.

[22] ALEPH Collaboration, Phys. Lett. **B 458** (1999) 152.

[23] ALEPH Collaboration, ALEPH 99-038 CONF 99-022.

[24] K. Affholderbach, *Messung der hadronischen Structur des Photons*, Fachbereich Physik, Universität Siegen, Ph. D. thesis (2000).

[25] J. Hess, *Measurement of the Hadronic Photon Structure Function $F_2^\gamma(x, Q^2)$ in Two-photon Collisions*, Fachbereich Physik, Universität Siegen, Ph. D. thesis (2002).

[26] ALEPH Collaboration, *Measurement of the Hadronic Photon Structure Function $F_2^\gamma(x, Q^2)$ in Two-photon Collisions*, Paper in preparation.

[27] G. Prange, *Messung des hadronischen Wirkungsquerschnitts doppelt markierter 2-Photon Ereignisse*, Fachbereich Physik, Universität Siegen, Ph. D. thesis (2001).

[28] ALEPH Collaboration,*Measurement of the hadronic cross section of double-tagged $\gamma\gamma$ events at ALEPH* , Paper in preparation.

[29] V. M. Budnev, I. F. Ginzburg, G. V. Meledin, V. G. Serbo, Phys. Rep. , **C15** (1975) 181.

[30] L3 Collaboration, http://l3.web.cern.ch/l3/analysis/gg/

[31] L3 Collaboration, M. Acciarri et al., Phys. Lett. **B 461** (1999) 155.

[32] The DELPHI Collaboration, Contributed paper to ICHEP 2002, DELPHI 2002-080 CONF 614.

[33] The ALEPH Collaboration, A. Heister et al., *Search for $\gamma\gamma \rightarrow \eta_b$ in e^+e^- at LEP 2* Phys. Lett. **B 530** (2002) 56.

[34] S. Frixione, M. Krämer, and E. Laenen, Nucl. Phys. **B 571** (2000) 169.

[35] J. Binnewies, B.A. Kniehl and G. Kramer, Phys. Rev. **D 58** (1998) 014014. J. Binnewies, B.A. Kniehl and G. Kramer, Phys. Rev. **D 53** (1996) 6110.

[36] G. Kramer, and H. Spiesberger, hep–ph/0109167.

[37] M. Cacciari, M. Greco, B.A. Kniehl, M. Krämer, G. Kramer, and M. Spira, hep–ph/9512246.

[38] M. Drees, M. Krämer, J. Zunft, and P. M. Zerwas, Phys. Lett. **B 306** (1993) 371.

[39] C. Peterson, D. Schlatter, I. Schmitt, and P. Zerwas, Phys. Rev. **D 27** (1983) 105.

[40] Particle Data Group, *Review of Particle Physics*, Eur. Phys. J. **C 15** (2000).

[41] The ALEPH Collaboration, D. Buskulic et al., Phys. Lett. **B 355** (1995) 595.

[42] The ALEPH Collaboration, ALEPH 2000-070, CONF 2000-048.

[43] U. Sieler, *Untersuchung der Zwei-Photon Production von D^{*+}-Mesonen mit dem ALEPH-Detektor bei LEP*, Fachbereich Physik, Universität Siegen, Ph. D. thesis (2001).

[44] T. Sjöstrand, Comput. Phys. Commun. **82** (1994) 74.

[45] ALEPH Collaboration, *ALEPH: A Detector for Electron-Positron Annihilations at LEP*, Nucl. Instrum. Meth. **A 294** (1990) 121; **A 303** (1991) 393.

[46] ALEPH Collaboration, *Performance of the ALEPH Detector at LEP*, Nucl. Instrum. Meth. **A 360** (1995) 481.

[47] C. Bowdery, *ALEPH Handbook Volume 1*, CERN publications (1995).

[48] C. Bowdery, *ALEPH Handbook Volume 2*, CERN publications (1997).

[49] F. Ranjard, ALEPH 86-015, intenal note.

[50] R. Brun et al., *Geant 3 Users Guide*, CERN DD/EE/84–1 (1985).

[51] CERN Program Library Long Writeup, *GEANT – Detector Description and Simulation Tool* (1995).

[52] S. Jadach, M. Skrzypek, W. Placzek and Z. Was, Comput. Phys. Commun. **94** (1996) 216.

[53] S. Jadach, B. F. L. Ward and Z. Was, *The Monte Carlo program KORALZ, version 4.0, for the lepton or quark pair production at LEP / SLC energies*, Comput. Phys. Commun. **79** (1994) 503.

[54] J. A. M. Vermaseren, *Two Photon Processes at very high-energies*, Nucl. Phys. **B229** (1983) 347.

[55] The L3 Collaboration, M. Acciarri et al., Phys. Lett. **B 503** (2001) 10.

[56] The ALEPH Collaboration, D. Buskulic et al., Phys. Lett. **B 308** (1993) 425. A. Finch private communication.

[57] The OPAL Collaboration, G. Abbiendi et al., Eur. Phys. J. **C 16** (2000) 579.

[58] S. Catani, Y. L. Dokshitzer, M. H. Seymour, and B. R. Webber, Nucl. Phys. **B 406** (1993) 187.

[59] P. Hodgson, M. Lehto, and B. Pötter, *Measurements of the di-jet cross section in $\gamma\gamma \to hadrons$ with ALEPH*, in Proceedings of PHOTON 2000, Ambleside (2000),
Eds.: A. Finch, New York, American Institute of Physics.

[60] A. A. Sokolov, *Inclusive D^{*+}-meson production in two-photon collisions at LEP*, to appear in proceedings of PHOTON 2001, Ascona, Switzerland (2001).

[61] A. Ngac, *Charged Particle Identification Using Specific Ionisation Energy Loss dE/dx in the ALEPH Detector*, Fachbereich Physik, Universität Siegen, Diploma thesis (2000).

[62] ALEPH Collaboration, *Study of charm production in Z decays*, Eur. Phys. J. **C 16** (2000) 597.

[63] The LEP Collaborations ALEPH, DELPHI, L3, OPAL, the LEP Electroweak Working Group and the SLD Heavy Flavour and Electroweak Groups, CERN-EP/2001-021.

[64] M. Glück, E. Reya, and A. Vogt, Phys. Rev. **D 45** (1992) 3986.

[65] The L3 Collaboration, P. Achard et al., CERN-EP/2002-012.

[66] The L3 Collaboration, P. Acciari et al., Phys. Lett. **B 453** (1999) 83.

[67] O. Krasel and A. Böhrer, *Measurement of charm quark production by muon tagging in two photon events using LEP 2 data*, ALEPH 2000-031, CONF 2000-026.

[68] G. Altarelli, T. Sjöstrand and F. Zwirner, *Physics at LEP2*, CERN 96-01 (1996).

[69] The TPC/2γ Collaboration, M. Alston-Garnjost et al., Phys. Lett. **B 252** (1990) 499.

[70] The JADE Collaboration, W. Bartel et al., Phys. Lett. **B 184** (1987) 288.

[71] The TASO Collaboration, W. Braunschweig et al., Z. Phys. **C 47** (1990) 499.

[72] The TOPAZ Collaboration, R. Enomoto et al., Phys. Lett. **B 328** (1994) 535.

[73] The TOPAZ Collaboration, R. Enomoto et al., Phys. Rev. **D 50** (1994) 1879.

[74] T. Nozaki (The AMY Collab.), in proceeding of PHOTON 95, Sheffield (1995), S. Cartwright, D. Miller and V. A. Khose *edt* (World Scientific).

[75] The VENUS Collaboration, S. Uehara et al., Z. Phys. **C 63** (1994) 213.

[76] A. Böhrer and M. Krawczyk, *Summary of PHOTON 2001*, hep-ph/0203231.

[77] The ALEPH Collaboration, A. Heister et al., *Measurement of the inclusive $D^{*\pm}$ production in $\gamma\gamma$ collisions at LEP 2*, CERN-EP/2003-02; Submitted to Eur. Phys. J. C.

List of Tables

List of Figures

Acknowledgments